Effect of relaxation on eigenstresses and microcracking in concrete under imposed deformation

Bouquet, Guus

DOI
10.4233/uuid:5d9a9cc3-9f5a-4a0e-9ff1-f7dbd310a6a9

Publication date
2019

Document Version
Final published version

Citation (APA)
Bouquet, G. (2019). *Effect of relaxation on eigenstresses and microcracking in concrete under imposed deformation*. [Dissertation (TU Delft), Delft University of Technology]. https://doi.org/10.4233/uuid:5d9a9cc3-9f5a-4a0e-9ff1-f7dbd310a6a9

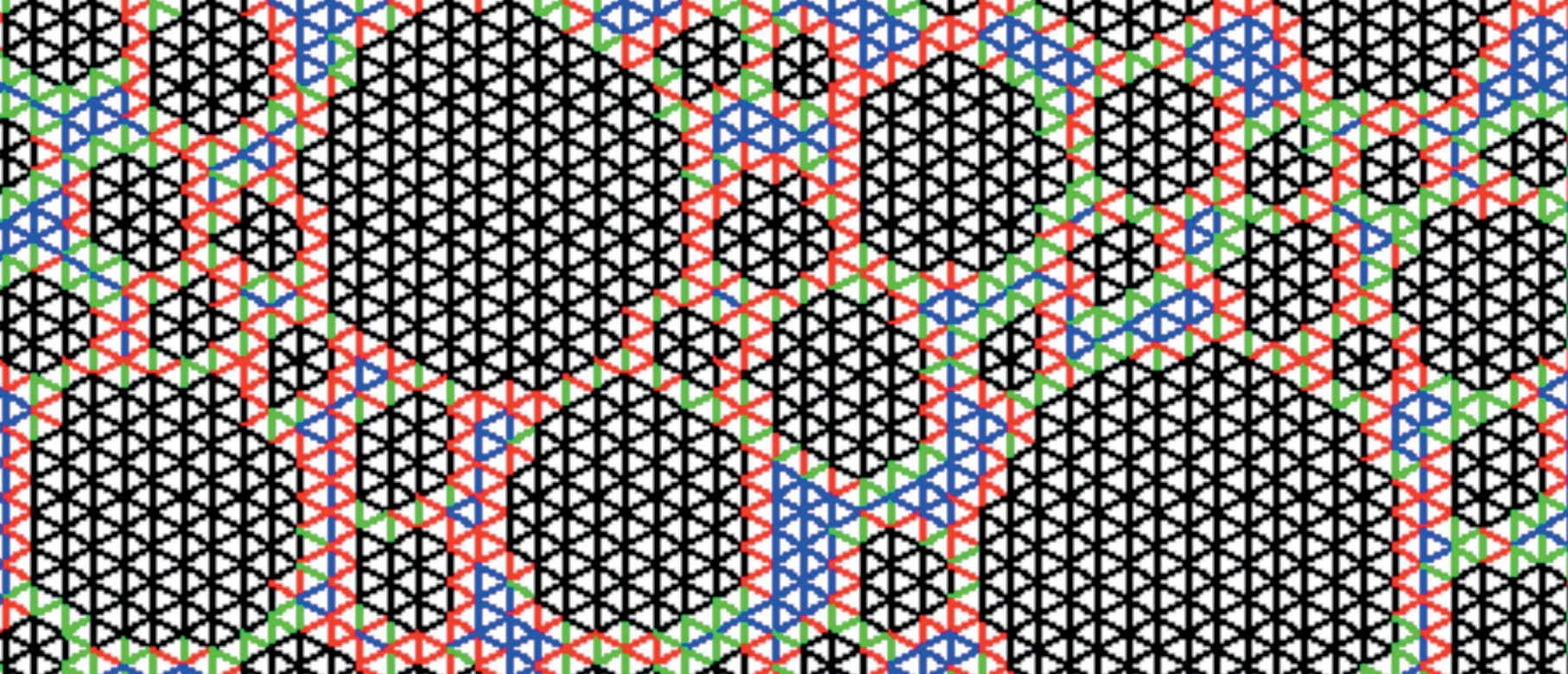

Effect of relaxation on eigenstresses and microcracking in concrete under imposed deformation

Gustaaf Chr. Bouquet

Effect of relaxation on eigenstresses and microcracking in concrete under imposed deformation

Proefschrift

ter verkrijging van de graad van doctor
aan de Technische Universiteit Delft,
op gezag van de Rector Magnificus prof. dr.ir. T.H.J.J. van der Hagen,
voorzitter van het College voor Promoties,
in het openbaar te verdedigen op

donderdag 11 juli 2019 te 10.00 uur
door

Gustaaf Christiaan BOUQUET

civiel ingenieur
geboren te ’s-Gravenhage

Dit proefschrift is goedgekeurd door de promotoren:

Prof. dr.ir. K. van Breugel
Prof. dr.ir. H.E.J.G. Schlangen

Copromotor: Dr.ir.drs. C.R. Braam

Samenstelling van de promotiecommissie:

Rector Magnificus	Voorzitter
Prof. dr.ir. K. van Breugel	Technische Universiteit Delft, promotor
Prof. dr.ir. H.E.J.G. Schlangen	Technische Universiteit Delft, promotor
Dr.ir.drs. C.R. Braam	Technische Universiteit Delft, copromotor
Prof. ir. A.Q.C. van der Horst	TU Delft, Koninklijke BAM Groep
Prof. dr.ir. J.W.G. van de Kuilen	TU Delft, TU München
Dr.ir. A. Taheri – Motlagh	Ports & Maritime Organization (PMO), Iran
Dr.ir. R.A. Vonk	Royal HaskoningDHV

ISBN / EAN: 978-94-6384-022-4
Cover design: G.Chr. Bouquet & F.M. Bouquet
Printed by: Proefschriftmaken.nl
Published by: Proefschriftmaken.nl

Keywords: eigenstress, stress relaxation, microcracks, imposed shrinkage deformation, durability, chloride penetration

Table of contents

List of Symbols

Latin letters

A_{beam}	Cross-sectional area of a lattice beam	[m^2]
C_s	Chloride concentration at the concrete surface	[kg/m^3]
C_i	Chloride concentration in the cement paste matrix of the concrete	[kg/m^3]
D_a	Apparent diffusion coefficient of concrete	[m^2/h]
$D_{RCM,0}$	Diffusion coefficient, measured with the RCM-test	[m^2/h]
D_h	Moisture diffusion coefficient	[m^2/h]
D_{UPV}	Degree of microcrack damage measured with ultrasonic pulse velocity	[-]
D(t)	Chloride diffusion coefficient at time t	[m^2/h]
D_0	Iitial chloride diffusion coefficient at time t = 0	[m^2/h]
D_{mc}	Microcrack damage ratio	[-]
d	Diameter of aggregate particle	[mm]
E_0	Modulus of elasticity of cement paste at the time of loading t_0	[N/m^2]
E_a	Modulus of elasticity of aggregate	[N/m^2]
E_b	Modulus of elasticity of bond beams	[N/m^2]
E_c	Modulus of elasticity of concrete	[N/m^2]
E_{cm}	Secant modulus of elasticity of concrete	[N/m^2]
E_d	Dynamic modulus of elasticity of concrete	[N/m^2]
E_m	Modulus of elasticity of matrix beams	[N/m^2]
E_p	Modulus of elasticity of cement paste beams	[N/m^2]
F	Normal force in cement paste beams	[N]
f_b	Tensile strength bond beams in equilateral triangle beam lattice model	[N/mm^2]
$f_{cm,cube}$	Mean concrete compressive strength of 150 mm cubes	[N/mm^2]
$f_{ctm,cube}$	Mean concrete tensile strength of 150 mm cubes	[N/mm^2]
f_{ctm}	Sound mean value of the concrete tensile strength	[N/m^2]
f_m	Tensile strength matrix beams in equilateral triangle beam lattice model	[N/mm^2]
f_p	Tensile strength of cement paste	[N/mm^2]
h	Height of the beams in the equilateral triangle beam lattice model	[mm]
h_d	Relative humidity of the cement paste in concrete due to drying shrinkage	[%]
k	Load vector	[-]
L_x	Length of beam lattice model in horizontal (x) direction	[mm]
L_y	Length of beam lattice model in vertical (y) direction	[mm]
l_{beam}	Length of the beams in the equilateral triangle beam lattice model	[mm]
m	Activation volume ratio ($m = \Delta V/RT$)	[-]
N_b	Total number of bond beams in the beam lattice model	[-]
N_m	Total number of matrix beams in the beam lattice model	[-]
N	Residual number of cement paste beams after micro-cracking	[-]
N_0	Total number of cement paste beams	[-]
n	Number of layers in the Finite Layer Method (chapter 2)	[-]
n	Ageing factor expressing the decrease of chloride diffusion over time	[-]
R	Universal gas constant	[J/molK]

S	Stiffness matrix	[-]
T	Transformation matrix	[-]
T	Absolute temperature	[K]
t	Time	[h]
t_0	Initial time at the start of measurements	[h]
U	Activation energy	[J/mol]
U_0	Initial activation energy at time t_0	[J/mol]
ΔU_0	Enhancement factor for the increase of activation energy over time	[J/mol]
ΔV	Apparent activation volume	[m^3/mol]
V_a	Aggregate volume fraction in 2D lattice model	[m^2/m^2]
$V_{agg,dmin}$	Aggregate 'volume' fraction of particles < d_{min} (2D-lattice)	[m^2/m^2]
v_0	Ultrasonic pulse velocity before loading of concrete specimen	[km/s]
v	Ultrasonic pulse velocity after loading of concrete specimen	[km/s]
v	Displacement vector	[-]
Δy	Thickness of layer in the Finite Layer Method (chapter 2)	[m]
Δy	Vertical displacement (y-direction)(chapter 5)	[m]

Greek letters

α_{ds}	Coefficient of linear drying shrinkage	[m/m]
β	Concrete crack probability factor ($\beta = \sigma_{cr} / f_{ctm}$)	[-]
ε_{cr}	Tensile cracking strain of concrete	[m/m]
ε_{ctu}	Tensile strain capacity of concrete ($\varepsilon_{ctu} = f_{ctm} / E_{cm}$)	[m/m]
$\varepsilon_{c,sh}$	Concrete shrinkage	[m/m]
$\varepsilon_{p,sh}$	Cement paste shrinkage	[m/m]
$\varepsilon_{p,ds}$	Cement paste drying shrinkage	[m/m]
$d\varepsilon_{cr}/dt$	Creep strain rate	[m/mh]
$d\varepsilon_0/dt$	Initial strain rate constant at t_0	[m/mh]
ν	Dynamic Poisson's ratio of concrete	[-]
ν_{latt}	Apparent Poisson's ratio of the equilateral triangle beam lattice model	[-]
ρ	Densite of concrete	[kg/mm^3]
σ_0	Stress at the time of loading t_0	[N/mm^2]
$\sigma_{e,k}$	Eigensstress in layer k in the Finite Layer Method (chapter 2)	[N/mm^2]
σ_k	Stress in layer k in the Finite Layer Method (chapter 2)	[N/mm^2]
σ_N	Stress due to 'normal' force in the Finite Layer Method (chapter 2)	[N/mm^2]
$\sigma_{M,k}$	Bending stress in layer k in the Finite Layer Method (chapter 2)	[N/mm^2]
σ_{tan}	Tangential tensile stress in cement paste near an aggregate particle	[N/m^2]
σ_{rad}	Radial compressive stress in cement paste near an aggregate particle	[N/m^2]
σ_{cr}	Concrete cracking stress	[N/m^2]
γ	Correction factor to ensure the correct volume fraction in 2D-lattice model	[-]
ψ	Relaxation coefficient	[-]

List of abbreviations

AE	Acoustic emmission
AVF	Aggregate volume fraction
BLM	Beam lattice model
CG	Continuous grading
CTE	Coefficient of thermal expansion
ESEM	Environmental scanning electron microscopy
FEM	Finite element method
FLM	Finite layer method
HPC	High performance concrete
ITZ	Interfacial transition zone
MP	Multi particle size grading
NWC	‘Normal’ weight concrete
LWAC	‘Light’ weight aggregate concrete
OC	Ordinary concrete
PSD	Particle size distribution
RH	Relative humidity
SP	Single particle size grading
UPV	Ultrasonic pulse velocity

List of figures

Chapter 1

Chapter 2

Chapter 3

Chapter 4

Chapter 5

Chapter 6

Summary

For the dimensioning of concrete structures it is customary to determine the forces and stresses occurring in construction elements on the basis of the prescribed loads. In an iterative process, the final dimensions of the elements and reinforcement are then determined. This process becomes less simple if not only the *external loads*, but also the *deformations* imposed by shrinkage and temperature change are the cause of forces and stresses. The determination of stresses in the concrete becomes even more complicated if we not only want to know the distribution of forces and the associated stresses in the structures, but also the so-called *eigenstresses*, which are the result of non-linear temperature and shrinkage fields in concrete cross-sections. These eigenstresses can give rise to microcracks, often in the surface zone of concrete elements. These microcracks can jeopardize the durability of the concrete. With the methods for calculating the force distribution in a concrete construction, these eigenstresses remain out of sight. In current design practice, these eigenstresses are almost never taken into account. The assumption is that as a result of relaxation the eigenstresses largely disappear and will have no influence on the behavior and durability of concrete structures. This research examines whether this assumption is justified.

In chapter 1 the occurrence of eigenstresses due to temperature changes and drying shrinkage is described. A distinction is made between the eigenstresses caused by a non-linear strain field in the concrete cross-section (*structural restraint*) and the eigenstresses due to the restrained cement paste shrinkage caused by the aggregate (*material restraint*). In this study , the emphasis is on eigenstress and microcracking as a result of drying shrinkage. The eigenstresses in the cement paste and the possibly occurring microcracking are reduced by relaxation. This dissertation focuses on the influence of relaxation on eigenstresses and microcracking in concrete. The research question is therefore:

What is the effect of relaxation on the resulting eigenstresses and microcracking?

Chapter 2 contains a review of the literature regarding eigenstresses and microcracking in concrete structures. Crack criteria are discussed, as well as the effect of microcracking on the permeability and diffusion resistance of concrete. It discusses which methods are available for calculating stresses due to *structural restraint* and *material restraint*. In this context, attention is given to finite element programs and lattice models.

Chapter 3 describes the (two-dimensional) beam lattice model (Beam Lattice Model - BLM) used in this study. With this model, concrete is modeled as a 3-phase material, consisting of circular aggregate particles embedded in a cement paste matrix with a boundary layer (ITZ) at the interface between matrix and aggregate particles. The three components are represented by 'beams' with different properties. It describes how the stresses in the beams in the BLM are calculated as a result of an imposed shrinkage strain. In the calculation of the stresses in the beams, relaxation is applied or not.

Chapter 4 deals with the time-dependent behavior of cement paste and concrete. Subsequently, it is discussed how time-dependent behavior, i.e. relaxation, can be taken into account. The calculation rules for relaxation in concrete, as described in Eurocode 2, part 1-1, are suitable for calculating the effect of relaxation on the force distribution in a concrete structures, but are not suitable for the calculation of stress relaxation at cement paste level. In this study, the activation energy concept is used to calculate time-dependent behavior at paste level. Relaxation coefficients are derived based on this concept. The relaxation of stresses partly depends on the speed with which the strains are applied.

In chapter 5 the results of an extensive numerical parameter study are described. An imposed shrinkage curve is defined, with which most calculations have been carried out. The tensile strength and stiffness of the cement paste beams is specified. The magnitude of microcracking is indicated by a Microcrack Damage Ratio (D_{mc}). Calculations were made with BLM specimens with one single-particle (SP), with multiple particles of the same diameter (MP) and with continuous particle size grading (CG). The aggregate volume fraction in the BLM specimens varies from 0.08 to 0.75 m^2/m^2 (8 to 75%). The calculations were performed with and without relaxation of stresses. The magnitude of relaxation is thereby varied (i.e. different values for the activation energy). The development of eigenstress and microcracking has been investigated for variations in, among other things, the following parameters: stiffness of the cement paste, ratio between the tensile strength of the bond beams (representing the ITZ) and the matrix beams, stiffness of the aggregate, size of the aggregate particles and the particle grading, the speed with which the shrinkage strains are imposed and the magnitude of the activation energy. The influence of microcrack formation on the magnitude of the drying shrinkage of concrete was also investigated.

In Chapter 6 it was investigated whether the simple calculation model used in this thesis could describe the influence of microcracking on the transport properties of concrete. The results of a study about chloride penetration in concrete were available. In that experiment, the concrete was subjected to temperature and moisture cycles during the penetration process. In the experiments it was shown that temperature and moisture cycles resulted in increased chloride penetration in the concrete. This was attributed to microcracking that had developed during the temperature and moisture cycles. With the BLM the microcracking in the concrete is determined according to the temperature and shrinkage strains to which the concrete was subjected in the experiment. On the basis of literature data, a relationship has been established between the magnitude of the apparent diffusion coefficient and the extent of microcrack formation, i.e. the Microcrack Damage Ratio D_{mc}. The values of the apparent diffusion coefficient thus calculated are used for comparison with the values of the apparent diffusion coefficient derived from the test results.

Chapter 7 contains the conclusions and recommendations. The main results of the study can be summarized as follows.

- Eigenstresses in concrete, caused by an imposed shrinkage deformation, will almost always lead to (micro-)crack formation. This applies to conditions of both *structural restraint* and *material restraint*.
- Due to relaxation (in the cement paste) stresses caused by an imposed shrinkage deformation increase less rapidly and the intensity of microcracking is reduced compared to a situation without relaxation.
- The properties of the aggregate and the aggregate volume fraction influence the crack pattern, but have only a limited influence on the probability of cracking under an imposed shrinkage deformation.
- As a result of microcracking, the drying shrinkage measured on concrete test specimen will be smaller compared to a shrinking specimen that remains free from microcracking. This reduction can amount up to 10 to 15% of the measured shrinkage values. Without relaxation, this difference would be even greater (without relaxation more cracking).
- Microcracks have an effect on the transport properties of concrete. However, simulations performed indicate an underestimation of the calculated effect of microcracks on transport properties compared to experimentally found values. Reason for the differences is probably that in the simulations (in chapter 6) the microcracks are assumed to be homogeneously distributed in the concrete. However, the simulations of crack patterns performed in chapter 5 show that in reality microcracks may become connected and thus form a continuous transport route.
- Lifetime predictions often assume an *increasing* resistance to penetration of substances in the concrete over time. However, microcracking due to eigenstresses leads to a *decrease* of this resistance. It is presumed that, among other things, selfhealing of microcracks contributes substantially to the ability of concrete to resist the penetration of aggressive substances in concrete.

Samenvatting

Voor het dimensioneren van betonconstructies is het gebruikelijk om de in bouwdelen optredende krachten en spanningen te bepalen op basis van de maatgevende belastingen. In een iteratief proces wordt vervolgens de definitieve afmetingen en de wapening bepaald. Dit proces wordt minder eenvoudig als niet alleen de *uitwendige belastingen*, maar ook de door krimp en temperatuurverandering *opgelegde vervormingen* de bron zijn van krachten en spanningen. Het bepalen van spanningen in het beton wordt nog ingewikkelder wanneer men niet alleen de krachtsverdeling en de daarbij behorende spanningen in de constructies wil weten, maar ook de zogenoemde *eigenspanningen*, die het gevolg zijn van niet-lineaire temperatuur- en krimpvelden in een betondoorsnede. Deze eigenspanningen kunnen aanleiding geven tot microscheurvorming, vaak aan de oppervlak van een betonconstructie. Deze microscheuren kunnen nadelig zijn voor de duurzaamheid van het beton. Met de methoden voor het berekenen van de krachtsverdeling in een betonconstructie blijven deze eigenspanningen buiten beeld. In de gangbare ontwerpparktijk wordt met deze eigenspanningen ook vrijwel nooit gerekend. De veronderstelling is daarbij dat als gevolg van relaxatie de eigenspsanningen grotendeels verdrwijnen en geen invloed zullen hebben op het gedrag en de duurzaamheid van een betonconstructie. In dit onderzoek wordt onderzocht of deze veronderstelling gerechtvaardigd is.

In hoofdstuk 1 wordt het optreden van eigenspanningen als gevolg van temperatuurveranderingen en uitdrogingskrimp beschreven. Onderscheid wordt gemaakt tussen eigenspanningen veroorzaakt door een niet-lineair rekveld in de betondoorsnede (*structural restraint*) en de eigenspanningen als gevolg van door toeslagmateriaal verhinderde krimp van de cementsteen (*material restraint*). In het onderzoek ligt de nadruk op eigenspanningen en microscheurvorming als gevolg van uitdrogingskrimp. De eigenspanningen in de cementsteen en de eventueel optredende microscheurvorming worden gereduceerd door relaxatie. Dit proefschift richt zich op de invloed van relaxatie op eigenspanningen en microscheurvorming in beton. De onderzoeksvraag luidt dan ook:

Wat is het effect van relaxatie op de resulterende eigenspanningen en microscheurvorming?

Hoofdstuk 2 bevat een literatuuroverzicht betreffende eigenspanningen en microscheurvorming in betonconstructies. Scheurcriteria worden besproken, alsmede het effect van microscheurvorming op de permeabiliteit en diffusieweerstand van beton. Besproken wordt welke methoden beschikbaar zijn voor het berekenen van spanningen als gevolg van *structural restraint* en *material restraint*. In dit verband wordt aandacht gegeven aan eindige elementen programma's en staafwerkmodellen (Lattice models).

In hoofdstuk 3 wordt het in deze studie toegepaste (twee-dimensionale) staafwerkmodel (*Beam Lattice Model - BLM*) beschreven. Met dit model wordt beton gemodelleerd als een 3-fasen materiaal, bestaande uit cirkelvormige toeslagkorrels ingebed in de cementsteen matrix met een grenslaag (*ITZ*) in het grensvlak tussen matrix en toeslagkorrels. De drie componenten worden gerepresenteerd door 'staafjes' met verschillende eigenschappen. Beschreven

wordt hoe de spanningen in de staafjes in het BLM worden berekend als gevolg van een opgelegde krimpvervorming. Bij de berekening van de spanningen in de staafjes wordt al dan niet relaxatie toegepast.

In hoofdstuk 4 wordt ingegaan op het tijdafhankelijk gedrag van cementsteen en beton. Vervolgens wordt besproken hoe tijdafhankelijk gedrag, i.c. relaxatie, in rekening kan worden gebracht. De rekenregels voor de berekening van relaxatie in beton, zoals omschreven in Eurocode 2, deel 1-1, zijn geschikt voor het berekenen van het effect van relaxatie op de krachtsverdeling in een betonconstructie, maar kunnen niet zonder meer worden toegepast voor de berekening van spanningsrelaxatie op cementsteenniveau. In deze studie wordt voor het in rekening brengen van tijdsafhankelijk gedrag het activeringsenergie concept toegepast. Op basis van dit concept wordt een relaxatiecoefficient afgeleid. De relaxatie van spanningen is mede afhankelijk van de snelheid waarmee de rekken worden opgelegd.

In hoofdstuk 5 worden de resultaten van een uitgebreid numeriek parameteronderzoek beschreven. Als opgelegde vervorming is een krimpverloop vastgelegd, waarmee de meeste berekeningen zijn uitgevoerd. De treksterkte en stijfheid van de cementsteenstaafjes is gespecificeerd. De omvang van de microscheurvorming wordt aangeduid met een microscheurratio (D_{mc} = Microcrack Damage Ratio). Er zijn berekeningen uitgevoerd met BLM-proefstukken met een enkele korrel (SP), met meerdere korrels met gelijke diameter (MP) en met een continue korrelgradering (CG). Het toeslaggehalte in de BLM-proefstukken varieert van 0.08 tot 0.75 m^2/m^2 (8 tot 75%). De berekeningen zijn uitgevoerd met en zonder relaxatie van spanningen. De intensiteit van het relaxatiegedrag wordt daarbij gevarieerd (i.c. verschillende waarden voor de activeringsenergie). De ontwikkeling van eigenspanningen en microscheurvorming is onderzocht voor variaties in onder meer de volgende parameters: stijfheid van de cementsteen, verhouding tussen de treksterkte van de bond-staafjes (representeren de ITZ) en de matrix-staafjes, stijfheid van het toeslagmateriaal, grootte van de toeslagkorrels en de korrelgradering, de snelheid waarmee de krimprekken zijn opgelegd en de grootte van de activeringsenergie. Ook is onderzocht wat de invloed is van microscheurvorming op de grootte van de uitdrogingskrimp van beton.

In hoofdstuk 6 is onderzocht of met het in dit proefschrift toegepaste eenvoudige rekenmodel de invloed van microscheuvorming op de transporteigenschappen van beton kan worden beschreven. Ter beschikking stonden resultaten van een onderzoek naar chlorideindringing in beton. In dat experiment werd het beton gedurende het indringingsproces onderworpen aan temperatuur- en vochtcycli. In de experimenten was aangetoond dat temperatuur- en vochtcycli een verhoogde chlorideindringing in het beton tot gevolg hadden. Dit werd toegeschreven aan microscheurvorming die tijdens de temperatuur- en vochtcycli was ontstaan. Met het BLM is de microscheurvorming in het beton bepaald behorend bij de temperatuur- en krimprekken waaraan het beton in het experiment was onderworpen. Op basis van literatuurgegevens is een relatie gelegd tussen de grootte van de schijnbare diffusiecoëfficient en de omvang van de microscheurvorming, i.c. de microscheurratio D_{mc}. De hiermee berekende waarden van de schijnbare diffusiecoëfficient zijn gebruikt voor de vergelijking met de uit de proefresultaten gedestileerde waarden van de schijnbare diffusiecoëfficient.

Hoofdstuk 7 omvat de conclusies en aanbevelingen. De belangrijkste resultaten van het onderzoek laten zich als volgt samenvatten.

- Eigenspanningen in beton, veroorzaakt door een opgelegde krimpvervorming, zullen vrijwel altijd tot (micro-)scheurvorming leiden. Dit geldt zowel voor de situaties 'structural restraint' als 'material restraint'.
- Door relaxatie (in de cementsteen) nemen spanningen als gevolg van een opgelegde krimpvervorming minder snel toe en neemt de intensiteit van microscheurvorming af vergeleken met een situatie zonder meenemen van relaxatie.
- De eigenschappen en het volume van het toeslagmateriaal beïnvloeden het scheurenpatroon, maar hebben slechts geringe invloed op de kans op scheurvorming onder een opgelegde krimpvervorming.
- Als gevolg van microscheurvorming zal de aan betonnen proefstukken gemeten uitdrogingskrimp kleiner zijn dan in het geval geen microscheuren zouden ontstaan. Deze reductie kan oplopen tot 10 à 15% van de gemeten krimpwaarden. Zonder relaxatie zou dit verschil nog groter zijn (zonder relaxatie meer scheurvorming).
- Microscheuren hebben effect op de transporteigenschappen van beton. Uitgevoerde simulaties wijzen echter op een onderschatting van het berekende effect van microscheuren op transporteigenschappen vergeleken met experimenteel gevonden waarden. Reden voor de verschillen is waarschijnlijk dat in de simulaties (in hoofdstuk 6) de microscheuren homogeen verdeeld zijn in het beton. Uit de in hoofdstuk 5 uitgevoerde simulaties van scheurpatronen blijkt echter dat in werkelijkheid microscheuren met elkaar verbonden zijn en zo een doorgaande transportweg vormen.
- In levensduurvoorspellingen wordt vaak uitgegaan van een toenemende weerstand tegen indringen van stoffen in beton bij toenemende ouderdom. Microscheurvorming door eigenspanningen leiden echter tot een afname van deze weerstand. De veronderstelling is dat o.a. zelfherstel van microscheuren substantieel bijdraagt aan het vermogen van beton om weerstand te bieden tegen indringen van agressieve stoffen in beton.

Acknowledgements

I want to express my sincere gratitude to my promotor, professor dr.ir. Klaas van Breugel and my advisor dr.ir.drs. C. René Braam, for their commitment, guidance, support, and advice throughout the years I was working on this Ph.D. research at the Delft University of Technology. Gratitude is also expressed to my friend, ir. Henk J.M. Lamers, for the work and kind support on the development of the numerical research tool Lattice.

I also want to express gratitude to the colleagues and laboratory personnel for their work and kind support. Thanks also to my former colleagues in the Eerste Nederlandse Cement Industrie (ENCI B.V.) and *Stufib* members for their interest in my research results.

This research would not have been possible without the financial support of ENCI Studiefonds during 4 years, Stichting Stimulering Kennisontwikkeling Kwaliteitsbeheersing Bouwconstructies (SKKB) during 1 year and a subsidy provided in the context of the Wet Bevordering Speur- en Ontwikkelingswerk (WBSO).

Finally, and most importantly, I wish to express my deep-felt thanks to my partner José G. Koetsenruijter for her support and understanding. Moreover, I wish to express my thanks to my daughters Merel Marije and Fleur Margot for their interest and enthusiasm, which gave me the power to finalise this adventure!

Chapter 1

1. Introduction

1.1 History of structures made with brittle building materials

For more than 100 years the performance of concrete structures has illustrated that concrete is a durable building material that can resist high compressive forces. Structures primarily loaded in compression are known to last even for centuries. Historic examples of centuries old structures made of concrete or stone-like materials loaded in compression are the dome of the Pantheon in Rome and the arches of bridges and aqueducts. The Pantheon is about 2000 years old, but still in perfect shape.

Figure 1.1 Dome of the Pantheon – Rome (photo: G.Chr. Bouquet).

Figure 1.2 Aquaduct Ponte delle Torri – Spoleto (Italy) (photo: G.Chr. Bouquet).

Although strong in compression, concrete is relatively week in tension. In reinforced concrete steel bars take up the tensile forces. Under ordinary service loads reinforced concrete is allowed to crack. After cracking of the concrete the tensile forces in the cross section of structural elements are transferred to the embedded steel bars. These cracks are an inherent feature of reinforced concrete and should not be considered as damage, unless the crack widths exceed predefined values. The building codes give rules for determining the amount of reinforcing steel needed to resist the imposed loads and for predicting the crack width in the 'serviceability limit state' (SLS). The maximum allowable crack widths are given in building codes and depend on the ambient conditions to which the structure will be exposed during its service life.

For calculating and detailing the required amount of reinforcement and the crack width codes assume that the concrete is initially *stress free* and that stresses in the concrete structure are caused exclusively by the (external) imposed loads, like deadweight, traffic, goods, people etc. Besides the stress induced by these imposed loads concrete structures may also contain stresses caused by *imposed deformations*. These imposed deformations may originate

from thermal and/or hygral loads, i.e. swelling and shrinkage. In case imposed deformations are restrained they will cause stresses in the concrete. Already in the early stage of a structure's lifetime, i.e. in the stage of *hardening*, thermal loads are generated as result of the exothermal hydration process. Exposure of a *hardened* structure to temperature variations and to drying and wetting also creates strain fields in the concrete, which will cause deformations and, if these deformations are restrained, compressive or tensile stresses. If the tensile stresses reach the tensile strength of the concrete, cracking is likely to occur. To which extent cracks caused by imposed deformations jeopardize proper functioning of the structure strongly differs from case to case. Cracks may cause leakage, impair the aesthetics of a structure, reduce the stiffness of structural elements and/or reduce the durability.

The extent of the impact of imposed deformations on the durability of concrete structures has been subject of debate. This thesis will focus on one of the aspects of this debate, namely the role of relaxation on the so-called eigenstresses and (micro)cracking in the concrete cover of concrete structures.

1.2 Imposed deformation and structural eigenstresses in concrete

1.2.1 Hardened concrete elements under imposed deformation

A typical example of a structural element under imposed thermal deformation is shown in Fig. 1.3a. The element is one-sided cooled down. The imposed thermal loads is modelled as a triangular temperature drop. The element is completely clamped at the top and bottom. Due to cooling the outer zone will shorten. Since this shortening is restrained tensile stresses will be generated in the cooled zone.

In case of free elongation and free bending of the element, only *thermal eigenstresses* will occur, see Fig. 1.3b. In this example tensile stresses occur in the outer zones and compressive stresses in the interior of the element.

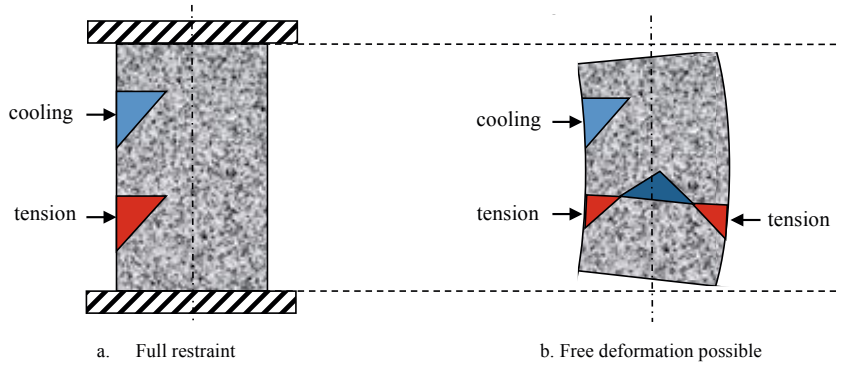

Figure 1.3 Massive concrete wall exposed to surface cooling (after Van Breugel et al., 1996)
a. Full restraint: tensile stresses in cooled surface zone.
b. Element free to deform, resulting in thermal eigenstresses: tension in outer zones and compression in the interior.

Similarly, drying shrinkage of the outer zone of the structure causes drying-induced tensile stresses. Also in this case the stress distribution in the cross-section depends on the kinematic boundary conditions of the element.

If these stresses caused by either cooling or drying shrinkage of the outer zone reach the tensile strength of the concrete, (micro) cracking of the cover concrete is expected to occur.

1.2.2 Eigenstresses in hardening concrete structures – Structural eigenstresses

Already at the very early age stresses are generated in the cross-section of concrete structures. Due to the liberated heat of hydration the temperature of the concrete increases. On subsequent cooling at the concrete surfaces the concrete in the outer zone will shrink. This shrinkage is restrained by the relatively warm inner part of the concrete element. This causes compressive stresses in the inner part and tensile stresses in the outer zone of the concrete (Fig. 1.4). In case of a symmetric temperature distribution and assuming linear elastic material behaviour, the compressive and tensile forces are in equilibrium and the concrete element will not deform. These stresses are called *eigenstresses* and the temperature components that cause these stresses are called *eigentemperatures.*

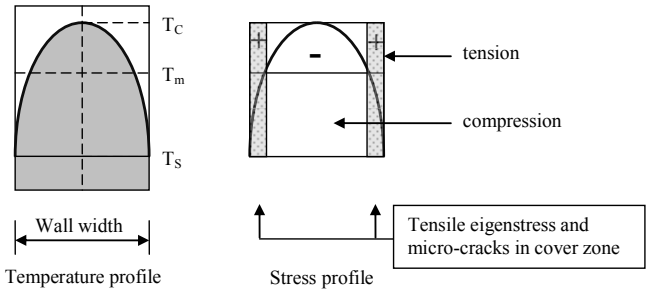

Figure 1.4 Typical distribution of the (structural) eigenstress in a concrete wall due to the heat of hydration and subsequent cooling at the concrete surfaces. T_m = mean temperature.

In the forgoing examples the cross-sections of structural elements are supposed to remain plane (Bernoulli's theorem). The eigenstresses caused by a non-uniform distribution of imposed deformations in a cross-section of a concrete element are called *structural eigenstresses*.

If the tensile stresses in the outer zone reach the tensile strength, (micro)cracking of the cover concrete may occur. These small cracks can reduce the resistance of the concrete against ingress of aggressive substances, like chloride ions and, hence, jeopardise the service life of the structure (Van Breugel et al., 1996).

Imposed strain distributions might also result in tensile structural eigenstress and microcracking in the *core* of the wall. In thick elements this internal microcracking can result in the formation of through cracks.

1.2.3 Material eigenstress

For calculating structural eigenstresses the material is assumed to be homogenous. Concrete, however, is a heterogeneous material. This heterogeneity causes a second type of eigenstress, namely *material eigenstress*. Material eigenstresses are stresses in the cement paste matrix, induced by the restraint of volume changes of the cement paste by aggregate and/or reinforcing bars. Volume changes in the cement paste matrix may originate from the autogenous or drying shrinkage of the cement paste or temperature changes. Typical material eigenstresses and related crack patterns in a shrinking cement paste are shown in Fig. 1.5. The figure shows a crack pattern in a paste of which shrinkage is restrained by a spherical aggregate particle.

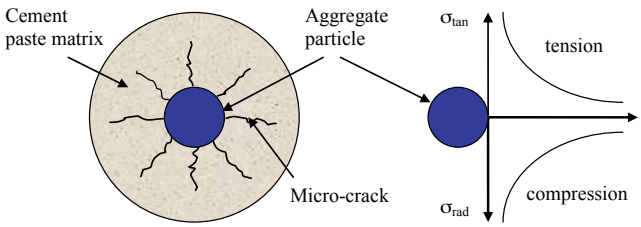

Figure 1.5 Distribution of *material eigenstresses* and microcracks near an aggregate particle due to cement paste volume reduction

1.3 Imposed deformations in the engineering practice

1.3.1 Structures with imposed deformations and eigenstresses

In real structures the structural and material eigenstresses often occur simultaneously and interact with each other. This complicates the determination of eigenstresses. The occurrence of (micro) cracks further complicates an accurate prediction of eigenstresses and their consequences on the performance the structure. This complexity holds already for linear elastic analysis of eigenstresses, but even more in case time-dependent behaviour of the material has to be taken into account. Both (micro)cracking and time-dependent effects, i.e. relaxation, affect the magnitude of the so-called *residual* eigenstresses.

A better insight into the extent of *residual (eigen)stresses*, caused by imposed deformations, is needed for reliable predictions of the probability of cracking and the influence of microcracks on the serviceability and durability of a concrete structure. Typical examples of structures where *residual stresses* might have a negative influence on the serviceability and/or durability are:

- concrete walls of containment structures (silo, basin etc.) from the point of view of liquid and/or gas tightness;

- massive concrete structures (foundation slabs, locks, tunnels) subjected to high temperature differentials (hydration-induced tensile stresses), from the point of view of water tightness;
- concrete slabs (concrete roads, bridge decks etc.) subjected to climate conditions (changing temperature and humidity), from the point of view of durability (chloride ingress);
- industrial concrete floors subjected to combinations of high concentrated loads, dynamic loads and extreme high and low temperatures, from the point of view of liquid tightness.

Already in the execution phase of a project, or later during service life, concrete structures can suffer from unforeseen cracking due to (partially) restrained imposed temperature and shrinkage deformations. Even advanced software tools are not always capable to analyse the impact of *eigenstresses* adequately. In many building codes and standards no directives are given for determining the magnitude and relevance of eigenstresses. As a result eigenstresses are often disregarded in practice.

1.3.2 Design codes

For designing structures with respect to structural design, safety, serviceability and durability, national building codes, guidelines and additional regulations have to be followed. For the design of concrete structures in the European Union, the Eurocode 2 parts 1-1 [EN 1992-1-1+C2:2011], part 2 [EN 1992-2:2005+C1:2008] and part 3 [EN 1992-3:2006] give guidance to engineers for designing concrete buildings and bridges. In Eurocode 2 concrete is considered as a quasi-homogeneous material in which the forces due to the loads acting on the structure may be determined assuming linear-elastic material behaviour. Stresses and strains follow from cross-sectional analyses in which cracking of concrete can be taken into account.

Detailed temperature profiles for the calculation of imposed temperature strain distributions in cross-sections of elements are given in part 1-5 of Eurocode 1 [EN1991-1-5:2003+C1:2011]. For concrete bridges the engineer/designer is referred to part 2 of Eurocode 2 [EN 1992-2:2005+C1:2008]. Rules are given to account for the relaxation of the stresses caused by temperature effects and shrinkage on *macro-level*, in which case concrete is assumed to be a homogeneous material. For detailed analysis of (residual) eigenstresses and (micro)cracking at the *meso-scale*, design codes generally give little or no guidance.

1.4 Resume and research questions

The magnitude of residual eigenstresses is influenced by stress relaxation and microcracking in the cement paste matrix. As stated in the state-of-art report of RILEM TC-122-MLC on microcracking and life-time performance of concrete: *"it would be highly desirable to carry out some systematic work on how a system of microcracks develops over time under particular environmental conditions"* (Jensen et. al., 1996). For the prediction of the magnitude of residual eigenstresses and the associated probability of microcracking in concrete the following questions require further attention:

- what is the role of relaxation of eigenstresses in the cement paste?

- what is the role of microcracking on the evolution of (residual) eigenstresses?
- what is the role of aggregate properties on the intensity of microcracking?

A follow-up question concerns the impact of microcracking on the protective function of the concrete cover. Microcracks in the concrete cover are supposed to promote the ingress of aggressive substances into the concrete. Quantification of the effect of microcracking on transport properties is an intriguing question, particularly when it comes to the chloride diffusion coefficients applied in service life predictions of concrete structures. Progressive microcracking would result in an *increase* of the diffusion coefficient, whereas in practice the diffusion coefficient is generally assumed to *decrease* with elapse of time. Experiments performed by Taheri-Motlagh (1998) on chloride ingress into concrete beams showed the promotion of chloride penetration into the concrete in case the chloride penetration took place in the presence of temperature and shrinkage-induced microcracks. Other test results also showed that the chloride diffusivity of concrete increases exponentially with the microcrack damage of the cement paste (Tegguer et al., 2013).

To answer these questions a better understanding of the magnitude and development over time of eigenstresses and microcracking in the cement paste matrix in concretes is needed. The resulting research questions are:

- What is the effect of relaxation on the evolution of eigenstresses?
- How to calculate residual eigenstresses and microcracking in concrete?
- How to judge the effect of microcracking on transport properties in concrete?

In this study the focus will be on eigenstresses and microcracking caused by *drying shrinkage* of *hardened* concrete.

1.5 Research strategy

The aim of this research is to investigate and quantify, by numerical simulation, the effect of relaxation on the magnitude of *residual eigenstresses* and *microcracking* in the cement paste matrix and to analyse the influence of microcracking on the durability of concrete. The research is subdivided in the following activities:

1. Literature study, with a special attention to:
   - current engineering approaches for predicting the eigenstresses in concrete caused by cement paste shrinkage;
   - inventory of models/methods for analysing eigenstresses;
   - inventory of ‘white spots’.
2. Development of a method for determination of the effect of relaxation on shrinkage-induced eigenstresses in cement paste in concrete.
3. Incorporation of stress relaxation in a numerical method for calculating eigenstresses in concrete.
4. Analysis of the evolution of eigenstresses, microcracking and crack patterns due to an imposed shrinkage strain with special attention for the influence of the following parameters:
   - cement paste stiffness;

- bond strength between aggregate and matrix;
- aggregate stiffness;
- aggregate particle size, aggregate volume fraction (AVF) and particle size distribution (PSD);
- sensitivity of results (stresses, cracking) for the magnitude of relaxation;
- sensitivity of results (stresses, cracking) for the rate of imposed shrinkage.

5. Evalution of the effect of microcracking on the transport properties of concrete exposed to imposed deformations.

The analyses are carried out without and with relaxation of eigenstresses in the cement paste and for different kinematic boundary conditions: full restraint (structural restraint) and (only) material restraint (free boundaries of a small numerical specimen).

1.6 Outline of thesis

In chapter 2 the state-of-art knowledge of eigenstresses in concrete is described. Recent literature about eigenstresses and microcracking in concrete is reviewed. The determination of eigenstresses and microcracking with a lattice model is discussed.

Chapter 3 gives a description of a numerical tool developed for non-linear analyses of eigenstresses and microcracking in concrete. The concrete is modelled at meso-level as a three-phase material (aggregates, cement paste matrix and the Interfacial Transition Zone - ITZ). An extended two-dimensional beam lattice model (BLM) is developed in which the relaxation of eigenstresses is incorporated.

In chapter 4 the proposed method used for the calculation of stress relaxation in cement paste is described. The approach is based on the activation energy method by which creep deformation and stress relaxation of hardened cement paste can be described.

The results of the numerical analysis of eigenstresses and microcracking in specimens with different mix compositions are reported in chapter 5. The influence of boundary conditions for structural and material eigenstress and concrete mix compositions is analysed.

In chapter 6 the proposed method for the prediction of microcracking in concrete is used for quatification of the effect of microcracking on transport properties. The calculated effect of microcracking on transport properties is compared with transport properties inferred from chloride profiles in concrete elements exposed to thermal and hygral cycles.

In chapter 7 the different aspects influencing the formation of eigenstresses and microcracks are evaluated and conclusions are drawn. Conclusions are presented with respect to the magnitude of residual eigenstresses and microcracking in concrete.

In figure 1.6 an overview of the outline of the thesis is given.

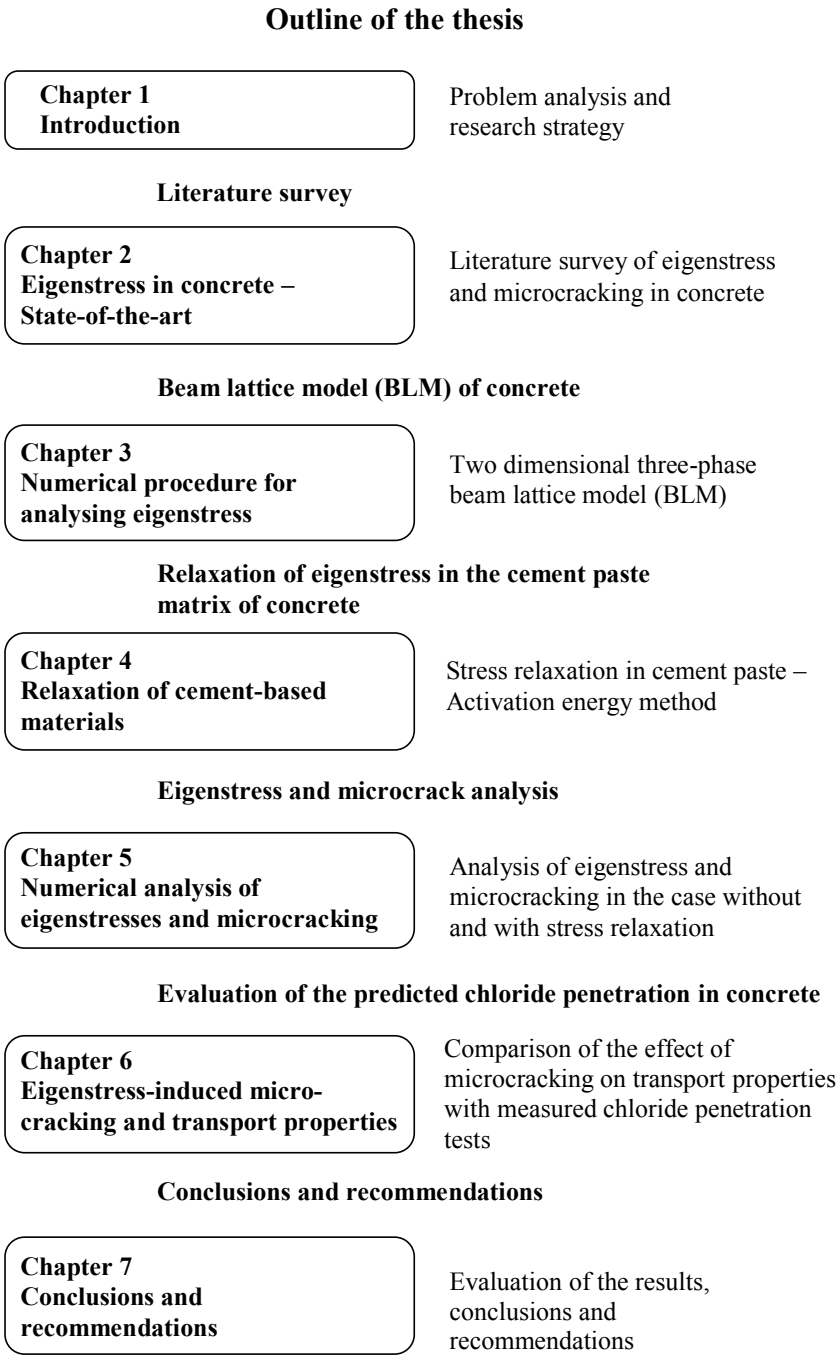

Figure 1.6 Outline of the thesis

Chapter 2

2. Eigenstress in concrete – State-of-the-art

Following the preliminary remarks on eigenstresses in chapter 1, this chapter summarizes the results of research on the role of eigenstresses in concrete structures. The way designers have addressed the issue of eigenstresses is reviewed, including methods for quantitative analysis of eigenstresses and subsequent (micro)cracking in case eigenstresses reach the tensile strength of the cement paste. Attention will be paid to the effect of relaxation on the magnitude of eigenstresses and to which extent relaxation has been considered in the determination of eigenstresses. The role of microcracking of the cement paste on strength and stiffness of the concrete and the impact of cracking on the transport properties and durability will be addressed.

2.1 Concept of eigenstress

The original German term 'Eigenspannung' was first used by Reissner (1931). *Eigenstresses* are induced by *eigenstrains* in the cross-section of structural elements. By definition these eigenstrains do not result in any deformation of the structural element, except close to the ends of the element where Bernoulli's theorem (plane sections remain plane) does not apply. Mura (1982) has defined eigenstresses as the *self-equilibrating internal stresses* caused by one or several eigenstrains in bodies that are free from any other external force and surface constraint.

Eigenstresses are always present in concrete. Their magnitude, however, is often not known and even not considered in the prediction of the performance of concrete structures. Ignoring the presence of eigenstresses implies that the actual stresses in the concrete differ from those that are calculated or assumed. A higher tensile stress level implies a higher susceptibility to microcracking, which may result in a lower durability than assumed. In a general discussion on eigenstresses in engineered products Jun et al., (2010) stated that uncontrolled residual stresses are detrimental to the performance of a product. Jun considers residual stress as one of the mechanisms through which processing significantly affects the quality, durability and mechanical response of engineered components. In the context of economical effectiveness, he said, appropriate residual stress assessment can lead to substantial savings and improved integrity of products. One of the reasons why residual eigenstresses are easily overlooked or totally disregarded is that these stresses cannot be measured directly, he said.

The fact that Jun spoke about *residual* eigenstresses implicitly points to the effect of *relaxation* on the magnitude of eigenstresses. Knowing that relaxation is a phenomenon that is always there and that it will result in a decrease of eigenstresses, might make people reluctant to pay much attention to the role of eigenstresses. However, as long as the actual

magnitude of residual eigenstresses is unknown, it is not justified to ignore these stresses. Jun's statements on the importance of residual eigenstresses for the performance of engineering products, therefore, still applies, also to concrete structures.

2.2 Eigenstresses in concrete structures

2.2.1 Origin and consequences of structural eigenstresses

In chapter 1 the main characteristics of eigenstresses have been briefly addressed yet. Typical for eigenstresses is that these stresses are present in the cross-section of a concrete element, but are not associated with macroscopic deformations of a structure or structural element, i.e. no bending and no axial elongation.

Eigenstresses occur when a *non-uniform* strain field is generated in a cross-section of a structural element. A non-uniform strain field may occur as a result of the liberation of heat of hydration in hardening concrete and subsequent cooling. Other examples are one-sided heating or cooling of a structure due to temperature changes of the environment or drying shrinkage. In the hardening stage of young concrete also autogenous shrinkage strains may lead to (eigen)stresses.

Daily temperature changes of the environment result in heating and cooling of the surface zones of concrete structures. The surface zones that experience temperature variations expand or shrink. The temperature-induced deformations are restrained by the part of the structure of which the temperature remains constant. In massive structures the outer zone can conservatively be considered as fully restrained by the interior of the structure. Situations of full restraint are schematically shown in figure 2.1

The imposed thermal strains result in compressive and tensile stresses in the outer zone of the structure on heating and cooling, respectively. One-sided drying out of the surface zone of concrete structures will also result in tensile stresses in this zone. If tensile stresses in

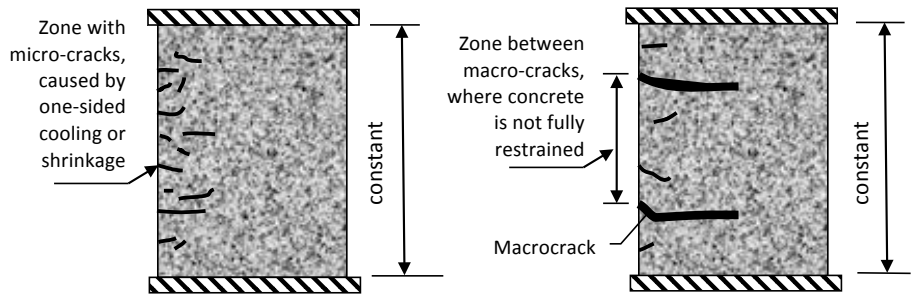

a. Microcracking in outer zone b. Micro- and macro-cracking in outer zone

Figure 2.1 Concrete elements, subjected to one-sided cooling or drying shrinkage. Full restraint of the imposed deformations. Left: microcracking in the zone subjected to shrinkage. Right: Formation of large (macro)cracks. Concrete between macrocracks is no longer fully restrained.

the outer zone, caused by cooling and/or drying, reach the tensile strength, cracking is likely to occur. Depending on the imposed strain gradients and eventual rebar configuration, micro- or macrocracks will occur, or a combination of them. In case macrocracks are formed, the concrete between the macrocracks is no longer fully restrained. Further cracking of the concrete between macrocracks will be dominated by the properties of the aggregate (materials eigenstresses, see section 2.3).

Among the consequence of eigenstresses the formation of cracks in the surface zone of concrete structures is the most discussed one. Microcracks may jeopardise the durability and service life of reinforced concrete structures (Ujike et al., 2010). This is the reason why in this thesis emphasis will be on microcracking and the consequences thereof for the performance of the surface zone of concrete structures.

2.2.2 Magnitude of eigenstrain and eigenstress – Preliminary comments

Eigenstrains originate from thermal loads or drying of the concrete. Thermal strains follow from a temperate differential ΔT and the coefficient of thermal expansion α_{cT}. The coefficient of thermal expansion (CTE) of *concrete* strongly depends on the type of aggregate used. Values may range between $0.8 \cdot 10^{-5}$ and $1.2 \cdot 10^{-5}$ m/mK. For a value of $1.0 \cdot 10^{-5}$ m/mK a temperature differential of 10 K will generate a strain of $0.1 \cdot 10^{-3}$ m/m. For an ordinary concrete with a E-modulus of 30,000 MPa, a strain of $0.1 \cdot 10^{-3}$ m/m will result in a stress of 3 MPa. For these values of tensile strain and stress a concrete is about to crack. In practice eigentemperatures can easily exceed the aforementioned value of 10 K. This means that the occurrence of microcracking due to thermal eigenstresses is certainly conceivable and even almost unavoidable.

Strains due to drying shrinkage depend on the type of concrete and relative humidity in the concrete. The shrinkage coefficients for concrete given in design codes implicitly take into account the restraining effect of the aggregate particles in the concrete. In fact the *shrinking cement paste* is the component in the mixture that causes the concrete to shrink. The final shrinkage strain of ordinary concretes, exposed to an environment with a RH of about 70% may vary between $0.2 \cdot 10^{-3}$ and $0.3 \cdot 10^{-3}$ m/m. (Eurocode 2 part 1-1 (2011)). This (tensile) strain is two to three times the tensile strain capacity of the concrete. Hence, in practice the outer zone of most concrete structures are likely to suffer from microcracking.

2.2.3 Crack criteria

As discussed in the previous section, eigenstresses might result in microcracking of the concrete. In a deterministic approach cracking is assumed to occur when *tensile strain criteria* or *tensile strength criteria* are reached. For judging the probability of cracking due to thermal loads *temperature criteria* have been proposed in terms of maximum allowable temperature differentials (Röhling 2005, Bamforth 2007).

2.2.3.1 Strain criterion

When dealing with strains induced by imposed deformations, the use of a tensile strain capacity (ε_{ctu}) of concrete seems advantageous. In case of imposed deformation not the peak stress

during application of the strain, but the ultimate strain capacity of the concrete determines the occurrence of failure (see Figure 2.2). The tensile strain capacity is the maximum tensile strain that the concrete can withstand without the occurrence of a continuous crack (Bamforth 2007).

The tensile strain capacity of concrete depends on a number of factors like: strength class, modulus of elasticity and concrete age. Moreover, the tensile strain capacity of concrete is very sensitive to the strain rate (Carlson et al., 1979). The tensile strain capacity of concrete under slow loading is about $0.13 \cdot 10^{-3}$ m/m in case of gravel aggregate and $0.18 \cdot 10^{-3}$ m/m in case of crushed rock aggregate (Bamforth 2007). Eurocode 2 part 1-1 recommends a mean value of $0.10 \cdot 10^{-3}$ m/m for the tensile strain capacity under sustained short term loading. In a strain controlled test the post-peak behaviour was found to be substantially affected by, for example, the particle size distribution of the aggregate (Unger et al., 2011).

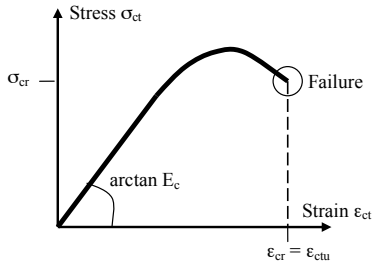

Figure 2.2 The strain criterion for a non-linear elastic stress-strain relation for concrete loaded in tension. Criterion for cracking: $\varepsilon_{ct} = \varepsilon_{cr}$

2.2.3.2 Strength criterion

The most commonly used criterion for cracking of concrete is the concrete tensile strength. The probability of cracking with corresponding safety coefficient can be expressed as a function of the mean value of the sound concrete tensile strength (f_{ctm}) (Fig. 2.3). In this approach the cracking stress with a certain probability is written as: $\sigma_{cr} = \beta\ f_{ctm}$, in which the value of β ranges from 0.5 (crack probability 0.02%) to 0.85 (crack probability 50%). In a deterministic approach a value $\beta = 0.6$ is proposed in the case of sustained (imposed) loads

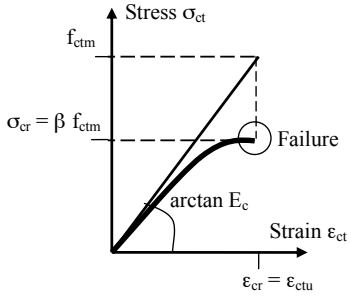

Figure 2.3 The strength criterion in the case of a non-linear elastic stress-strain relation for concrete loaded in tension. Criterion for cracking: $\sigma_{ct} = \sigma_{cr}$

(Van Breugel et al., 1996). The strength criterion is used when concrete is considered to perform as a non-linear elastic material (see Fig. 2.3).

2.2.3.3 Temperature criterion

The 'temperature criterion approach' is equivalent with the tensile strain capacity approach. The imposed strain is a function of the temperature differential (ΔT) and the coefficient of thermal expansion α_{cT}: $\varepsilon_{cT} = \alpha_{cT} \Delta T$. This strain should not exceed the tensile strain capacity of the concrete.

Temperature criteria have been used for estimating the probability of thermal cracking of hardening concrete elements (walls, slabs) (Röhling 2005, Bamforth 2007). The use of temperature criteria presupposes that thermal strains are the only reason for cracking. In practice, however, additional strains caused by autogenous shrinkage substantially contribute to the probability of cracking. In situations where thermal strain and autogenous shrinkage occur simultaneously temperature criteria are not applicable for crack risk analyses and only the *strain criterion* is applicable (Bamforth 2007).

2.3 Materials eigenstresses - Meso-level

2.3.1 A 'single particle – paste' system

In section 2.2 the effect of eigenstresses on concrete elements was discussed, whereby concrete was assumed to be a *homogenous* material. As mentioned in section 1.2.3 concrete is a *heterogeneous* material, of which the properties of the individual components may differ. They differ in, for example, strength and stiffness, but also with respect to their response on thermal and hygral loads. In concrete, aggregate particles are generally stiffer than the cement paste. If the cement paste shrinks or expands, the stiff aggregate particles (partially) restrain the free deformations of the paste, which results in stresses in the cement paste and in the restraining aggregate particles. Stresses due to *internal restraint* on the meso-level are called *material eigenstresses* .

A schematic picture of *material eigenstress* is shown in figure 2.4.

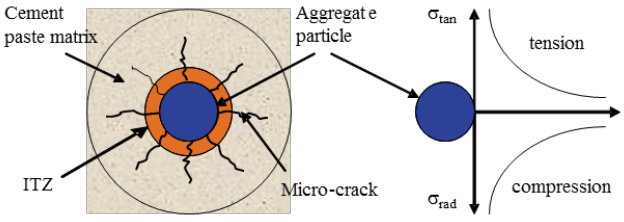

Figure 2.4 Microcracks near an aggregate particle due to the tensile material eigenstress in tangential direction caused by a shrinking cement paste. In case the 'aggregate-paste system' is loaded in tension, the weaker interfacial transition zone (ITZ) may dominate the cracking process.

This figure is almost identical with figure 1.5, except for the presence of an additional component, i.e. the interfacial transition zone (ITZ) between the aggregate particle and the matrix. In ordinary concrete the ITZ-paste is more porous than the bulk paste and has a lower stiffness and strength than the bulk paste. When loaded in tension, the tensile strength of the material is generally dominated by the mechanical properties of the ITZ (Unger et al., 2011).

2.3.2 The effect of aggregate on shrinkage of concrete mixtures

2.3.2.1 Effect of aggregate volume fraction on shrinkage and microcracking

Already in 1937 Carlson (1937) pointed out that the magnitude of shrinkage and the associated risk of (micro)cracking of concrete depend on the magnitude of the imposed strain of the cement paste and on the size of the aggregate particles and the aggregate volume fraction in the mixture. Based on Pickett's (1956) work, Hansen et al., (1965) developed a graph in which the shrinkage of a concrete mixture, with the cement paste as the shrinking component, was presented as a function of the aggregate volume fraction (Fig. 2.5).

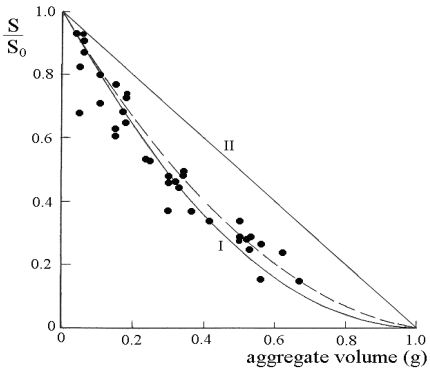

Figure 2.5 Ratio of concrete shrinkage (S) and cement paste shrinkage (S_0) as function of the aggregate volume fraction g (=V_a) in concrete mixtures (Hansen et al., 1965).

The ratio concrete shrinkage / cement paste shrinkage is in the order of 1/7 for concrete strength class C55/67 to 1/6 for C20/25. The lower shrinkage of concrete compared to the shrinkage of cement paste is caused by the restraining effect of aggregate. Shrinkage of the cement paste will be (partially) restrained by the aggregate, causing tensile stresses in the paste and compressive stresses in the aggregate particles. In case tensile stresses reach the tensile strength of the paste, microcracking will occur, which on its turn affects the resulting macroscopic shrinkage strain. The occurrence of stresses will also cause strains that are subject to *creep*. These creep strains further complicate the quantification of the shrinkage of heterogeneous materials.

2.3.2.2 Effect of aggregate size

The effect of aggregate grading and particle size on the performance of concrete has been studied for decades. In the past the focus of those studies was often on the design of mixtures with optimal mechanical properties. More recently the focus is on the role of aggregate characteristics on the susceptibility to microcracking and loss of durability. Grassl et al., (2010) studied the influence of the aggregate size and aggregate volume fraction on shrinkage-induced microcracking. In a numerical study aggregate diameters from 2 mm to 16 mm were considered and volume fractions of the aggregate between 0.1 and 0.5. They found an increase of the crack width with increasing aggregate diameter (at equal volume fraction) and with decreasing aggregate volume fraction (at equal aggregate diameter). Idiart et al., (2011) reported a larger degree of internal microcracking with increasing aggregate diameter and aggregate volume fraction. Fabien et al., (2012) found lower compressive strength for concretes made with larger aggregates.

2.3.3 Materials eigenstresses due to chemical and autogenous shrinkage

In the hardening stage of concrete the cement paste will shrink due to chemical shrinkage. Chemical shrinkage, however, is largely transformed into *internal porosity* and *internal drying* of the cement paste. The self-desiccation process is accompanied by autogenous shrinkage. At the time autogenous shrinkage strains emerge, the cement paste is stiff enough to create substantial stresses, supposed that the strains are restrained. In this case the aggregate is the restraining component in the mixture. Autogenous shrinkage can be an important cause of material eigenstresses in concrete mixtures with a low water-cement ratio (Emborg 1998). Schlangen et al., (2004), studying the formation of eigenstresses due to autogenous shrinkage, reported that microcracking caused by autogenous shrinkage may result in a reduction of the tensile strength of concrete by 15% in mixtures with w/c = 0.3.

As said (section 2.2.2), the cement paste is the component that either shrinks or expands and is, as such, the driving force behind the occurrence of *structural eigenstresses*. On top of the (drying) shrinkage, the cement paste is also restrained by the aggregate particles, which creates additional *material eigenstresses.* Little research has been devoted to the magnitude of the eigenstresses in the cement paste caused by the combination of material and structural eigenstresses and the role of stress relaxation. There is no doubt, however, that these eigenstresses caused by drying shrinkage are high enough to cause (micro) cracking of the cement paste.

2.4 Effect of eigenstress on performance of concrete structures

2.4.1 Microcracking

The presence of eigenstresses *as such* is not considered a big problem. Tensile eigenstrains, however, can easily exceed the tensile strain capacity of the concrete, followed by cracking of the concrete. Depending on the origin of the eigenstresses the generated cracks are either small microcracks or wider macrocracks. Microcracking is a typical result of material ei-

genstresses. Microcracks are defined as cracks with a width up to 0.1 mm and a length up to 5 mm (Neville 2010). With increasing magnitude of the eigenstresses initially isolated microcracks may become connected, forming a macro-crack that facilitates the penetration of water and/or aggressive substances into the concrete and enhances the risk of corrosion of reinforcing steel (Emborg 1985,1989,1998, Emborg et al., 1994, Larson 2000, Yang et al., 2005).

Microcracking may also happen in case of compressive stresses. When loaded up to about 60% of the maximum load microcracking may start to occur (Sluijs 1992, Hofstetter et al., 1995). Compressive eigenstresses, however, are generally not consideredas problematic for their effect on durability.

2.4.2 Cracking and crack width criteria

Crack width criteria in design codes have been defined in order to ensure that reinforced or prestressed concrete structures will last for the required service of the structure without excessive maintenance. Most important reasons for defining crack width criteria are preventing premature rebar corrosion (Alexander et al., 2012) and preventing or controlling leakage through cracks.

Although cracks are almost always considered as weak points in the protection of reinforcing steel against corrosion, opinions still differ about the allowable crack widths. According to Leonhardt (1987) cracks < 0.4 mm do not significantly harm the corrosion protection if the concrete cover is sufficiently thick and dense. Cracks > 0.4 mm should be avoided just for appearance or image sake. Leonhardt's precondition of a sufficiently thick and dense concrete cover is crucial here. In case structures are subjected to thermal or hygral eigenstresses, microcracking of the concrete cover is almost unavoidable. The question is then which degree of microcracking is still acceptable for ensuring adequate protection against rebar corrosion. No studies have been found, however, for acceptable crack widths of microcracks or the level, or intensity, of microcracking.

Crack width criteria strongly depend on the relevant exposure conditions. There is, therefore, not such a thing as a crack width criterion that holds for all conceivable situations. Once crack width criteria have been defined for a particular situation, the next question should then be how to determine and judge the role of microcracking in the concrete between the macrocracks in service life predictions.

2.4.3 Microcracking and transport properties - Permeability

In concrete technology the presence of microcracks is not considered a point of concern per se. Microcracks are to be considered as an inherent feature of concrete (Covarrubias 2007). The presence of (micro)cracks, however, does affect the transport properties of concrete. Microcracks promote the connectivity of pores in the concrete and contribute dramatically to the permeability (Hearn 1999). According to Yang et al., (2005) microcracks caused by material eigenstress are well-distributed and do have effect on the transport properties of the concrete, while Mu et al., (2013) emphasized that microcracking caused by internally restrained deformations reduces the efficiency of concrete as a barrier against aggressive agents. Grassl et al.,

(2012) found an increasing permeability with increasing size of aggregate particles. An increase of the aggregate diameter from 2 mm to 16 mm caused an increase of the permeability by approximately a factor 2.5. For a constant aggregate size an increase of the aggregate volume from 10% to 50% caused an increase of the permeability by about 1 order of magnitude.

Wang et al., (1997) found little influence of microcracks on permeability for crack widths smaller than 50 μm. For crack widths between 50 to 200 μm, the permeability increased substantially. Wang et al., (2001) studied the effect of compressive stress on the permeability. For compressive stresses below 40% of the compressive strength the effect of a compressive stress was very small. For stress levels higher than 40 to 50% of the compressive strength, the permeability started to increase more rapidly. An increase of permeability caused by load-induced microcracking was also found by Zhao (2006). In an experimental study Fabien et al., (2012) found that concrete specimens subjected to 30%, 60% and 80% of the maximum compressive strength exhibit for all load levels a higher permeability the larger the aggregate used. From a review of literature and own research on the effect of load on transport properties Niu et al. (2008) concluded that experiments on non-loaded specimens *cannot* reflect the real state of a structure and that concrete structures subjected to loads are less durable than those without loads. A similar statement was made by Melchers et al., (2006), who made this statement based on an analysis of reinforcement corrosion in marine structures.

Yang et al., (2008) studied the water permeability of concrete beams while subjected to bending. The side of the beam with tensile stresses was exposed to water. Water permeability was measured for 4 levels of flexural load: 0, 0.3, 0.5 and 0.7 times the crack load. It was found that the permeability coefficient increased significantly when load levels exceeded 0.3 times the flexural strength of the beam. The effect was more pronounced for concrete with low w/c (w/c from 0.45 to 0.65).

Tawfiq et al., (1996) found an increase of permeability in case of cyclic loading. Taheri-Motlagh (1998) found enhanced ingress of chloride ion in concrete subjected to combined thermal and hygral eigenstresses. In a numerical study Wang et al., (2015) found that cyclic drying-wetting of the concrete plays a crucial role on the chloride content in specific positions in the concrete. Desmettre et al., (2013) studied the effect of cyclic loading and self-healing of cracks on permeability. Cyclic loads were found to increase permeability, but self-healing was found to be a compensating phenomenon, even in case of a cyclic loading.

2.4.4 Effect microcracking on diffusion and chloride diffusion coefficient

In an extensive literature survey Marchand et al., (1998) showed that relatively little research had been conducted on the influence of cracking on diffusion properties of concrete. Moreover, published research results on the subject were contradictory. In studies of Samaha et al., (1992) cracking was found to affect the diffusivity of concrete, whereas experimental and theoretical work of Daian et al., (1993) and Locoge et al., (1992) suggested only little influence of cracking on diffusion. Gerard et al., (2000) found that the presence on continuous cracks tends to markedly modify the transport coefficient: diffusivity increased by a factor 2 to 10. The effect of cracking on diffusivity was relatively more important for dense materials. In a study on the influence of the aggregate size and aggregate volume on shrinkage induced

microcracking Grassl et al., (2010) found that diffusivity was less sensitive to microcracking than permeability.

Tegguer et al., (2013) studied the effect of microcracks on the ingress of chlorides in concrete. This effect was measured on concrete specimens in which microcracks were generated using a uniaxial compression test. From these experiments, carried out with the Cembureau permeameter, conclusions were drawn regarding the chloride diffusion coefficient. It was found that for a virgin, unloaded concrete the diffusion coefficient is $1.88 \cdot 10^{-12}$ m^2/s for ordinary concrete (OC) and $0.67 \cdot 10^{-12}$ m^2/s for high performance concrete (HPC). In specimens with a compressive load as high as 90% of the compressive strength, applied during 2 hours, the diffusion coefficient for OC is $5.74 \cdot 10^{-12}$ m^2/s and for HPC $1.28 \cdot 10^{-12}$ m^2/s. The increase of the diffusion coefficient was attributed to the generated microcracking under sustained load.

The effect of microcracks caused by sustained loading on chloride transport in concrete was recently studied by Wang et al., (2016). Stress levels up to 75% of the ultimate compressive load were applied to concrete disks with a diameter of 100 mm and chloride migration was measured with a test setup based on the NT BUILD 492. Ultrasonic pulse velocity (UPV) tests (ASTM C597, 1997) were conducted before and after the loads were applied. The results of the tests are plotted in figure 2.6, where the influence of microcracking on the normalised diffusion coefficient is shown as a function of the damage degree. The degree of microcrack damage D_{UPV} was calculated with the formula:

$$D_{UPV} = \frac{v_0 - v}{v_0} \tag{2.1}$$

with v_0 the pulse velocity in the material before loading and v after loading.

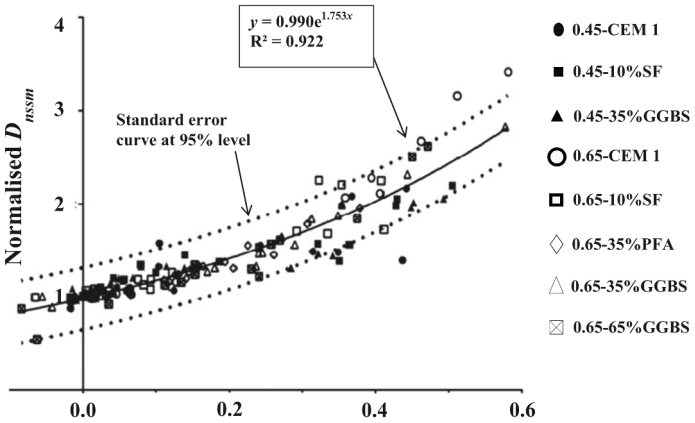

Figure 2.6 Relationship between the damage degree based on UPV measurements and the normalised non-steady state chloride migration coefficient (Wang et al., 2016).

Bernard et al., (2010) performed numerical analysis on ion diffusivity of concrete loaded in tension and compression. Numerical stress-strain curves were generated in strain-controlled tests. For the thus loaded (and microcracked) samples, numerical diffusion tests were performed. It was concluded that due to cracking the diffusivity increased by a factor 1.1 just before the peak load was reached and by a factor 2.8 just after the peak load. These values were considered in good agreement with comparable experimental results of Tognazzi (1998), who found corresponding values of 1.3 and 1.9 just before and just after reaching the stress peak.

Figure 2.6 shows how the rate of diffusion increases with increasing degree of damage. This microcrack-induced damage is generally assumed to *increase* with elapse of time. In the engineering practice, however, diffusion coefficients used for service life predictions suggest another trend. With elapse of time chloride diffusion coefficients D(t) are assumed to *decrease* with time according to the empirical equation:

$$D(t) = D_0 \left(\frac{t_0}{t} \right)^n \tag{2.2}$$

where D_0 [m^2/s] is the initial diffusion coefficient at time t_0 and n an ageing factor < 1. The ageing factor depends on the type of cement and water-binder ratio. For concrete made with Portland cement with silica fume percentages from 0 to 10%, Markeset et al., (2010) reported n-values from 0.1 to 0.59. For Portland cement concrete blended with up to 35% fly ash n-values between 0.1 and 0.52 were found. These values where calculated n-values from Norwegian field studies. For fly ash concrete, with fly ash percentages from 10% to 50% and w/b ratios from 0.4 to 0.6, Yu (2015) found n-values between 0.8 to > 0.9.

Even though the n-values fall in a wide range from 0.1 to almost 1.0, they all have in common that they result in a decrease of the diffusion coefficient over time. This suggests that with elapse of time the concrete becomes denser and obviously does not suffer from microcracking. In laboratory studies on carefully prepared samples it is plausible that microcracking of the concrete has been excluded. In real structures, which are exposed to imposed thermal and hygral loads, however, the absence of any effect of microcracking is less obvious. Nilsson (2012) has mentioned chloride binding as a possible explanation for a decreasing apparent diffusion coefficient over time. Whether chloride binding can compensate the diffusion-enhancing effect of microcracking, however, is still to be established. Chloride binding as a possible cause for decreasing diffusivity over time has also been put forward by Mohammed et al., (2004). Besides chloride binding also self-healing of cracks was mentioned as a reason for densification of the outer zone of concrete structures.

In a study on the effect of cracking on the chloride content in concrete bridge decks Lindquist et al., (2006) observed an increasing crack density in more recently constructed bridges. This higher crack density was attributed to changes in the material properties and construction procedures over the past 20 years (period 1980 – 2000). The presence of cracks was found to increase the chloride content in the concrete. A higher chloride penetration depth was found in case of more intensive traffic, i.e. more load cycles. Deeper penetration of chlo-

rides into concrete exposed to cyclic loading was also observed by Küter et al., (2005) and Taheri-Motlagh (1998).

2.5 Determination of eigenstress

2.5.1 Determination of structural and materials eigenstresses

Quantitative analysis of eigenstresses starts with the determination of the strain fields caused by either thermal or hygral loads in concrete elements or structures. Once these strain fields and the kinematic boundary conditions are known, linear elastic stress analyses can be carried out with appropriate computer packages. These analyses become more complicated when stress levels have been reached high enough to cause cracking of the concrete and/or time-dependent materials properties have to be taken into account. Hence, for more detailed analysis of fracture processes caused by eigenstresses more sophisticated methods have to be used. In fact (micro) cracking of the concrete and the effect of time-dependent materials properties on the cracking process are the subject of this thesis.

2.5.1.1 Structural eigenstress

For determination of *structural* eigenstresses, concrete is generally considered to be a homogenous material. Finite Element Methods (FEM) and Finite Layer Methods (FLM) are widely used for quantitative analysis of eigenstresses in both hardening and hardened concrete. FLM analysis have often been used for the determination of stresses and probability of cracking in hardening concrete structures (Röhling 2005, Rostásy et al., 1998, Gutsch et al., 1994, Traute 1994). The FLM is schematically shown in figure 2.7.

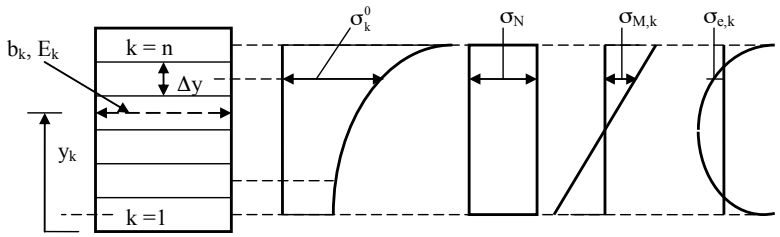

Figure 2.7 FLM approach for stress calculation in a cross-section, divided in n layers (thickness Δy), each with its own width b_k and own modulus of elasticity $E_{k,i}$ at each time t_i. $\sigma_{e,k}$ is the structural eigenstress.

During hydration the strength and stiffness of individual layers can be calculated as function of the degree of hydration. To allow for time-dependent behaviour of the material simplified approximations have been proposed, for example arbitrary reductions of the modulus of elasticity. Besides these simplified approaches, creep and relaxation formulas have been pro-

posed as function of the continuously changing degree of hydration (Van Breugel 1980, Eberhardt 1993, Töllner 1995, Lokhorst 2001). For determining the probability of cracking these authors compared the calculated (tensile) stresses with calculated tensile strength (assuming normal distribution for both stress and strength). The effect of relaxation on the evolution of the hydration-induced stresses was found to be significant. The calculations of the probability of cracking are generally not extended to a detailed evaluation of the post-peak stage of the cracking process.

2.5.1.2 Material eigenstress

The linear elastic material eigenstress close to an aggregate particle can be calculated with the theory of Lamé, as has been described by Timoshenko et al., (1970). All the analytical calculation models, like the model of Pickett (1956), the extended Pickett model of Hansen et al., (1965), Hobbs' C&CA model (1974) and the model of Hansen (1987) for the prediction of drying shrinkage of concrete have in common that they all are based on the linear elastic law and do not take into account reduction of stress due to either relaxation or microcracking. The effect of the interfacial transition zone (ITZ) on the cracking process is generally ignored in these models. Unger et al., (2011), however, strongly emphasized the importance of the ITZ to acquire realistic results from numerical studies. Orta et al., (2014) emphasized the importance of creep effects in analysis of local stresses in concrete subjected to restrained shrinkage. Neglecting creep strains would result in predicting very large and unrealistic tensile stresses. When analyzing the effect of creep one should realize that typical creep factors mentioned in design codes refer to average (macroscopic) creep strains. Those creep factors are not appropriate for analyses of the effect of creep of the matrix in concrete on material eigenstress.

2.5.2 Numerical models for analysing material eigenstresses

2.5.2.1 Finite element analysis

The finite element method (FEM) is a technique developed for numerical analyses of complex problems in structural mechanics. As such it is an appropriate method for analyzing the performance of brittle, heterogeneous materials at the mesolevel. At the Swiss Federal Institute of Technology the Numerical Concrete Concept (NCC) program has been developed by Roelfstra (1989). This NCC program was among the first FEM programs – if not the first - for analyzing fracture processes at the meso-scale. With the NCC program the effect of a number of mixture parameters on the performance of the mixture can be investigated, like strength of the matrix, aggregate properties and the presence of the matrix-aggregate interfacial zone (ITZ) (Sadouki et al., 1988, Wittmann 2008). The importance of reliable modeling of the ITZ was also emphasized by Unger et al., (2011). Unger also compared the results of 2D and 3D modelling of the performance of the concrete. He concluded that results obtained with 2D-models were already in good agreement with experimental results. Idiart et al., (2011) used a meso-mechanical 2D finite element model for hygro-mechanical coupled analysis of drying shrinkage of concrete. He used his model for investigating the effect of the

aggregate size on the drying-induced crack pattern and obtained a good agreement between simulated and experimental results.

2.5.2.2 Lattice models

Lattice models are an alternative for finite element models. A two-dimensional lattice model has been developed by Schlangen (1993), known as the Delft Beam Lattice Model (Delft-BLM). In this approach the concrete is represented at the meso-level by a system of (lattice) beams. Properties of the different components of the concrete are assigned to beams representing these components. So, there are beams that represent the aggregate, the bulk cement paste and the paste-aggregate interfacial transition zone (ITZ). Figure 2.8 shows a schematic picture of the geometry of a beam lattice structure (a), the beam forces (b) and the stress-strain relation of cement paste beams as adopted in the analyses (c). Analyses are possible in 2D and 3D. Schlangen (2008) used the 3D lattice model for modelling the fracture process in a uni-axially loaded 'concrete' (i.e. mortar with spherical aggregate particles), and found a good agreement between simulated crack patterns and the crack patterns obtained with a CT-scanner.

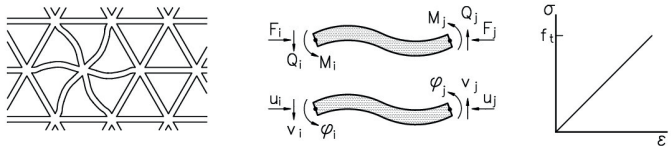

Figure 2.8 Delft Beam Lattice Model (a), forces and degrees of freedom (b), stress-strain relation of cement paste beams (c) (Schlangen 1993).

Jankovic et al., (2001) used a lattice model for the analysis of microcracking in concrete caused by (drying) shrinkage. Also Grassl et al., (2010) used a lattice model for analyzing shrinkage-induced cracking of concrete and the effect of microcracking on permeability. In his analysis aggregate particles were considered of 2, 4, 8 and 16 mm. The shrinkage was represented as an eigenstrain, which was uniformly applied to the cement matrix.

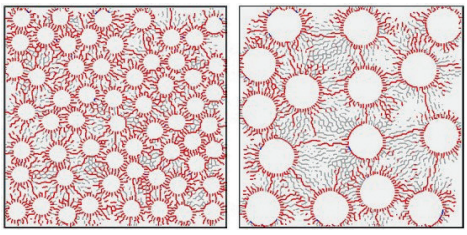

Figure 2.9 Modelling of shrinkage-induced microcracking in samples with 4 mm (left) and 8 mm (right) aggregate at equal volume fraction at a cement paste shrinkage of 0.5%, using a discrete lattice model (Grassl et al., 2010).

Results from lattice-based finite element modelling of shrinkage-induced microcracking are shown in figure 2.9. It was found that coarse aggregate particles resulted in wider cracks and hence an increase in transport phenomena of that concrete.

Koenders (1997) used the Delft-BLM to investigate the deformation of concrete specimens due to autogenous shrinkage of the cement paste. In a step-wise calculation procedure the cement paste beams of the lattice model were loaded by an internal strain, representing autogenous shrinkage of the cement paste. The imposed deformations of the hardening cement paste are (partially) restrained by the aggregate. The result of this is a smaller volume change in the concrete compared to the unrestrained volume change in the neat cement paste (see Fig. 2.10). In Koenders' calculations linear elastic behaviour of the material was assumed. Microcracking and stress relaxation in the cement paste were not considered. Note that the lower shrinkage of concrete compared to the cement paste is not obtained for free, but at the cost of tensile eigenstresses in the cement paste.

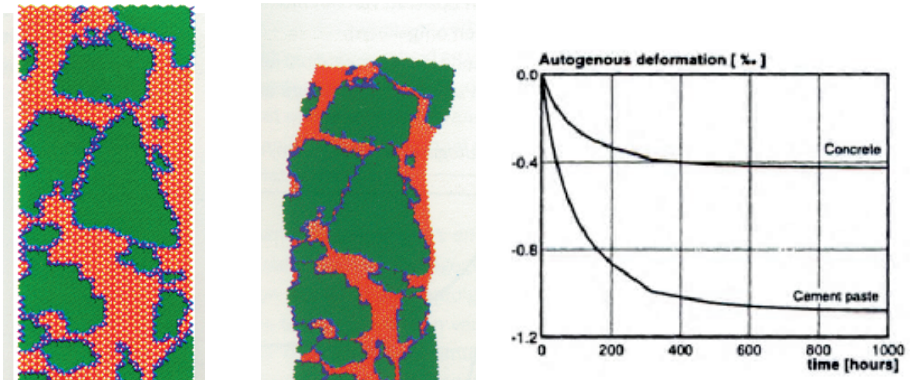

t_0 = 0 hour t_0 = 100 hour

Figure 2.10 Numerical simulations of autogenous shrinkage deformation of a concrete sample (40 x 80 mm) after 0 hour (left) and 100 hours hydration (right) and the autogenous deformation as function of time (after Koenders et al., 1998).

In a later study Schlangen et al., (2004) used the Delft-BLM for investigating the cracking process generated by autogenous shrinkage of the cement paste.

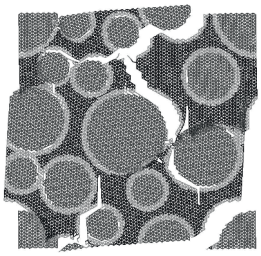

Figure 2.11 Cracking due to autogenous shrinkage in full restrained (periodic boundaries) 2D lattice specimen 600 μm x 600 μm (beam length 8 μm) with aggregates ($40 \leq d \leq 200$ μm) and $w/c = 0.3$ (Schlangen et al., 2004).

His numerical model contained circular aggregates (E_a = 70 GPa) with diameters between 40 and 200 μm randomly placed in the cement paste. The length of the BLM beams was 8 μm. The cement paste stiffness ranged from about 5 to 10 GPa. Relaxation was taken into account by assuming that 50% of the stress in the matrix and ITZ beams relaxes immediately. Figure 2.11 shows an example of the calculated crack pattern in the sample. Microcracking concentrates to a great extent in the aggregate – cement paste interface.

In the Delft-BLM the natural heterogeneity of concrete is simulated by random placement of aggregate particles and variation of the mechanical properties of the beams representing the different phases of the concrete, i.e. cement paste beams, aggregate beams and bond beams representing the ITZ. The heterogeneity of the concrete will promote the occurrence of irregular crack patterns. If the aim of numerical analyses is to simulate realistic crack pattens, more sophisticated lattice meshes will be adopted. An brief overview of possible mesh patterns, presented in figure 2.12, has been discussed by Lilliu (2007). Figure 2.12a shows a regular lattice mesh, whereas the figure 2.12b,c,d show lattices meshes with increasind degree of randomness. A high degree of randomness can be preferreable if the aim of the analysis is to mimic the crack pattern as realistic as possible. In this study the focus is on the effect of stress relaxation on eigenstresses and microcracking for which a regular lattice is appropriate.

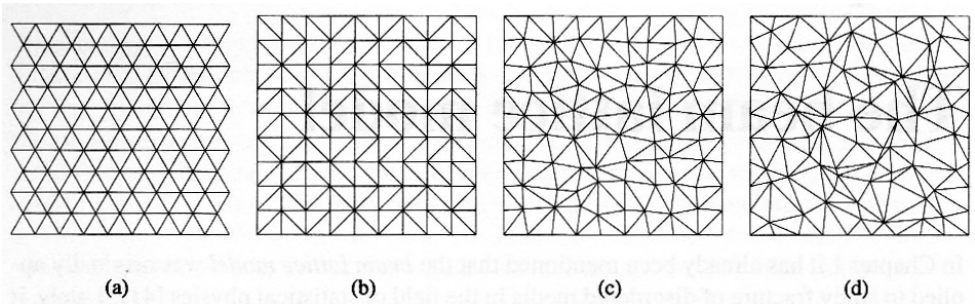

Figure 2.12 Examples of 2D regular and random lattices. a) regular lattice; b,c,d) lattices with increasing randomness (after Lilliu, 2007).

2.5.3 Effect of time dependent material properties on fracture processes

Little information is available about the effect on time dependent material behaviour on the formation of microcracking caused by eigenstresses. From numerical analysis of microcrack formation Idiart et al., (2011) concluded that assuming time *independent* material behaviour resulted in a much higher degree of microcracking. Relaxation would reduce stresses and promote redistribution of stresses. Lopez et al., (2001) studied basic creep under sustained compressive loads at various stress levels and the occurrence of microcracking. Some microcracks, which did not develop under the application of a short term load, did occur over time while the external load remained constant. Further evolution of cracking was accompanied by internal redistribution of stresses. These stresses were progressively transferred from the matrix to the larger aggregate particles.

2.6 Experimental determination of microcracks

Several methods have been used to study the evolution of microcracking of concrete. Commonly used is the *acoustic emission* (AE) technique by which the AE hits increase with the number of microcracks (Landis et al., 1995, Li et al., 2000). Other methods used to determinate microcracking are the *ultrasonic pulse velocity* (UPV) test (ASTM C597, 1997), by which the reduction of the pulse velocity is a measure for the intensity of microcracking (Wang et al., 2016) and the *impregnation techniques,* by which specimens are impregnated with dye or epoxy to facilitate detection and identification of microcracks (Bisschop et al. 1999, Hsu et al., 1963). For detecting microcracking in cement paste specimens the Environmental Scanning Electron Microscopy (ESEM) technique is commonly used. The advantage of this technique is a high resolution, needed to detect the microcracks, and the possibility to use not pre-dried specimens. Bisschop (2002) used the ESEM to study microcracking due to drying shrinkage in concrete specimens.

2.7 Evaluation

Eigenstresses are always present in concrete. Direct measuring of this kind of stresses is not possible and their magnitude is often not known and even not considered in the prediction of the performance of concrete structures. This implies that actual (tensile) stresses can be different from the calculated (tensile) stresses. A higher tensile stress level implies a higher susceptibility to microcracking, which may result in a lower durability than assumed. Jun et al., (2010) stated that uncontrolled residual stresses are detrimental to the performance of a product and he considered residual stress as one of the mechanisms through which processing significantly affects the quality, durability and mechanical response of engineered components.

The origin of eigenstresses in concrete are temperature and shrinkage-induced deformations. In this respect a subdivision is made between the occurrence of eigenstresses due to a non-uniform strain field in a cross-section of a structural element, noted in this study as *structural eigenstress.* The eigenstresses caused by the restraining effects of aggregate particles are noted in this study as *material eigenstress.*

Depending on the imposed strain gradients, caused by cooling and/or drying, micro- and/or macrocracks will occur in the surface zone of concrete structures. The imposed tensile strains can reach about two or three times the tensile strain capacity of concrete ($0.1 \cdot 10^{-3}$ m/m). This means that the occurrence of microcracking is almost unavoidable.

In a deterministic approach cracking is assumed to occur when *tensile strain criteria* or *tensile strength criteria* are exceeded. With respect to temperature-induced tensile strains the *temperature differential criterion* is used, which is in fact equivalent with the *tensile strain criterion*.

Tensile *material eigenstresses* reach maximum values at the surface of aggregate particles where microcracking starts. This microcracking process is often dominated by the weaker 'interfacial transition zone' (ITZ) of the cement paste. Results of studies (Grassl et al., 2010, Idiart et al., 2011, Fabien et al., 2012) showed the influence of aggregate size and aggregate

volume fraction on shrinkage-induced microcracking and the influence of microcracking on the concrete strength.

With increasing magnitude of the eigenstresses initially isolated microcracks may become connected, forming macrocracks that facilitate the penetration of water and/or aggressive substances into the concrete and enhance the risk of corrosion of reinforcing steel. In the engineering practice *macrocrack width criteria* are used to determinate the allowable crack width. In contrast to the macrocrack criteria no *microcrack criteria* exists, but the presence of microcracks certainly affects the transport properties of concrete (Hearn 1999, Mu et al., 2013).

In this study only microcracking caused by imposed deformation are analysed. It is noticed, however, that microcracks are also initiated by (external) loads on the concrete (Zhao 2006). This means that concrete structures subjected to loads are less durable than those without loads. Niu et al., (2008) concluded in this respect that durability research findings obtained from experiments on non-loaded specimens cannot reflect the real durability performance of the concrete.

Tegguer et al., (2013) showed that the chloride diffusion coefficient substancially increases in specimens when microcracking is generated using a uniaxial compression test. This phenomenon was recently also reported by Wang et al., (2016).

Lattice models seem appropriate tools for mimicing concrete on mesoscale as a three-phase material with beams representing the cement paste, ITZ and aggregate (Schlangen (1993). Schlangen et al., (2004) used the Delft-BLM for investigating the microcracking in the cement paste due to autogenous shrinkage in a linear elastic approach. In this study relaxation was taken into account by assuming that a fraction of the stresses (50%) in the matrix and ITZ beams relaxes immediately. The challenge of the present study is to analyse the effect of relaxation of stresses generated by imposed deformations in more detail.

For studying fracture processes in concrete it is essential that time dependent material behaviour (stress relaxation) is taken into account. Idiart et al., (2011) concluded in this respect that time independent material behaviour results in a much higher degree of microcracking.

Chapter 3

3. Numerical procedure for analysing eigenstress

In this chapter an extended Beam Lattice Model is presented suitable for calculating residual eigenstresses in concrete and cement paste caused by shrinkage, taking into account the influence of stress relaxation. In the chapter the focus is on the numerical tool for performing the analysis. Details of the time dependent properties of concrete, i.c. cement paste, will be dealt with in chapter 4.

3.1 Concrete as a multi-scale material

To gain information about stresses and microcracking with enough detail in a numerical analysis of concrete, the analyses must be carried out at an appropriate length scale. For concrete a subdivision can be made at three subsequent length scales. These length scales have been chosen in view of the typical dimensions of the constituents of the concrete. These components are the cement paste or matrix, the aggregate particles and the matrix-aggregate interfacial zone (ITZ). The hierarchical length scales have been proposed by Wittmann (1982). He distinguished the following length scales:

1 Macro-level
On the macro-level concrete is considered to be a homogeneous material. All internal heterogeneities and structural defects are considered to be smeared out over the total volume.
Scale size: materials laws (10^{-2} m to 10^{-1} m).

2 Meso-level
On the meso-level concrete is considered as a three-phase (3P) material. The meso-scopic heterogeneity is characterized by:
- aggregates: most (dense) aggregates in concrete can be considered to react in a linear elastic way and to undergo negligible shrinkage;
- cement paste matrix: a porous material with a wide range of pore sizes;
- interfacial transition zone (ITZ): a thin paste layer at the aggregate surface with a generally lower (tensile) strength compared to the bulk cement paste matrix.

On the meso-level the internal restraint caused by the presence of aggregates in the mixture can be taken into account.
Scale size: matrix, aggregate, large cracks (10^{-4} m to 10^{-2} m).

3 Micro-level
On the micro-level the microstructure is built up of reaction products, cement particles and pores. On this level the internal restraint and associated stresses caused by the pres-

ence of un-hydrated cement particles and fillers in the cement paste matrix can be taken into account.
Scale size: hardened cement paste (10^{-8} m to 10^{-4} m).

In this study emphasis will be on analyses of shrinkage-induced deformations and stresses at the meso-level. Figure 3.1a shows a meso-level picture of concrete, together with an arbitrary 2D-schematization of the aggregate particles (Fig. 3.1b) and the 3-phase presentation of the concrete (Fig. 3.1c).

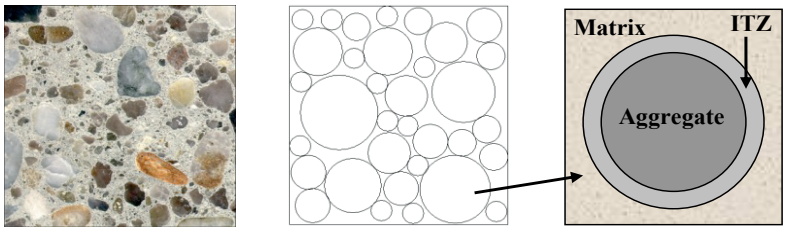

Figure 3.1 Two dimensional (2D) representation of the three-phase (3P) meso-scale model of concrete: aggregates surrounded by an ITZ and embedded in the cement paste matrix.

3.2 Numerical analysis of concrete at meso-scale

3.2.1 Beam Lattice Model – The concept

In chapter 2 several types of numerical models have been mentioned that could be used for numerical analyses of the response of concrete at meso-scale. In this study the analyses will be performed with a Beam Lattice Model (BLM). A typical example of the principle of a BLM is shown is figure 3.2. In lattice-type numerical models, a continuum is represented by a network of linear beam elements. The heterogeneity of the concrete is taken into account by assigning different properties to the lattice elements that represent the different phases

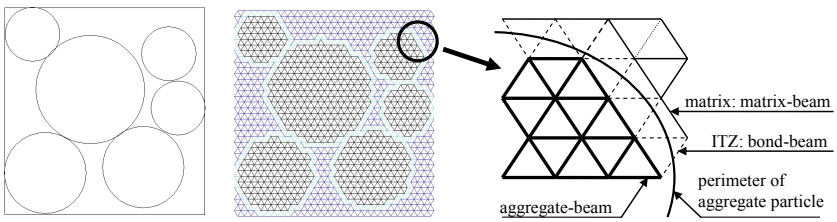

Figure 3.2 The identification of the three types of beam in the Delft-BLM: matrix-beams (m-beams), bond-beams (b-beams) and aggregate-beams (Schlangen 1993).

(Schlangen et al., 1992). An overlay-procedure is used to identify the three different types of beams to be considered in the analyses: aggregate-beams, matrix-beams and bond-beams, the latter representing the Interfacial Transition Zone (ITZ) (see Fig. 3.2).

In the lattice model, the meso-scopic brittle response is assumed to be caused by the (tensile) failure of individual cement paste beams, either matrix beams of bond beams (Fig. 3.3). The beams, representing the aggregate, are assumed to be linear elastic and do not fail. Of course, in case limited strength of aggregate particles has to be considered, the aggregate beams can fail as well.

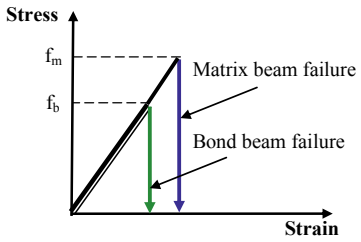

Figure 3.3 Tensile stress – strain relation of cement paste (matrix- and bond-beams) in the Delft-BLM. f_m = tensile strength matrix beams, f_b = tensile strength bond beams

3.2.2 Beam lattice geometry

As shown in chapter 2 there are several possibilities for the geometry of the lattice. The choice for the lattice geometry depends on the purpose of the analyses to be performed. In case the focus of the analyses is on details of the crack pattern, a choice of a more sophisticated lattice geometry is appropriate. In this study the focus is not on details of the crack pattern, but on analyses of the effect of relaxation on stresses induced by imposed deformations. A sophisticated geometry of the lattice has not priority in this case.
The basic geometry of the lattice to be used in this study is shown in figure 3.4. The nodes in the two-dimensional BLM are placed at equal distances in a triangular equilateral pattern. All the beams have the same length (l_{beam}) and are connected in the nodes (see Fig. 3.4).

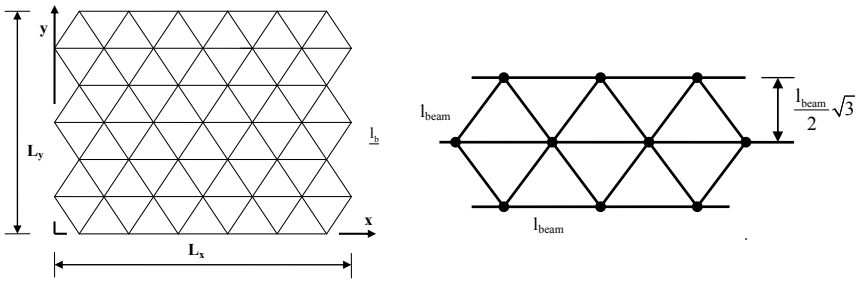

Figure 3.4 Geometry of the two-dimensional equilateral triangle beam lattice model (BLM) with beam length l_{beam}.

3.2.3 Beam size and lateral contraction (Poisson ratio)

When a continuum is represented by a lattice model due attention has to be given to a realistic simulation of the lateral contraction. With a two-dimensional equilateral triangle beam lattice model an apparent Poisson's ratio ν_{latt} [-] follows from the ratio of the height of the cross-section and the length of the beam lattice elements (Schlangen et al., 1997):

$$\nu_{latt} = \frac{1-\left(\frac{h}{l_{beam}}\right)^2}{3+\left(\frac{h}{l_{beam}}\right)^2} \quad (0 < h/l_{beam} \leq 1) \tag{3.1}$$

where h is the height of the lattice beams and l_{beam} is the length of the lattice beams. In this research a fixed beam length of 1.0 mm is used.

The value of the Poisson's ratio of the BLM is taken equal to the Poisson's ratio of hardened concrete, viz. $\nu_c = 0.20$. With $\nu_{latt} = 0.20$, the height of the beams follows from eq. 3.1, viz. $h = l_{beam} / \sqrt{3} = 0.577$ mm. The width of a beam is taken equal to its height, thus $b = h = 0.577$ mm. Note that the beam and the lattice structure as such are *fictitious*. Figure 3.5 shows how the lattice model is assumed to be constructed from non-slender beams ($l_{beam}/h = 1.73$). With the assumed size of the beams they would dramatically overlap, which is not realistic. In other words: the BLM is, as the term indicates, a model.

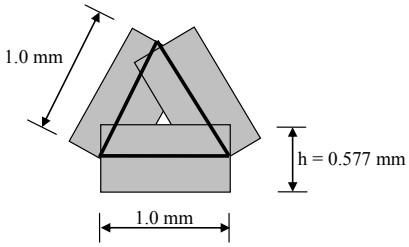

Figure 3.5 Lattice beams with length-height scale (1:0.58) in the triangular geometry of a 2D-BLM.

3.2.4 Aggregate size and aggregate volume fraction

In the two dimensional BLM the circular disk-shaped aggregate particles must at least contain several sets of triangles that can represent a rigid aggregate particle. Therefore, the minimum diameter of the aggregate particles d_{min} must be 3 times larger than the length of the beams in the BLM (Schlangen 1993), viz. $d_{min} = 3 \cdot l_{beam}$. As mentioned in the previous sectoin, in this research a fixed beam length is used of $l_{beam} = 1$ mm. The consequence of this choice is that the diameter of the smallest aggregate particle covered by the model is $d_{min} = 3$ mm.

Adopting a minimum aggregate size of 3 mm means that particles < 3 mm have to be disregarded and have to be removed from the mixture. Depending on the particle size distribution (PSD) of the aggregate disregarding of particles $d < d_{min}$ will lead to a substantial reduction of the aggregate volume (can be in the order of 35%). In the numerical simulations removal of the aggregate fractions smaller than d_{min} is compensated for by increasing the volume of the aggregate fractions equal or larger than d_{min}. If the aggregate volume fraction of particles < d_{min} is V_{agg,d_min}, the aggregate volume fraction $V_{agg,>d\_min}$ has to be multiplied by a factor γ, for which it holds:

$$\gamma = \frac{1}{1 - V_{agg,d_{min}}} \tag{3.2}$$

Practically speaking, the number of aggregate particles > d_{min} has to be multiplied with the correction factor γ in order to ensure that the intended aggregate volume is present in the concrete mixture.

The maximum particle size in this research is limited to 16 mm. Aggregate 'volume' fractions up to 75% with any particle size distribution will be considered.

3.2.5 Implications of ITZ

3.2.5.1 Representing the ITZ in BLM

In figure 3.1c it is shown that the ITZ is represented by bond. In ordinary concrete the thickness of the ITZ is in the order of 10-50 μm (Zheng et al., 2005). This thickness is much smaller than the length of a lattice beam, i.e. 1 mm. This is more than an order of magnitude smaller. In order to allow for the effect of the ITZ not the *thickness* of the ITZ, but the *volume fraction* of the ITZ-paste is taken into account in the numerical analyses. The total volume of the ITZ-paste depends on the specific surface and content of the aggregate in the concrete mixture. Garboczi et al. (1998) found that, depending on maximum aggregate size, the fraction of the ITZ in the bulk cement paste (V_{ITZ}/V_{bulk}) in concrete with an aggregate volume fraction of 0.75 m^3/m^3 and a proposed ITZ thickness of 30 μm is in the order of 0.67-0.79. For a concrete mixture with a coarse aggregate content, i.e. volume fraction, of 0.75 m^2/m^2, consisting of particles, as in this study, with a diameter in the range from 3 to 16 mm, the number of bond beams N_b, i.e. beams passing the ITZ, divided by the total number of paste beams, i.e. bond beams N_b plus matrix beams N_m, i.e. $N_b/(N_b+N_m)$, is 0.62. This ratio is in good agreement with the ITZ volume fraction of ordinary concretes (i.e. 0.67-0.79) mentioned by Garboczi et al. (1998). Based on this observation it is assumed that the effect of the ITZ volume fraction on the overall performance of a concrete mixture can be simulated with the bond beams of the 2D-BLM.

3.2.5.2 ITZ stiffness

According to Vervuurt (1997) the difference in stiffness of the ITZ and the bulk matrix has hardly any effect on the results of interface fracture. This finding was lateron confirmed by

Lilliu et al., (2003). Schlangen (1993) found that equal stiffness of bond-beams and matrix-beams in the beam lattice simulations (Delft-BLM) gave the best fit with results of uniaxial tensile tests on concrete. Therefore, in this study the stiffness of ITZ (E_b) and matrix (E_m) will be considered equal, i.e. $E_b = E_m$.

3.2.5.3 ITZ strength

The ITZ is the weakest link in normal strength concrete. Maso (1996) found that the tensile strength can vary from a small value up to the magnitude of the tensile strength of the bulk cement paste. In the lattice model a constant ratio between the tensile strength of the ITZ (f_b) and matrix (f_m) is assumed. An often used value is $f_b = 0.25\ f_m$ (Schlangen 1993). Vervuurt (1997) concluded that the strength of the ITZ-beams for a granite or phosphorous slag aggregate has to be chosen as less than half the matrix strength: $f_b < 0.5\ f_m$. In this study three values of the f_b/f_m ratio will be considered: $f_b/f_m = 0.25$, 0.50 and 0.75.

3.3 Numerical analysis of imposed deformation with BLM

3.3.1 General computation procedure for imposed deformation

For accurate analysis of eigenstresses and microcracking due to imposed deformations the effect of the time-dependent behaviour of the materials should be considered explicitly. This means an extra complication for the numerical analysis. A schematic representation of the calculation procedure is given in Figure 3.6. In the calculations first strain increments are assigned to all the matrix- and bond-beams at successive time increments and corresponding

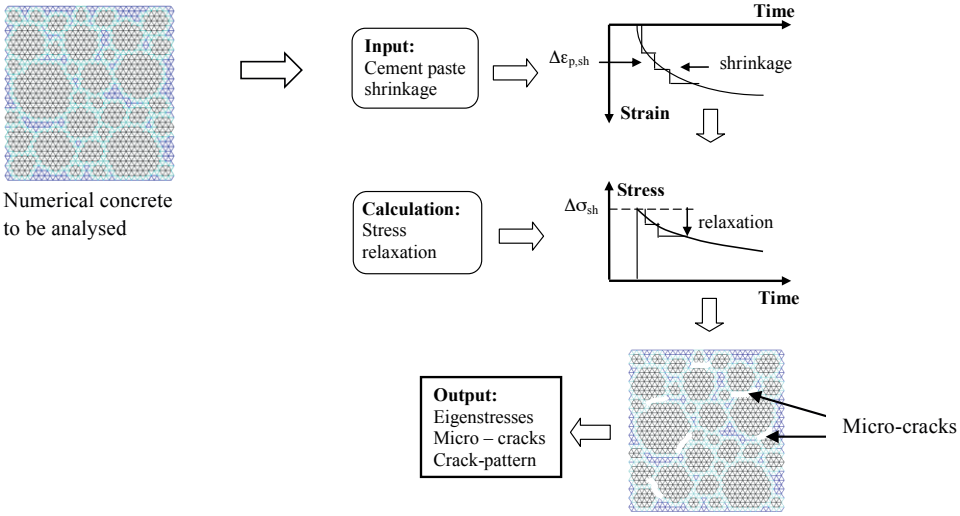

Figure 3.6 Schematic representation of calculation procedure: cement paste beams are 'loaded' with a shrinkage strain increment. Output: eigenstresses in m- and b-beams, number of broken m- and b-beams (microcracks) and the crack pattern.

elastic stresses are determined. Than the effect of relaxation on the stresses is determined and the residual eigenstresses and microcracking are calculated (see also section 3.3.2). The resulting stress in each cement paste beam (matrix and bond beams) of the lattice is calculated by superposition of what is left of all the previous stress increments.

Relaxation of the shrinkage-induced stresses is calculated with a relaxation formula based on the activation energy concept, which will be described in chapter 4.

3.3.2 Calculating stresses due to imposed shrinkage strain

In this section subsequent steps for calculating the stresses caused by imposed shrinkage and relaxation are presented in more detail. Figure 3.7 shows an arbitrary strain curve of a cement paste (dotted line), for which the generated stresses in a meso-structure have to be determined. The shrinkage strain increment in the matrix and bond beams is written as:

$$\Delta\varepsilon^{0}_{p,sh,i} = \varepsilon_{p,sh,i} - \varepsilon_{p,sh,i-1} \tag{3.3}$$

in which $\Delta\varepsilon^{0}_{p,sh,i}$ represents the imposed strain increment in a matrix or bond beam at time t_i and $\varepsilon_{p,sh,i}$ the cement paste shrinkage in a matrix or bond beam at time t_i.

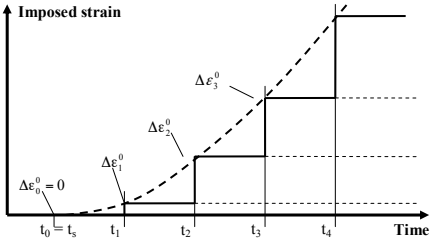

Figure 3.7 Imposed strain increments $\Delta\varepsilon^{0}_{i}$ (i.e. $\Delta\varepsilon^{0}_{p,sh,i}$) in the matrix-beams and bond-beams at each time t_i (schematic).

The response on the imposed strain is calculated with the displacement method. The imposed shrinkage strain in the matrix and bond beams is introduced with the forces F^{0}_{i} acting on both ends of the beams (see Fig. 3.8):

$$F^{0}_{i} = F^{0}_{i-1} + \Delta\varepsilon^{0}_{i} A_{beam} E_{p} \tag{3.4}$$

where F^{0}_{i} is the force needed to generate the imposed strain in a beam at time t_i, $\Delta\varepsilon^{0}_{i}$ is the imposed strain increment at time point t_i, A_{beam} is the cross-sectional area of a lattice beam and E_p is the modulus of elasticity of a matrix or bond beam.

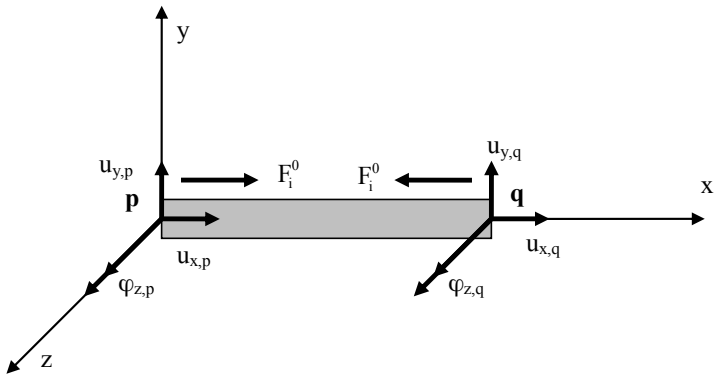

Figure 3.8 The imposed strain increment $\Delta\varepsilon^0_i$ is introduced by pairs of forces F^0_i on the ends of all the matrix- and bond-beams (further discussion in section 3.4.2).

3.3.3 Superposition of relaxed stresses

At any time t_i, the total stress $\sigma_{total,i}$ in each matrix and bond beam is the sum of the (elastic) stress increment $\Delta\sigma_{0,i}$ at the actual time t_i and what is left from all the previously inserted stress increments $\Delta\sigma_{0,j}$ from previous time steps t_j, i.e. $\Sigma\, \Delta\sigma_{0,j}.\psi_{i,j}$:

$$\sigma_{total,i} = \Delta\sigma_{0,i} + \sum_{j=1}^{j=i-1} \Delta\sigma_{0,j}\psi_{i,j} \tag{3.5}$$

in which $\sigma_{total,i}$ is the total stress at time t_i; $\psi_{i,j}$ the relaxation coefficient at time t_i for a stress increment that emerged at time t_j (i = time t_i ($1 \le i \le n$; j = time at loading t_j ($1 \le j \le i\text{-}1$) for $i \ge 2$). This superposition process, described with eq. 3.5, is schematically shown in figure 3.9.

The initial stress increment $\Delta\sigma_{0,i}$ caused by a strain increment $\Delta\varepsilon_i^0$ applied for $i \ge 1$, can be written with:

$$\Delta\sigma_{0,i} = -\left(\varepsilon_i^0 - \varepsilon_{i-1}^0\right)E_p \tag{3.6}$$

with ε_i^0 the imposed strain at time t_i ($1 \le i \le n$), E_p the modulus of elasticity of a matrix- or bond beam.

At each time t_i the residual (relaxed) stresses in all the matrix and bond beams are calculated. When the tensile stress in one of more beams reaches the tensile strength (f_m for matrix beams, f_b for bond beams), those beams get the status 'broken'. The stiffness in the broken beams is set on a low value ($E_{m,broken} = E_{b,broken} = 10$ N/m^2). The calculation at the same time t_i is repeated untill no further beams are broken and equilibrium at time t_i has been established.

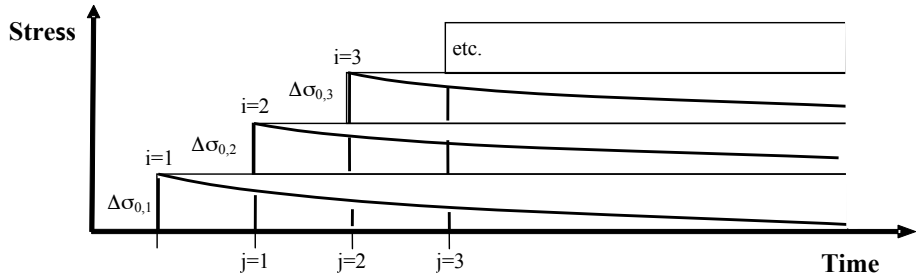

Figure 3.9 Schematic representation of the superposition of stress increments

The calculation is carried out with the displacement method by which the system of equations **Sv = k** is solved with the Efficient Cholesky Decomposition of the symmetric banded stiffness matrix **S** (see also section 3.4.2).

Fracture criterion

Fracture in the cement paste beams occur when the total tensile stress σ_{total} (section 3.3.3) exceeds the tensile strength. The fracture criterion which is frequently applied for the analysis of cracking in cement based materials with lattice models can be written as (Schlangen, 1993):

$$\sigma = \frac{F}{A_{beam}} + \alpha \frac{\left|M_p + M_q\right|_{max}}{W} \tag{3.7}$$

The formula represents the stress in the lattice beam due to normal forces (F) and bending moments (M_p, M_q) and $W = bh^2/6$. With the parameter α the effect of additional stress due to bending can be taken into account. With increasing α values the maximum tensile stress and the post peak are reduced. A common used value used in lattice analyses is 0.005. In this study the influence of bending is disregarded with $\alpha = 0$.

The fracture criterion used in this study implies that the cement paste beams are local brittle elements. The 2D beam lattice model with these elements has a brittle response. However, the initiation and growth of microcracks create a non-linear quasi-brittle material. In this respect the 2D lattice model has limitations for the analysis of microcracking in concrete. Physically realistic studies about crack formation and evolution in non-linear brittle materials, like concrete with pores and microcracks, require 3D lattices (Morrison, C.N. et al., 2014). The 2D lattice model used in this study has in this respect its limitations that can have influence on the results.

3.4 Overview of the calculation procedure

3.4.1 Building up of a 2D numerical concrete BLM-specimen

For a numerical 2D-analysis of the response of concrete to an imposed deformation first a lattice structure has to be built up that represents the concrete to be analysed.

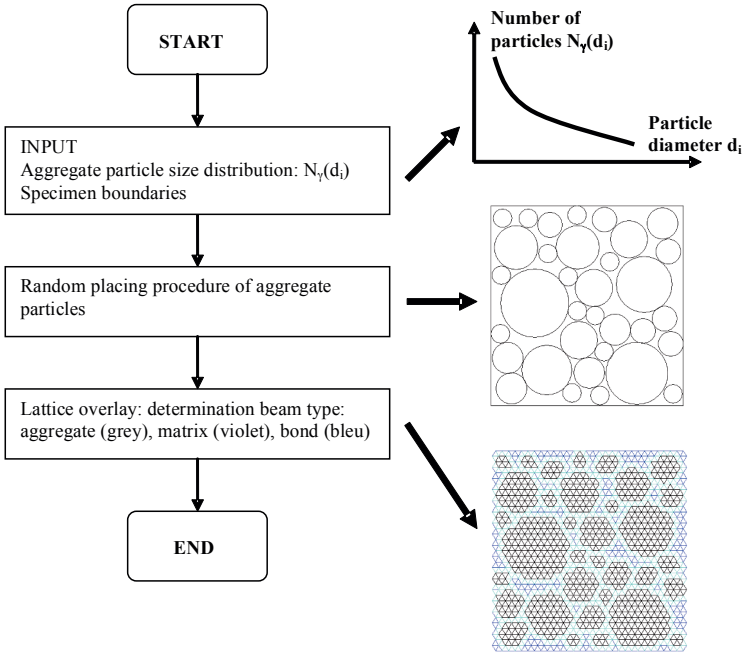

Figure 3.10 Building procedure of a beam lattice specimen

For a given (or arbitrary chosen) aggregate grading the aggregate particles are randomly placed in the BLM specimen. Aggregate particles are placed such that the prescribed aggregate content of the specimen is reached. As explained in section 3.2.4, in this study only particles in the range 3 mm ≤ d_i ≤ 16 mm are considered. Once all the aggregate particles are placed in the BLM-specimen, the lattice overlay procedure is started. The properties of the individual mixture components, i.e. aggregate particles, matrix and ITZ, are assigned to geometrically corresponding beams. The procedure is schematically shown in figure 3.10.

3.4.2 Eigenstress and microcrack analysis

For calculating the eigenstresses and microcracking in the BLM-specimen the finite element program WinFrame is used. The linear elastic beam elements have three degrees of freedom (u_x, u_y and φ_z) in each node (see also Fig. 3.8).

In the beam element between its two nodes p and q (Fig. 3.8) the beam element's end forces (normal force $F_{p,q}$, shear force $Q_{p,q}$ and bending moment $M_{p,q}$) and beam end displacements ($u_{x,p;q}$, $u_{y,p;q}$ and $\varphi_{z,p;q}$) are related with the element stiffness matrix, written as:

$$\begin{pmatrix} \frac{EA}{l} & 0 & 0 & -\frac{EA}{l} & 0 & 0 \\ 0 & \frac{12EI}{l^3} & -\frac{6EI}{l^2} & 0 & -\frac{12EI}{l^3} & -\frac{6EI}{l^2} \\ 0 & -\frac{6EI}{l^2} & \frac{4EI}{l} & 0 & \frac{6EI}{l^2} & \frac{2EI}{l} \\ -\frac{EA}{l} & 0 & 0 & \frac{EA}{l} & 0 & 0 \\ 0 & -\frac{12EI}{l^3} & \frac{6EI}{l^2} & 0 & \frac{12EI}{l^3} & \frac{6EI}{l^2} \\ 0 & -\frac{6EA}{l^2} & \frac{2EI}{l} & 0 & \frac{6EI}{l^2} & \frac{4EI}{l} \end{pmatrix} \begin{pmatrix} u_{x,p} \\ u_{y,p} \\ \varphi_{z,p} \\ u_{x,q} \\ u_{y,q} \\ \varphi_{z,q} \end{pmatrix} = \begin{pmatrix} F_p \\ Q_p \\ M_p \\ F_q \\ Q_q \\ M_q \end{pmatrix} \tag{3.8}$$

where A is the cross-section area of a lattice beam (A = h.b), I is the moment of inertia ($I = bh^3/12$) and l is the length of each lattice beam.

Written in matrix notation it holds (with the element stiffness matrix $\mathbf{S^e}$, the element displacement vector $\mathbf{v^e}$ and the element force vector $\mathbf{k^e}$):

$$\mathbf{S^e v^e = k^e} \tag{3.9}$$

By assembling all the element stiffness matrices with the transformation formula:

$$\mathbf{T^{eT} \hat{S}^e T^e v^e = k^e} \tag{3.10}$$

the system stiffness matrix is made:

$$\mathbf{Sv = k} \tag{3.11}$$

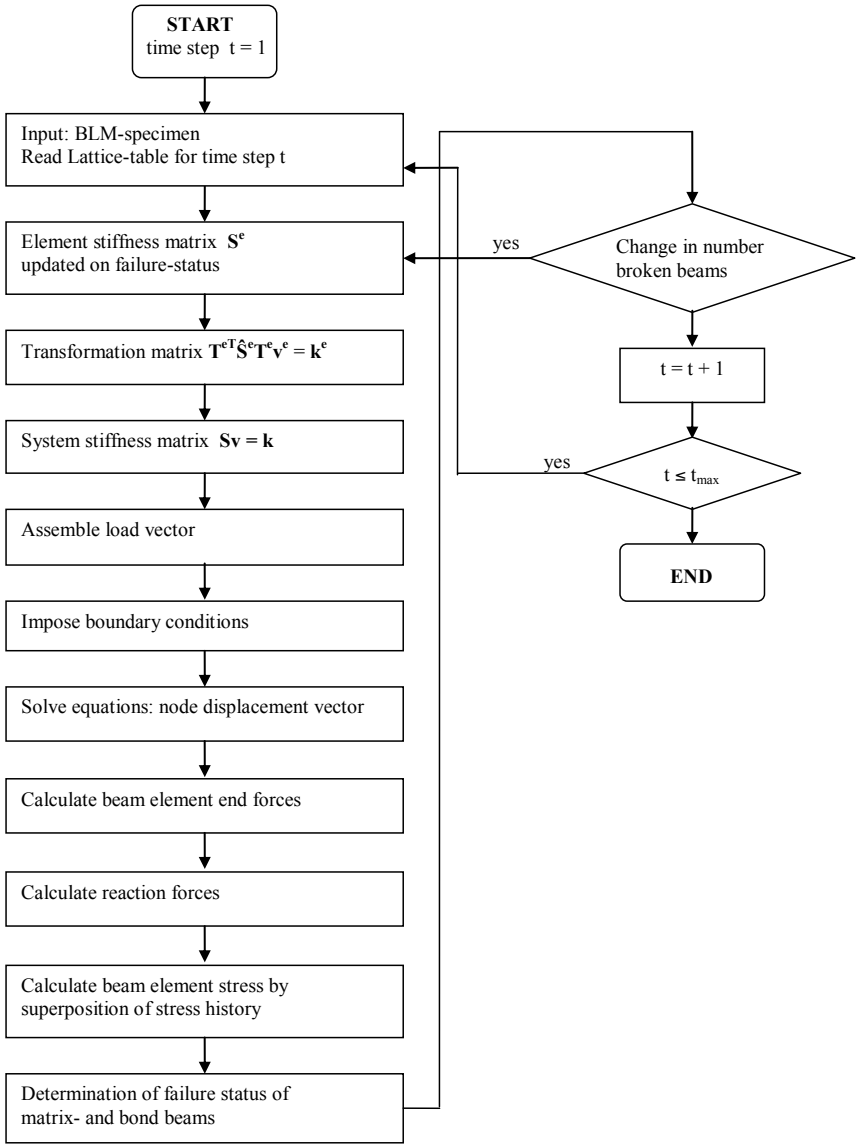

Figure 3.11 Flow chart for calculation of eigenstresses and microcracking in concrete exposed to imposed deformation, i.e. shrinkage of the cement paste, with a BLM.

The components of the force vector **k** are determined by calculating the primary node forces in each bond and matrix beam caused by the imposed shrinkage increments. The boundary conditions are implemented in the system stiffness displacement vector **v**. In the next stage the set of equations (eq. 3.10) is solved by using the symmetric band matrix method. The two displacements and rotation of all the nodes are stored. In the next stage the beam end forces are calculated from the node displacements. With the beam end forces the reaction forces on the lattice model are calculated. In the next stage the stresses in the beams are calculated, taking into account stress relaxation. When the calculated tensile stress in a bond or matrix beam exceeds the tensile strength, the beam is considered as 'broken'. The stress in beams with the status 'broken' is assumed to be zero.

When the number of broken beams in a certain time step is changed, the element stiffness matrices are adjusted for the reduced stiffness of the broken beams. The process as described before is repeated until the situation is reached in which no further beam failures take place. Stresses and displacements in the lattice beams are calculated in the next time step with the adjusted stiffness matrix where the broken beams are taken into account. A schematic representation of the calculation procedure is given as a flow chart (see Fig. 3.11).

3.5 Summary

In this chapter the main characteristics of the Beam Lattice Model used are presented. This BLM will be used for the numerical analysis of shrinkage-induced eigenstresses and microcracking in hardened concrete. The presented BLM has been built up in a similar way as the Delft Beam Lattice Model (Schlangen 1993). However, an option has been added that enables numerical analysis of the effect of relaxation on the generated shrinkage-induced stresses. The evolution of eigenstresses is calculated in an incremental computation process by superposition of residual stress increments.

The proposed BLM is able to analyse the effect of the aggregate content, aggregate grading aggregate stiffness, stiffness and strength of the matrix and strength of the ITZ on the response of a numerical concrete specimen subjected to imposed shrinkage of the cement paste. For quantification of the effect of relaxation on the evolution of stresses an appropriate relaxation formula should be adopted. This will be discussed in chapter 4. Numerical analyses of stresses and microcracking in concrete specimens will be performed in chapter 5.

Chapter 4

4. Relaxation of cement-based materials

Eigenstresses in concrete partly fade away over time due to stress relaxation. Existing engineering approaches for calculating stress relaxation in concrete structures do not apply for detailed analysis of long-term effects on (eigen)stresses in the concrete and in the cement paste matrix in particular. In this thesis the activation energy concept will be used for analysing the effects of stress relaxation on residual eigenstresses in cement paste.

4.1 Introduction

In chapter 3 a Beam Lattice Model (BLM) for the analysis of the material eigenstresses and microcracking in concrete has been discussed. So far BLMs have been widely used for linear elastic analysis of stresses and strains of concrete at the mesoscale. For a more precise determination of residual eigenstresses the stress relaxation in the cement paste has to be considered as well.

Existing methods for the determination of stress relaxation in concrete structures are applicable for the calculation of time dependent effects on the macroscale, but are not appropriate for analysing eigenstresses at the level of the cement paste matrix (mesoscale). For the analysis of the effect of relaxation on eigenstresses in the cement paste matrix at the mesoscale the activation energy approach will be used. This approach will be described briefly in section 4.2.2

4.2 Stress relaxation in cement paste

4.2.1 The principle

For calculating the effect of relaxation on stresses in concrete caused by gradually developing imposed deformations, like shrinkage, an incremental stress analysis method can be used. The magnitude of stress relaxation is expressed by a relaxation coefficient ψ, being the ratio of the stress increment $\Delta\sigma(t,t_0)$ at time t and the initial stress $\Delta\sigma(t_0)$ caused by the imposed strain increment $\Delta\varepsilon(t_0)$ at the age of loading t_0. Hence:

$$\psi\left(t,t_0\right)=\frac{\Delta\sigma\left(t,t_0\right)}{\Delta\sigma\left(t_0\right)} \tag{4.1}$$

The effect of relaxation of an (eigen)stress due to an imposed strain increment is visualized in figure 4.1.

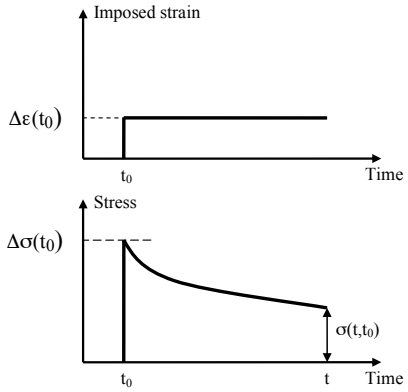

Figure 4.1 Schematic representation of the relaxation over time of an (eigen)stress due to an imposed strain increment $\Delta\varepsilon(t_0)$ at t_0.

In many codes the relaxation factor is a function of the creep coefficient φ. In Eurocode 2, part 1-1, this creep coefficient is a function of the relative humidity of the environment, the size and shape of the concrete element, the concrete compressive strength, the concrete age at loading and the duration of the load. This engineering approach is capable for the determination of *residual forces* and *force distributions* in concrete structures or structural elements on *macro-level*.

The goal of this study is to analyze and quantify the influence of stress relaxation on the evolution and magnitude of eigenstresses and microcracking at the *mesolevel*. For stress analysis at this level relaxation formulae given in design codes do not apply. For this reason the activation energy method will be used for the calculation of residual eigenstresses caused by imposed deformations.

4.2.2 Stress relaxation in cement paste – Activation energy method

4.2.2.1 Viscous flow in cement paste

It has been shown by Wittmann (1974) that creep deformation and stress relaxation of hardened cement paste can be calculated reliably with the activation energy approach. The basic concept was formulated by Eyring (1935) in his flow theory "Transition State Theory".

The mechanism of viscous flow due to a load consists of stepwise movements of molecules. This stress-activated mobility results on macro-level in a non-linear deformation of material in the direction of the stress, called creep deformation:

$$\varepsilon_{cr}(t,t_0) = \int_{t_0}^{t} \frac{d\varepsilon_{cr}}{dt}\,dt = \frac{d\varepsilon_{cr}}{dt}\left(t - t_0\right) \tag{4.2}$$

The creep strain rate can be written with the constitutive law (Krausz et al., 1975, Krausz et al., 1996):

$$\frac{d\varepsilon_{cr}}{dt} = \frac{d\varepsilon_0}{dt}\exp\left(-\frac{U}{RT}\right)\sinh\left(\frac{\sigma\Delta V}{RT}\right) \tag{4.3}$$

where $d\varepsilon_{cr}/dt$ is the creep strain rate [m/m.h], $d\varepsilon_0/dt$ the initial strain rate [m/m.h] at the moment t_0 for the applied stress σ [N/m^2], U the activation energy [J/mol], ΔV the activation volume [m^3/mol], R the universal gas constant (8.3145 J/molK) and T the absolute temperature [K]. The magnitude of the activation energy U and the activation volume ΔV have to be determined experimentally.

4.2.2.2 Activation volume

The activation energy approach assumes that the creep deformation is caused by the movement of small parts of mass. From research on creep of hardened cement paste Klug et al., (1969) concluded that C-S-H gel particles may be considered as the creep units. At this scale, i.e. at the nanoscale, the C-S-H can be considered as being a set of 'elementary bricks'. A typical size of these elementary particles is in the order of a few nanometers up to tenth of nanometers (Sanahuja et al., 2007) (Fig. 4.2).

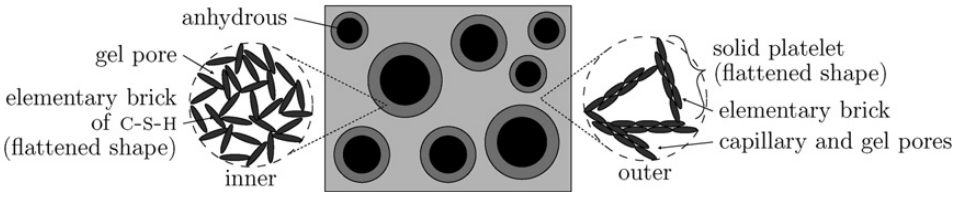

Figure 4.2 Schematic representation of the proposed morphological model of cement paste (Sanahuja et al., 2007).

Klug et al., (1974) used the results of relaxation tests on hardened cement paste to determine the activation volume. The tests were carried out on cement paste specimens, made with Portland cement PZ 375 with three different water-cement ratios loaded in compression (see Table 4.1). It was found that the value of the activation volume does not change over time and only depends on the composition of the cement paste (Wittmann 1974).

For the three cement paste mixtures the activation volume varies between $\Delta v = 1.5\cdot10^4$ Å^3 and $0.7\cdot10^4$ Å^3. In this study the time dependency of creep and relaxation will be calculated

Table 4.1 The (apparent) activation volume of hardened cement paste with different water-cement ratios (Klug et al., 1974).

Water-cement ratio	Activation volume	
ω_0 [g/g]	Δv [Å^3]	ΔV [m^3/mol]
0.3	$1.5\cdot10^4$	$9.0\cdot10^{-3}$
0.4	$0.8\cdot10^4$	$4.8\cdot10^{-3}$
0.5	$0.7\cdot10^4$	$4.2\cdot10^{-3}$

1 Å = 10^{-10} m, 1 Å^3 = 10^{-30} m^3; $\Delta V = \Delta v.\ N_A.10^{-30}$ m^3/mol ($N_A = 6.0221\cdot10^{23}$ 1/mol)

with an arbitrary value of the activation volume of $\Delta V = 7.0 \cdot 10^{-3}$ m^3/mol ($\Delta v = 1.16 \cdot 10^4$ Å^3), which volume corresponds to a cube with a rib length of 22.7 Å.

4.2.2.3 Activation energy

In the eighties Day et al., (1983) made an inventory of values of the activation energy U for creep. For a wide range of concretes, mortar and pastes U-values were found in the range from 25 to 116 kJ/mol. According to Day the activation energy for creep is low immediately after loading, but increases quickly to higher values, up to 100 kJ/mol. For cement pastes with a w/c = 0.65, Wittmann et al., (1968) calculated activation energies of 7.6 kJ/mol and 11.3 kJ/mol after 100 and 1000 hrs, respectively. For pastes with w/c = 0.4 an activation energy of 10.5 kJ/mol has been derived (Klug et al., 1969). In the latter publication activation energies at the beginning of a creep process in cement paste of 4.4, 5.6 and 6.6 kJ/mol after 25, 50 and 100 hrs under load, respectively, were reported. In a later publication Klug et al. (1974) found activation energies for cement paste of approximately 21 kJ/mol.

Klug et al., (1974) found that the water-cement ratio and moisture content had a significant effect on the magnitude of the activation energy of hardened cement paste. For a decrease of the relative humidity of cement paste from 90% to 40% an increase of the activation energy was found of about 2 kJ/mol. In concrete exposed to drying under atmospheric conditions such a decrease in relative humidity is conceivable, although quite large. Apart from microstructural changes in the cement paste, the drop of internal relative humidity partly explains the increase of the activation energy over time. In this study the evolution of the activation energy over time is taken into account with a log-function of time as proposed by Wittmann (1974):

$$U(t) = U_0 + \Delta U_0 \ln\left(1 + \frac{(t - t_0)}{t_1}\right) \tag{4.4}$$

where U_0 is the initial activation energy at the age of loading t_0 [J/mol], ΔU_0 a factor accounting for an increase of the activation energy over time [J/mol], t the actual age [h], t_0 the age at loading [h] and $t_1 = 1$ hr. For ΔU_0 a value of 300 J/mol holds.

It has to be mentioned that in the activation energy concept the rate of time dependent properties is determined by the values of both the activation volume and the activation energy. Care must be exercised, therefore, to adopt values of the activation volume and activation energy without knowing how these values have been determined. In this research not the exact values of creep and relaxation parameters are most important. Emphasis is on the sensitivity of eigenstresses for the effect of relaxation in concrete analysis. For these sensitivity analyses the activation energy values are arbitrarily set at $U_0 = 10$, 12 and 20 kJ/mol, whereas, as reported before, for ΔU_0 a value of 0.3 kJ/mol will be used. The evolution of the three adopted activation energies U(t) over time is shown in Figure 4.3.

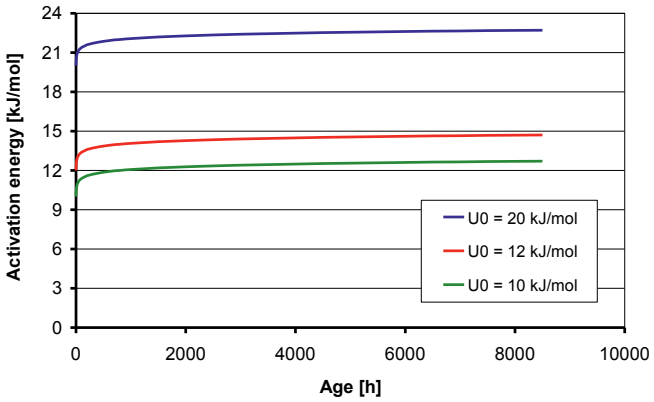

Figure 4.3 Evolution of the activation energy U(t) over time according to eq. (4.4). Values for U_0 are 10, 12 and 20 kJ/mol, while $\Delta U_0 = 0.3$ kJ/mol.

4.2.3 Relaxation formula for cement paste

4.2.3.1 Basic relaxation formula

When a material, like cement paste, is loaded the initially imposed elastic deformation gradually increases by a creep deformation:

$$\varepsilon_{total} = \varepsilon_{el} + \varepsilon_{cr} \tag{4.5}$$

The constraint for stress relaxation is that at any time the sum of elastic deformation and creep deformation is kept constant. This requirement can be written with the elastic strain rate ($d\varepsilon_{el}/dt$) and creep strain rate ($d\varepsilon_{cr}/dt$) as:

$$\frac{d\varepsilon_{total}}{dt} = \frac{d\varepsilon_{el}}{dt} + \frac{d\varepsilon_{cr}}{dt} = 0 \tag{4.6}$$

The creep strain rate is described with the activation energy concept (eq. 4.3) and the strain rate of the initial imposed deformation is written as:

$$\frac{d\varepsilon_{el}}{dt} = \frac{1}{E}\frac{d\sigma}{dt} \tag{4.7}$$

To fulfil the constraint for relaxation (eq. 4.6) relaxation of the initial imposed stress is required (see Fig. 4.4).

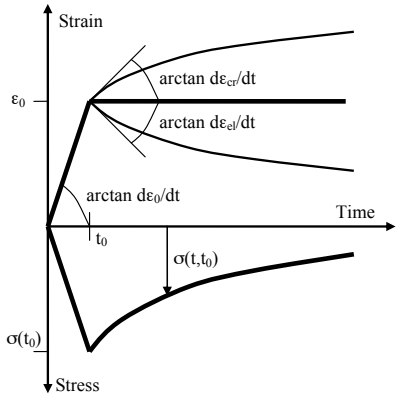

Figure 4.4 Stress relaxation due to a constant imposed strain ε_0, controlled by the strain rates $(d\varepsilon_{el}/dt) = -(d\varepsilon_{cr}/dt)$ (eq. 4.6).

By substitution of the elastic strain rate (eq. 4.7) and the creep strain rate (eq. 4.3) in equation 4.6, the coefficient for stress relaxation in cement paste can be written as (Appendix 4-1):

$$\psi(t,t_0) = \left(\frac{2RT}{\sigma_0 \Delta V}\right) \operatorname{arctan\,h}\left\{\tanh\left(\frac{\sigma_0 \Delta V}{2RT}\right)\exp\left[-2\left(\frac{\Delta V}{RT}\right)E_0\left(\frac{d\varepsilon_0}{dt}\right)(t-t_0)\exp\left(-\frac{U(t)}{RT}\right)\right]\right\} \quad (4.8)$$

where:
$\psi(t,t_0)$ = stress relaxation coefficient of cement paste [-]; $\psi(t,t_0) \leq 1.0$
σ_0 = stress at the time of loading t_0 [N/m^2]
$d\varepsilon_0/dt$ = imposed stress-dependent strain rate at the time of loading t_0 [m/mh]
E_0 = the modulus of elasticity of cement paste at the time of loading t_0 [N/m^2]
t = the actual age [h]
t_0 = the age at loading [h]
R = universal gas constant [J/mol.K]: R = 8.3145 J/molK
T = absolute temperature [K]
ΔV = apparent activation volume of cement paste [m^3/mol]
$U(t)$ = apparent activation energy of cement paste at time t [J/mol], see eq. 4.4

Parameters in eq. 4.8 which are taken into account with constant values are:

- activation volume : $\Delta V = 7.0 \cdot 10^{-3}$ m^3/mol
- increase of activation energy: $\Delta U_0 = 300$ J/mol
- temperature: T = 293 K (20°C)

With R = 8.3145 J/molK and T = 293 K it follows that RT = 2436 J/mol.

4.2.3.2 Structure of the relaxation formula – A simplified form

The relaxation formula given with eq. (4.8) contains many relevant parameters, but this at the cost of clarity.

In literature derivations are presented which lead to a more simpler structure of the relaxation formula. Simplification is possible for small stresses, leading to the condition that $\sigma\Delta V < RT$. For that condition the term $\tanh(\sigma\Delta V/2RT)$ can be approximated by $\sigma\Delta V/2RT$. Eq. (4.8) can then be rewritten as (see Appendix 4-1):

$$\psi(t,t_0) = \exp\left(-2\left(\frac{\Delta V}{RT}\right)E_0\left(\frac{d\varepsilon_0}{dt}\right)(t-t_0)\exp\left(\frac{\sigma_0\Delta V - U(t)}{RT}\right)\right) \tag{4.9}$$

For a given (constant) value of the activation volume ΔV the term $(\Delta V/RT)$ is a constant. With $\Delta V/RT = m$, eq. 4.9 can be rewritten as:

$$\psi(t,t_0) = \exp\left(-2\,m\,E_0\left(\frac{d\varepsilon_0}{dt}\right)(t-t_0)\exp\left(\sigma_0\,m - \frac{U(t)}{RT}\right)\right) \tag{4.10}$$

with $m^* = 2m / \exp(-U/RT)$ it holds:

$$\psi(t,t_0) = \exp\left(-m^*\,E_0\left(\frac{d\varepsilon_0}{dt}\right)(t-t_0)\exp(\sigma_0\,m)\right) \tag{4.11}$$

With $\dot{\varepsilon} = d\varepsilon/dt$, eq. 4.11 can be rewritten as:

$$\psi(t,t_0) = e^{-m^*.E_0\,.\,\dot{\varepsilon}\,(t-t_0)\,.\,e^{\sigma_0.m}} \tag{4.12}$$

which is a well-known structure for the relaxation factor $\psi(t,t_0)$.

For an arbitrary set of input data, listed in Appendix 4-1, figure 4.5 shows the evolution of the relaxation factor $\psi(t,t_0)$, calculated with relaxation formula (4.8) and the simplified formula (4.9). With the condition that $\sigma\Delta V < RT$, formula 4.9 can be used in incremental calculation procedures if small stress increments are considered. Figure 4.5 shows the evolution of

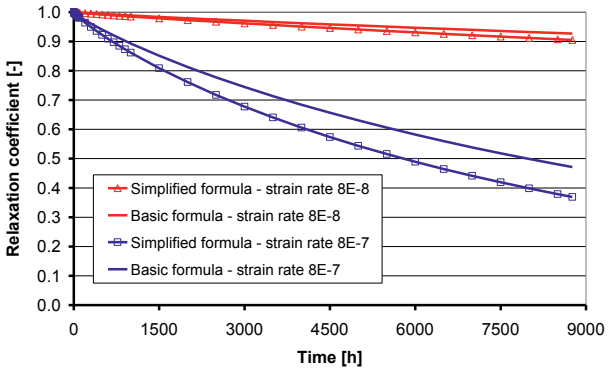

Figure 4.5 Evolution of the relaxation factor $\psi(t,t_0)$, calculated with basic relaxation formula 4.8 and the simplified formula 4.9. For details of the calculation, see Appendix 4-1.

the relaxation coefficient for $\sigma_0 = 0.1 \cdot 10^{-6}$ N/m^2. With this small stress, nesassary to meet the requirement $\sigma\Delta V < RT$, the decrease of the relaxation factor over time is limited with the formulas (4.8) and (4.9). From a comparison of the generated curves it can be inferred that for the chosen input data the curves do not deviate very much from each other. In this study, however, numerical analyses will be performed with the basic relaxation formula (4.8).

In the simplified formula it can easily be seen that stress relaxation is a function of the strain rate $\dot{\varepsilon}$, the initially generated stress σ_0 and the activation energy U (Note: the factor m* is a function of U). The effects of the strain rate and activation energy on the relaxation factor $\psi(t,t_0)$ are briefly discussed in the next section.

4.2.3.3 Effect of initial strain rate and activation energy on relaxation

This thesis focuses on the effect of relaxation on *shrinkage-induced* stresses. The rate at which these stresses are applied varies from relatively high values in the beginning of the shrinkage process to very low values at later ages. The shrinkage curve for which most of the stress analyses will be performed is presented in section 5.4, figure 5.6. From that shrinkage curve strain rates have been calculated at 1, 3, 7, 28, 91 and 365 days. The calculated strain rates are presented in Table 4.1. The strain rate decreases from about $1.0 \cdot 10^{-5}$ m/mh after 24 hours to about $4.5 \cdot 10^{-9}$ m/mh after 1 year. Figure 4.6 shows the evolution of the strain rate of the shrinkage curve during the first month.

Table 4.1 Shrinkage strain rates of the shrinkage curve presented in Figure 5.6.

Time		Strain rate
hour	day	[m/mh]
24	1	$1.0 \cdot 10^{-5}$
72	3	$4.0 \cdot 10^{-6}$
168	7	$1.3 \cdot 10^{-6}$
672	28	$1.7 \cdot 10^{-7}$
2184	91	$4.0 \cdot 10^{-8}$
8760	365	$4.5 \cdot 10^{-9}$

The effect of the strain rate on the evolution of the relaxation factor $\psi(t,t_0)$ is graphically shown in figure 4.7. The relaxation factors are calculated for activation energies U_0 = 10, 12 and 20 kJ/mol. The higher the strain rate, the faster stress relaxation develops.

Figure 4.7 shows that, depending on the parameters used in the equation, the relaxation factor calculated with eq. 4.8 can reach values close to zero. At time $t = \infty$ the relaxation factor always approaches zero, i.e. $\psi(\infty,t_0) = 0$, irrespective of the value of other parameters. This means that the validity of eq. (4.8) is limited since it is likely that a part of the initial stress remains at time $t = \infty$ under relaxation conditions. This limitation in proposed relaxation equations was already observed by Wittmann (1974). It is further noticed that the shrinkage strain rates are very low compared to the strain rates used in concrete strength tests. With the machines used for concrete compression strength testing (EN 12390 – part 4) the test deformation rate varies between 0.005 and 0.3 mm/min. For a concrete cube with rib size of 150 mm the strain rate varies therefore between $2 \cdot 10^{-3}$ m/mh and $120 \cdot 10^{-3}$ m/mh.

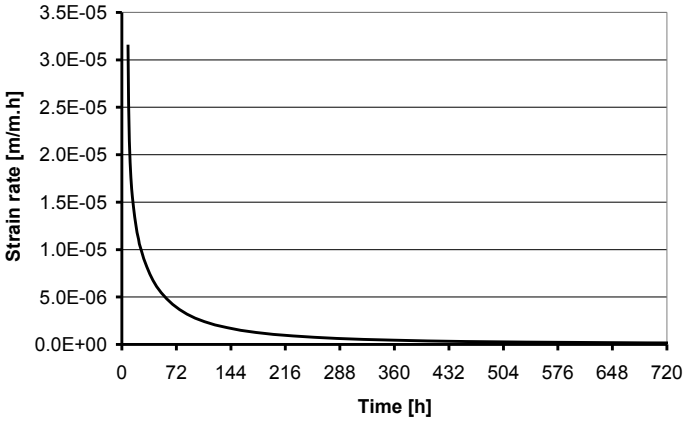

Figure 4.6 Evolution of the shrinkage stain rate in the shrinkage curve used in this study (chapter 5, section 5.4, Fig. 5.6) during the first month (30 days).

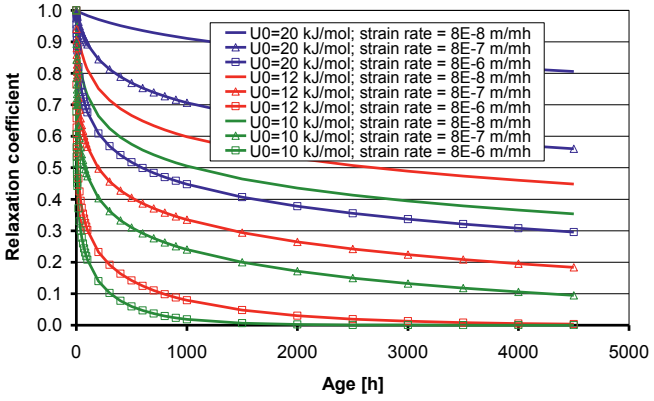

Figure 4.7 Relaxation factors for cement paste, calculated with eq. 4.8. Three strain rates are considered, i.e. $8 \cdot 10^{-5}$ m/mh (rapid), $8 \cdot 10^{-7}$ m/mh (moderate) and $8 \cdot 10^{-8}$ m/mh (slow). Stiffness: $E_0 = 7.8 \cdot 10^9$ N/m^2; stress: Initial stress: $\sigma_0 = 3.0 \cdot 10^6$ N/m^2.

4.3 Summary

Equations for calculating stress relaxation in concrete with creep coefficients presented in most of currently used codes, e.g. Eurocode 2, part 1-1, are not applicable for the analysis mesoscale of the eigenstresses and microcracking in the cement paste matrix at mesoscale. Therefore, in this study the activation energy method is adopted for numerical analyses of the effect of relaxation on the eigenstresses in concrete on the mesoscale.

In this chapter values for the activation volume and the activation energy have been briefly discussed. Based on this discussion values are adopted with which sensitivity studies will be performed. These sensitivity studies will be presented in chapter 5.

Chapter 5

5. Numerical analysis of eigenstresses and microcracking

This chapter presents the evolution and magnitude of eigenstresses and microcracking in concrete due to shrinkage of the cement paste. The two-dimensional beam lattice model (BLM), as described in chapter 3, is used to numerically simulate the response of specimens with specified compositions and material properties. The simulations are conducted without and with stress relaxation in the cement paste. Emphasis is on response in case of structural restraint. Situations of materials restraint are evaluated for comparison.

5.1 Introduction

The numerical analyses focus on the eigenstresses and microcracking caused by shrinkage of the cement paste in concrete under specific boundary conditions. A distinction is made between the eigenstresses in case of *structural restraint and material restraint.* The position of these specimens in the concrete structure and their boundary conditions for the numerical analyses are described in section 5.2.

The material properties of the BLM-specimens, such as cement paste shrinkage (section 5.3.1) and stiffness (section 5.3.2) are defined, including mix composition of the BLM-specimens (section 5.3.4).

The methods used to describe the evolution of the eigenstresses in the BLM-specimens are given in section 5.4. Section 5.5 contains the numerical test program and the results of the analyses. Detailed analysis of the evolution of stresses in individual beams, representing local stresses in the specimens, are discussed in section 5.7. Section 5.8 deals with the effect of the rate of imposed shrinkage on the response of concrete specimens. The effect of microcracking on the macroscopically observed shrinkage of concrete specimens is analysed in section 5.9. Section 5.10 contains a summary and discussion on all the generated numerical results. General preliminary conclusions are given in section 5.11.

5.2 Concrete specimens for numerical analyses of eigenstresses

5.2.1 Conditions to be simulated

For a numerical analysis of shrinkage-induced eigenstresses the surface layer of a concrete structure (e.g. slab, wall) is considered (see Fig. 5.1a). In this layer relatively high tensile stresses, caused by (partially) restrained imposed deformations, can occur. These eigenstresses may cause cracking. The evolution of these eigenstresses and microcracking is investigated with the BLM described in chapter 3 (see Fig. 5.1b).

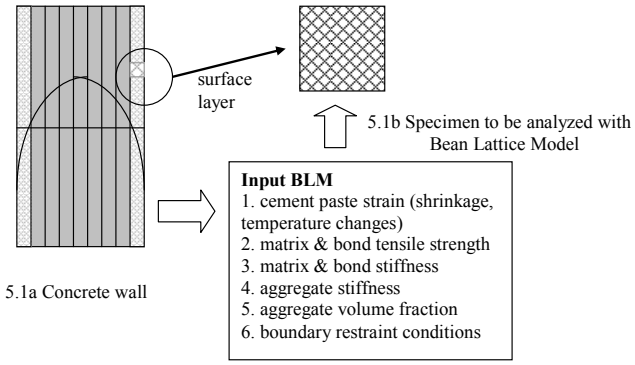

Figure 5.1 Concrete wall (5.1a) used to define the input parameters and boundary conditions for (5.1b) a detailed BLM analysis of the surface layer.

The input parameters required for the numerical stress analyses are the imposed strains caused by (see Fig. 5.1): (1) shrinkage of the cement paste; (2 and 3) the tensile strength and stiffness of the bulk cement paste and 'bond' paste in the interfacial transition zone (ITZ); (4) the aggregate stiffness and (5) aggregate volume fraction and (6) the restraint conditions. Values for these input parameters will be defined in section 5.3.2.

5.2.2 Boundary conditions

At the start of the simulation the concrete in the surface layer in the concrete wall (Fig. 5.1) is assumed to be free from micro- and macro-cracks. A small part, 48 mm × 50 mm, is considered in detail for the eigenstress analyses (Fig. 5.2). Two situations are considered:

a. situation without macro-cracks: *structural* eigenstresses, see figure 5.2a.
b. situation with macro-cracks: *material* eigenstresses, see figure 5.2b.

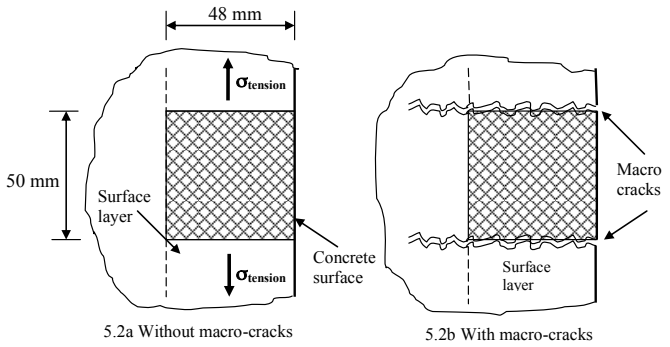

Figure 5.2 Surface layer of concrete wall. Fig.5.1a: without (macro)-cracks and Fig. 5.2.b: with two macro-cracks.

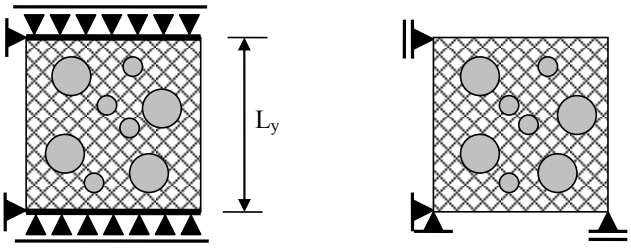

5.3a Structural eigenstress boundary condition

5.3b Material eigenstress boundary condition

Figure 5.3 Boundary conditions in the BLM for calculating structural eigenstress (a) and material eigenstress (b).

The boundary conditions in the BLM for *structural* eigenstress and *material* eigenstress are shown in figure 5.3.

For the simulation of *structural* eigenstresses (Fig. 5.3a), the specimen is clamped at the bottom and top edge, such that vertical displacements at top and bottom are zero (constant length L_y, $u_y = 0$). The nodes at the bottom and top edge are not fixed in horizontal direction, apart from two nodes where the horizontal displacements are fixed to ensure overall stability.

For the simulation of *material* eigenstresses (Fig. 5.3b), the specimen is free to deform in x- and y-direction, except at the three nodes where the horizontal and/or vertical displacements are restrained to have overall stability.

5.3 Mix composition and material properties

5.3.1 Mix composition of BLM-specimens

For the analyses of the response of the specimen to imposed shrinkage strains three different mix compositions are considered (Fig. 5.4):

1. Specimens with pure cement paste (paste specimens)
2. Specimens with one single aggregate particle ∅16 mm (single-particle specimens)
3. Specimens with more than one aggregate particle (multi-particle specimens) with:
   a. mono-size particles with particle size ∅3 mm, ∅4 mm and ∅8 mm.
   b. multi-size particles with particles ∅3 mm and ∅16 mm.
   c. continuous particle size distribution (PSD) (Fig. 5.5).

The number of particles in the (numerical) test specimens is chosen such that equal aggregate volume fractions (AVF) are obtained. Aggregate volume fractions in the 2D-test specimens (in fact: area fractions) range between 0.08 m^2/m^2 and 0.75 m^2/m^2. Specimens with a low AVF are those in which one single particle is present, or when only a few small particles are embedded in cement paste.

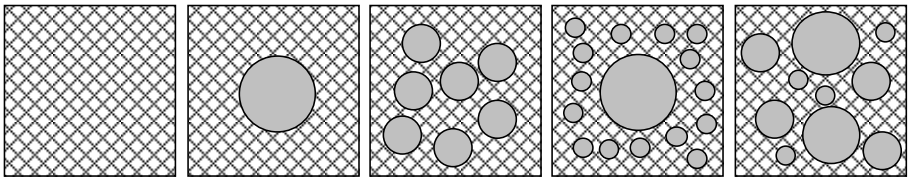

Figure 5.4 The different types of mix composition - schematic

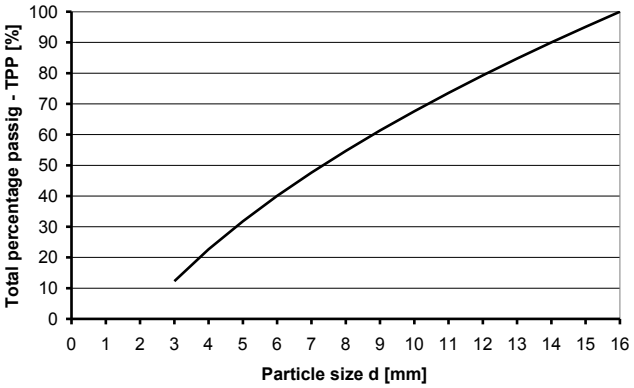

Figure 5.5 Continuous particle size distribution in specimens denoted CG (see Table 5.1)

Table 5.1 Mix composition of specimens for numerical analyses with BLM of eigenstresses and microcracking.

Specimen code	Aggregate Volume Fraction V_a [m^2/m^2]	Specimen composition
Matrix	---	Matrix without aggregate
C008-SP-16	0.08	Single particle 1∅16 mm
C008-MP-3	0.08	Multi particle 28∅3 mm
C060-MP-4	0.60	Multi particle 115∅4 mm
C060-MP-8	0.60	Multi particle 29∅8 mm
C060-MP-3/16	0.60	Multi particle 1∅16+176∅3 mm
C045-CG	0.45	Continuous grading ∅3-∅12 mm
C060-CG	0.60	Continuous grading ∅3-∅13 mm
C075-CG	0.75	Continuous grading ∅3-∅14 mm

.

In specimens with a continuous particle size distribution (Continuous Grading, CG) the Fuller grading is used with a minimum particle size of 3 mm (Fig. 5.5). Particles smaller than 3 mm are not considered in order to keep the mesh size and related computation time within acceptable limits. The small aggregate particles (d < 3 mm) are considered to be part of the matrix (For details on grading, see section 3.2.4).

An overview of mix compositions of specimens used for the numerical analysis with the BLM is presented in Table 5.1. The numerical test specimen are coded with the aggregate volume fraction, followed by the indicator SP (single particle size grading), MP (multi particle size grading) or CG (continuous grading), and the number and size of the aggregate particles.

5.3.2 Materials properties

5.3.2.1 Stiffness and tensile strength

As indicated in section 5.1, numerical analyses with the beam lattice model require input values for the following material parameters:

- tensile strength and stiffness of the bulk cement paste;
- tensile strength and stiffness of the 'bond' cement paste (Interfacial Transition Zone);
- stiffness of the aggregate particles;
- relaxation.

Although the specimens used for numerical analyses are made of 'virtual' mixtures, realistic values for the tensile strength and stiffness are preferred in order to enable drawing conclusions for the practice from the generated numerical results. The stiffness, or the modulus of elasticity of concrete, E_c is largely determined by the stiffness E_a and volume fraction V_a of the aggregate and the stiffness of the cement paste E_p. For given values of the aggregate content V_a, aggregate stiffness E_a and cement paste stiffness E_p Counto (1964) proposed the following relationship:

$$\frac{1}{E_c} = \frac{1-\sqrt{V_a}}{E_p} + \frac{\sqrt{V_a}}{E_a\sqrt{V_a} + E_p\left(1-\sqrt{V_a}\right)} \tag{5.1}$$

with V_a in [m^3/m^3] and E_c, E_a and E_p in N/mm^2. With eq. (5.1) the cement paste stiffness E_p can be calculated for chosen values of the concrete stiffness E_c, V_a and E_a. For arbitrary chosen values of the concrete stiffness E_c of 32000 and 44000 N/mm^2, aggregate stiffness E_a = 70000 N/mm^2 and aggregate volume fraction V_a of 0.75 and 0.60, values of the cement paste stiffness E_p are determined with eq. (5.1) and summarized in Table 5.2.

Table 5.2 Material properties to be used in numerical simulation with beam lattice model

Concrete stiffness E_c N/mm^2	Aggregated stiffness E_a N/mm^2	Aggregate volume fraction V_a m^3/m^3	Cement paste stiffness E_p (eq. 5.1) N/mm^2	Paste tensile strength f_p (eq. 5.2) N/mm^2
32000	70000	0.75	7800	5.0
44000	70000	0.60	15100	6.2
44000	70000	0.75	23200	7.1

The tensile strength of cement paste f_p is related to the cement paste stiffness E_p with an empirical equation based on experimental data presented by Padevat et al. (2014):

$$f_p = \frac{1}{4}\sqrt[3]{E_p} \tag{5.2}$$

with f_p and E_p in N/mm^2. Values of f_p are presented in the last column of Table 5.2. A paste tensile strength f_p = 5.0 N/mm^2 is a commonly used value in numerical analyses on the performance of concrete (Schlangen 1993).

5.3.2.2 Bond strength in paste-aggregate interface (ITZ)

In ordinary concrete the tensile strength of the matrix-aggregate interfacial transition zone, f_b, is generally lower than the tensile strength of the bulk matrix. Hsu et al. (1963) found a tensile strength of the bond paste varying from 50-75% of the tensile strength of the bulk paste. In this study the bond strength f_b is assumed to range from 25, 50 and 75% of the tensile strength of the bulk paste.

5.3.2.3 Relaxation

Relaxation of the eigenstresses in the cement paste matrix of the numerical specimens is calculated with eq. (4.8). In the analyses three values for the activation energy U_0 are used, i.e. U_0 = 10 kJ/mol, 12 kJ/mol and 20 kJ/mol, in combination with ΔU_0 = 0.3 kJ/mol.

5.4 Numerical analyses – Structure of the calculation process

5.4.1 Shrinkage curve of cement paste

The analyses of shrinkage-induced eigenstresses will be performed for a shrinkage curve of the cement paste presented in figure 5.6. This arbitrary chosen curve represents the free shrinkage of cement paste under drying conditions during a period of one year (Fig. 5.6a). The evolution of the shrinkage in the first 22 days is shown in figure 5.6b. An argument for this relatively high shrinkage value used in the analyses is that drying shrinkage in the cover concrete of structures can reach high values in a short period of time.

All the simulations presented in the sections 5.5, 5.6 and 5.7 will be carried out for the shrinkage curve of the cement paste shown in figure 5.6. In section 5.8 simulations will be performed for two other shrinkage curves as well in order to evaluation the effect of the rate of shrinkage on the resulting eigenstresses.

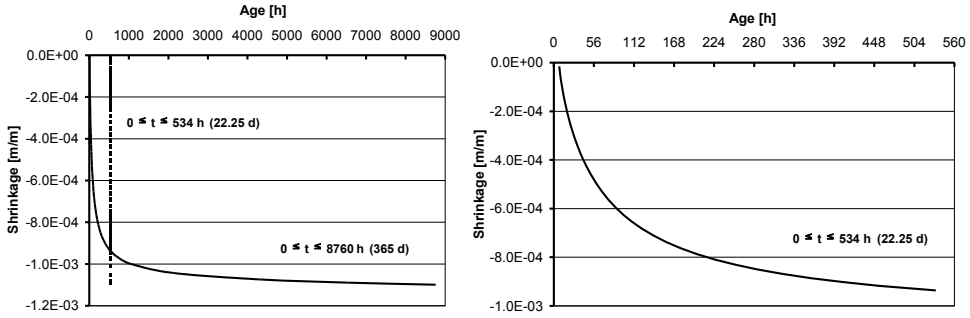

a. Shrinkage during 365 days b. Shrinkage during first 22.25 days

Figure 5.6 Cement paste shrinkage ($\varepsilon_{p,sh}$) used in the analyses: $0 \le \varepsilon_{p,sh} \le -1099 \cdot 10^{-6}$ m/m after 365 days (left) and in detail the evolution of the shrinkage in the first 22.25 days (right).

5.4.2 Structure of the numerical analyses with the Beam Lattice Model

The structure of the calculation process is schematically presented in figure 5.7. The shrinkage strain of the cement paste will be assigned to the cement paste of the numerical test specimen, i.e. to the beams of the beam lattice model. In a step-wise calculation process the stresses in the cement past will be determined. Calculations will be performed for both *structural restraint* and *material restraint*. The *structural* eigenstress at macro-level, $\sigma_{se,macro}$, is calculated by dividing the reaction force F, generated by the shrinkage of the cement paste, in the horizontal cross-sectional area of the BLM ($L_x \times b = 48 \times 0.577 = 27.7$ mm^2) with b is the width of the beam element and L_x is the length of the BLM in horizontal direction (see section 3.2 and Fig. 5.7). As soon as individual beams are broken, the stress-strain curve starts to deviate from linear.

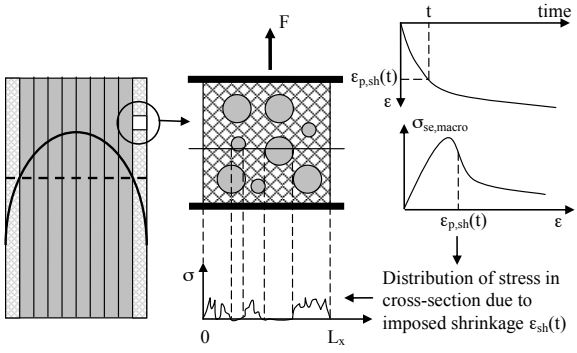

Figure 5.7 BLM-specimen with the *structural* eigenstress at macro-level ($\sigma_{se,macro}$) and the distribution of the *structural* eigenstresses in a cross-section.

After a certain peak load the stress $\sigma_{se,macro}$ decreases at a further increase of the imposed shrinkage strain $\varepsilon_{p,sh}(t)$ (see stress-strain curve in Fig. 5.7).

Because of the heterogeneous character of the specimen the stresses in the individual beams of the lattice model will be different. In section 5.6 the stress distribution in the cross-section of the numerical test specimens will be discussed in more detail.

5.4.3 The Microcrack Damage Ratio D_{mc}

When the tensile stress in a cement paste beam (matrix-beam, bond-beam) reaches the tensile strength (f_m in matrix beams, f_b in bond beams) the beam is assumed to fail and is denoted as being "cracked". The intensity of microcracking in the test specimen will be indicated with the microcrack damage ratio D_{mc}, indicating the percentage of broken beams relative to the total number of cement beams (both bulk matrix beams N_m and bond beams N_b):

$$D_{mc} = \frac{\text{number of broken cement paste beams}}{\text{total number of cement paste beams}} = \frac{N_{m,fail} + N_{b,fail}}{N_m + N_b} * 100 \ [\%] \qquad (5.3)$$

where N_m is the total number of matrix beams in the BLM, $N_{m,fail}$ the number of broken matrix beams, N_b the total number of bond beams in the BLM and $N_{m,fail}$ the number of broken bond beams.

5.4.4 Tensile strength f_{ct} of numerical concrete specimen

When the cement paste of numerical concrete specimens shrinks tensile stresses are generated and microcracking may occur, either in the paste-aggregate interfacial zone or in the paste itself. Due to microcracking the overall tensile strength of the concrete specimen will not reach the cement paste tensile strength. The peak tensile stress reached during the shrinkage process is denoted as the tensile strength f_{ct} of the concrete specimen.

5.4.5 Overview of performed numerical simulations

In the next sections of this chapter the results of numerical analyses on the performance of test specimens under imposed shrinkage of the cement paste are presented.

Table 5.3 Overview of numerical test program

Mixture parameters to be evaluated	Section
Cement paste stiffness E_p	5.5.1
Bond strength: Ratio of bond strength f_b and matrix tensile strength f_m	5.5.2
Aggregate stiffness E_a	5.5.3
Particle size (d) and particle size distribution (continuous grading)	5.5.4
Stress relaxation – low, moderate and high relaxation	5.5.5
Stress distribution over the cross section of the concrete	5.6
Material restraint vs. structural restraint	5.7
Effect of the rate of shrinkage on stress development	5.8
Role of cracking on shrinkage of concrete	5.9

The parameters of which the effect of relaxation and microcracking on the performance of the numerical test specimen will be analysed are summarized in Table 5.3.

5.5 Numerical analyses of eigenstresses - Results

5.5.1 Eigenstresses and microcracking: Influence of cement paste stiffness

The influence of the cement paste stiffness on the magnitude of eigenstresses and microcracking is analysed for three specimens, viz.:

- pure cement paste (matrix);
- single particle specimen with one aggregate particle 1∅16 mm (C008-SP-16);
- specimen with continuous aggregate grading with particles ∅3 - ∅13 mm (C060-CG).

Three cement paste stiffnesses are used, viz. E_p = 7.8, 15.1 and 23.2 GPa, respectively, with corresponding tensile strengths 5.0, 6.2 and 7.1 MPa (see Table 5.2).

The analyses are carried out with and without the effect of relaxation. Only moderate relaxation will be considered, i.e. with activation energy U_0 = 12 kJ/mol. The test program with the specimens and material parameters is listed in Table 5.4.

In this series only the magnitude of *structural eigenstresses* is analysed (full restraint). The development of the imposed shrinkage strain is presented in figure 5.6.

Table 5.4 Test program: Specimens and material parameters of specimens for numerical analyses

Specimen Code (Table 5.1)	Aggregate volume fraction V_a [m^2/m^2]	Material parameters				
		f_p [MPa]	f_b/f_m [-]	$E_m = E_b$ [GPa]	E_a [GPa]	Moderate relaxation U_0 [kJ/mol]
Matrix	0.0	5.0	---	7.8	---	---
	0.0	5.0	---	7.8	---	12
	0.0	6.2	---	15.1	---	---
	0.0	6.2	---	15.1	---	12
	0.0	7.1	---	23.2	---	---
	0.0	7.1	---	23.2	---	12
C008-SP-16	0.08	5.0	0.75	7.8	70	---
	0.08	5.0	0.75	7.8	70	12
	0.08	6.2	0.75	15.1	70	---
	0.08	6.2	0.75	15.1	70	12
	0.08	7.1	0.75	23.2	70	---
	0.08	7.1	0.75	23.2	70	12
C060-CG	0.60	5.0	0.75	7.8	70	---
	0.60	5.0	0.75	7.8	70	12
	0.60	6.2	0.75	15.1	70	---
	0.60	6.2	0.75	15.1	70	12
	0.60	7.1	0.75	23.2	70	---
	0.60	7.1	0.75	23.2	70	12

f_b/f_m = bond / matrix tensile strength ratio; cement paste stiffness: $E_p = E_m = E_b$

5.5.1.1 Structural eigenstress and micracking in cement paste (Specimen 'Matrix')

The effect of paste stiffness on structural eigenstresses in specimens made of pure cement and loaded by an imposed shrinkage is presented in figure 5.8. Stress-strain curves are presented for different paste stiffness and with and without relaxation.

When the tensile stress in the specimen reaches the matrix tensile strength f_m = 5.0, or 6.2 or 7.1 MPa the specimen shows a sudden failure. There is no residual bearing capacity.

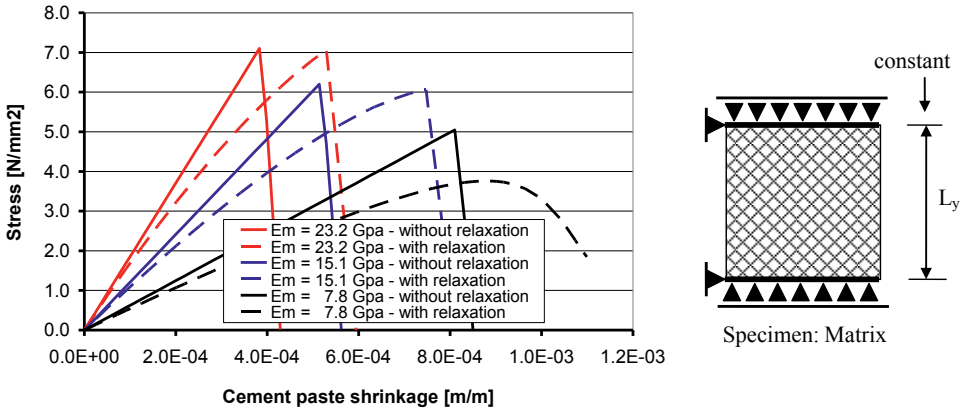

Figure 5.8 The *structural* eigenstress at macro-level, $\sigma_{se,macro}$, in a cement paste specimen for different stiffness of the cement paste. Stresses without relaxation and with moderate stress relaxation (U_0 = 12 kJ/mol).

At increasing cement paste stiffness the specimen stiffness increases and the maximum tensile stress is reached at a lower imposed shrinkage strain (see Fig. 5.8).

If moderate stress relaxation is taken into account the structural eigenstress at a specific shrinkage value is lower. Failure of the specimen is delayed, so higher shrinkage strains are reached before cracking occurs (if it occurs at all). Failure of the specimen cannot be prevented completely by relaxation, unless the cement paste stiffness is as low as 7.8 GPa.

In this simulation almost no effect of internal microcracking on the evolution of the post-peak stresses is observed. Because of the homogenous character of the cement paste all beams of the beam lattice model reach the tensile strength of the cement paste at the same time, resulting in brittle failure of the specimen.

5.5.1.2 Structural eigenstress and microcracking: single particle specimen (C008-SP-16)

The effect on the performance of adding one single particle ∅16 mm to the cement paste specimen under imposed shrinkage is shown in figure 5.9 for specimen C008-SP-16 for three different paste stiffness values. Results are shown for situations with and without relaxation.

Figure 5.9a shows that the stress-strain curve gradually bends shortly before the maximum tensile stress is reached, indicating that microcracking has started to occur. Microcracking in the pre-peak stage originates from bond beam failure (note: f_b/f_m = 0.75; Table 5.4). For strains beyond the strain at which the maximum tensile stress occurs, microcracking originates from failure of both matrix and bond beams.

The stage of sharp decreasing stress is accompanied by intensive microcracking. This is clear from figure 5.9b, where the damage ratio D_{mc} is shown as function of the imposed

strain. This figure also shows that with increasing stiffness of the cement paste the damage ratio D_{mc} reaches higher values. Stress relaxation results in a decrease of the damage ratio in the cases with E_m = 23.2 and 15.1 GPa. This in contrast to the case with E_m = 7.8 GPa, where the value of the damage ratio is higher in the case *with* stress relaxation compared to the case *without* stress relaxation.

In the post-peak stage the eigenstresses remain in the order of 1.0 – 2.0 N/mm^2 in the case with stress relaxation. When the maximum shrinkage strain of about $1.1 \cdot 10^{-3}$ m/m is reached the eigenstresses have decreased to values lower than 0.5 N/mm^2, irrespective whether relaxation is taken into account or not.

Figure 5.9c shows the crack patterns for different paste stiffnesses at the moment the imposed shrinkage strain has reached its final value of $1.1 \cdot 10^{-3}$ m/m for the case with moderate stress relaxation. Microcracking concentrates in the weakest cross-sections in the specimen at the top- and bottom-side of the aggregate particle. In the specimen with E_m = 23.2 GPa the microcracking at the top-side of the aggregate has formed a macro-crack. In the specimen with E_m = 15.1 GPa the microcracking at the top-side decreases while the microcracking at the bottom-side increases. Difference in microcracking at the top-side and the bottom-side is even more clearly visible in the crack pattern in the specimen with E_m = 7.8 GPa. The reason for an a-symmetry in the crack pattern is the excentric position of the aggregate particle in the specimen.

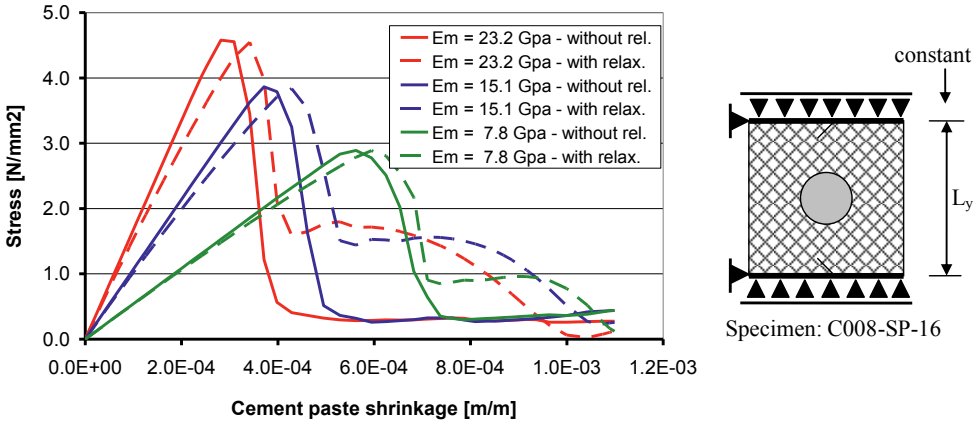

a. The *structural* eigenstress in specimen C008-SP-16

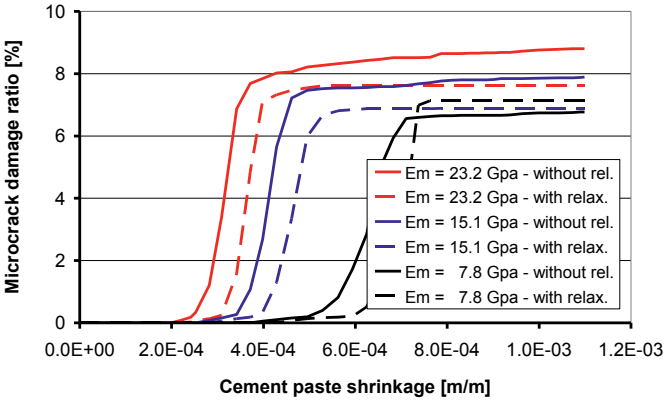

b. Microcrack damage ratio D_{cm}, specimen C008-SP-16

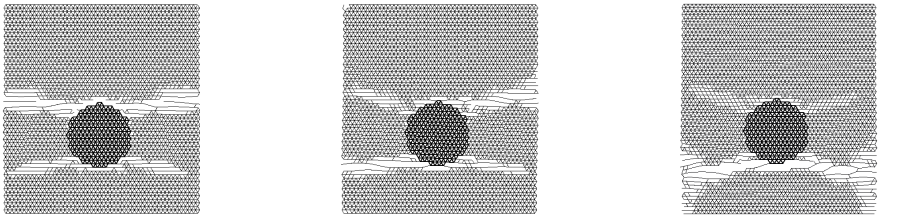

E_m = 23.2 GPa; D_{mc} = 7.6% E_m = 15.1 GPa; D_{mc} = 6.9% E_m = 7.8 GPa; D_{mc} = 7.8%

c. Crack pattern in specimen C008-SP-16 at maximum cement paste shrinkage $\varepsilon_{p,sh} = 1.1 \cdot 10^{-3}$ m/m. (situation with moderate relaxation).

Figure 5.9 The *structural* eigenstress at macro-level, $\sigma_{se,macro}$, (a), damage ratio D_{cm} (b) and crack patterns (c) in specimen C008-SP-16 (see Table 5.4) for different stiffness of the cement paste. Stresses without relaxation and with moderate stress relaxation (U_0 = 12 kJ/mol).

5.5.1.3 Structural eigenstress: specimen with continuous aggregate grading (C060-CG)

Structural eigenstresses in specimens with continuous aggregate grading caused by shrinkage of the cement paste are presented in figure 5.10 for three different paste stiffnesses. Calculations are performed with and without moderate relaxation. Figure 5.10 shows that moderate stress relaxation has only a small influence on the evolution of structural eigenstresses compared to the eigenstresses without relaxation. Obviously, the stresses are predominantly determined by the boundary conditions (full restraint of the specimen) and not so much by the restraining effect of the aggregate particles. In the post-peak stage the eigenstresses exhibit a similar tendency, irrespective of the effect of relaxation. The residual structural stresses decrease to a value of about 0.5 N/mm^2.

The maximum tensile eigenstress in the concrete specimen is denoted as the tensile strength f_{ct} (section 5.4.4). Figure. 5.10a shows that for different cement paste stiffness the tensile strength f_{ct} varies from about 2.5 MPa to 3.3 MPa for low and high paste stiffness, respectively. Hence, the tensile strength of the simulated concrete specimens, i.e. $\sigma_{se,macro}$, is about 50% of the tensile strength f_p of the cement paste (see Table 5.4).

Figure 5.10b shows the evolution of the damage ratio D_{mc} as function of the imposed shrinkage strains. In all the cases the evolution of the damage ratio shows a fast initial increase followed by a more gradually increasing value. In the cases without stress relaxation microcracking increases about linearly with increasing shrinkage strains. In case moderate relaxation is considered the increase of microcracking is slower with ongoing shrinkage strains compared to the situation without relaxation. Obviously relaxation reduces the intensity of microcracking substantially.

With a decreasing cement paste stiffness not only the magnitude of microcracking decreases. As shown in figure 5.10c, we also see that the microcracks tend to concentrate more in weak areas at the top- and bottom side of aggregates with the bigger diameters. The restraint of the specimen at the top and bottom in horizontal direction ($u_x = 0$, see Fig. 5.10a) results in a horizontal shear force in the specimen. Consequence of this is a concentration of microcracking at the vertical sides of the specimen not far from the bottom and top support of the specimen.

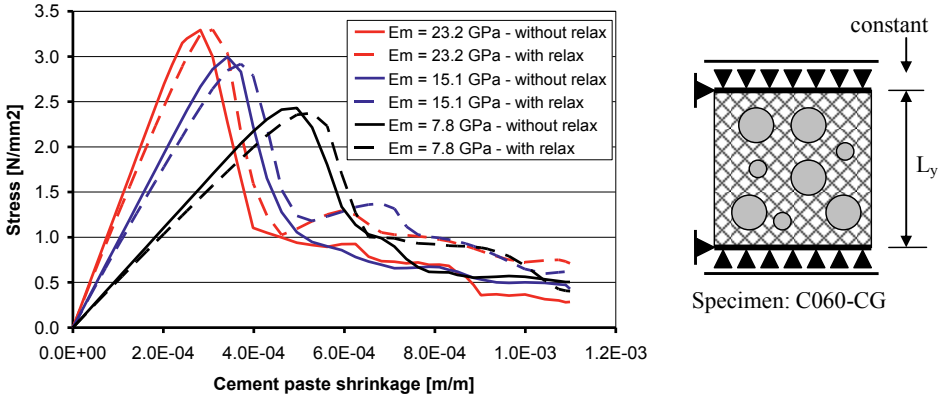

a. The *structural* eigenstress in specimen with continuous aggregate grading C060-CG

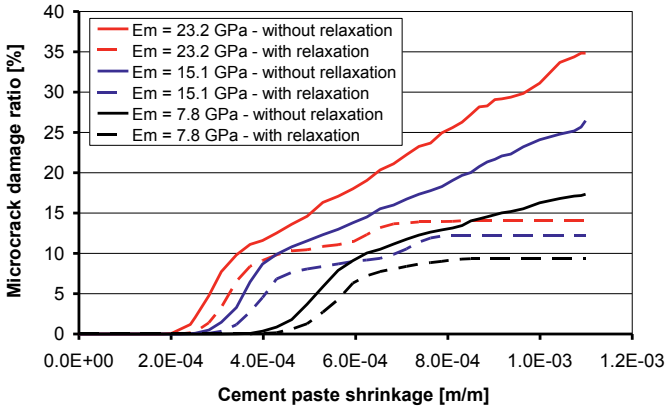

b. Microcrack damage ratio D_{mc}; specimen with continuous aggregate grading C060-CG

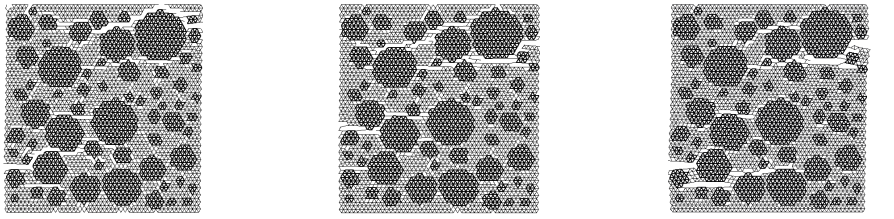

E_m = 23.2 GP; D_{mc} = 14.0 % E_m = 15.1; D_{mc} = 12.2% E_m = 7.8 GPa; D_{mc} = 9.3%

c. Crack pattern at maximum cement paste shrinkage $\varepsilon_{p,sh} = 1.1 \cdot 10^{-3}$ m/m. (situation with moderate relaxation).

Figure 5.10 The *structural* eigenstress at macro-level $\sigma_{se,macro}$ (a), damage ratio D_{mc} (b) and crack pattern (c) in specimen with continuous aggregate grading C060-CG for different stiffness of cement paste. Stresses without and with relaxation (U_0 =12 kJ/mol).

5.5.2 Structural eigenstresses and microcracking: Influence of bond strength

The influence of the bond strength between the cement paste matrix and aggregate particles on the magnitude of eigenstresses and microcracking is analysed for specimens with continuous aggregate grading and aggregate volume fractions of 45% and 75%, i.e. specimens C045-CG and C075-CG, with particle sizes between 3-12 mm and 3-14 mm, respectively.

All analyses are performed for a tensile strength of the cement paste f_p = 5 MPa. For the bond/matrix tensile strength ratio f_b/f_m values of 0.75, 0.50 and 0.25 are considered. The analyses are carried out both without and with (moderate) relaxation. In these simulations only structural eigenstresses will be evaluated. The test program with the specimens and material parameters is listed in Table 5.5.

Table 5.5 Test program: specimens and material parameters for the analysis of the bond / matrix tensile strength ratio

Specimen Code (Table 5.1)	Aggregate Volume Fraction V_a [m^2/m^2]	Material parameters				
		f_m [MPa]	f_b/f_m [-]	$E_m = E_b$ [GPa]	E_a [GPa]	Moderate relaxation U_0 [kJ/mol]
C045-CG	0.45	5.0	0.75	7.8	70	---
	0.45	5.0	0.75	7.8	70	12
	0.45	5.0	0.50	7.8	70	---
	0.45	5.0	0.50	7.8	70	12
	0.45	5.0	0.25	7.8	70	---
	0.45	5.0	0.25	7.8	70	12
C075-CG	0.75	5.0	0.75	7.8	70	---
	0.75	5.0	0.75	7.8	70	12
	0.75	5.0	0.50	7.8	70	---
	0.75	5.0	0.50	7.8	70	12
	0.75	5.0	0.25	7.8	70	---
	0.75	5.0	0.25	7.8	70	12

5.5.2.1 Structural eigenstresses in specimen C075-CG – Effect of bond strength f_b

Figure 5.11a shows the structural eigenstresses in the specimen C075-CG for three values of the bond/matrix tensile strength ratio f_b/f_m and with stress relaxation. The maximum value of the eigenstresses strongly depends on the bond strength. The final value of the eigenstresses for a strain of $1.1 \cdot 10^{-3}$ m/m are more or less proportional to the values of the bond/matrix tensile strength ratio.

The microcrack damage ratio D_{mc} of the specimens analysed in figure 5.11a is shown in figure 5.11b. The curves in this figure show that for f_b/f_m = 0.25 stress relaxation has a minimal influence on the reduction of the damage ratio D_{mc}.

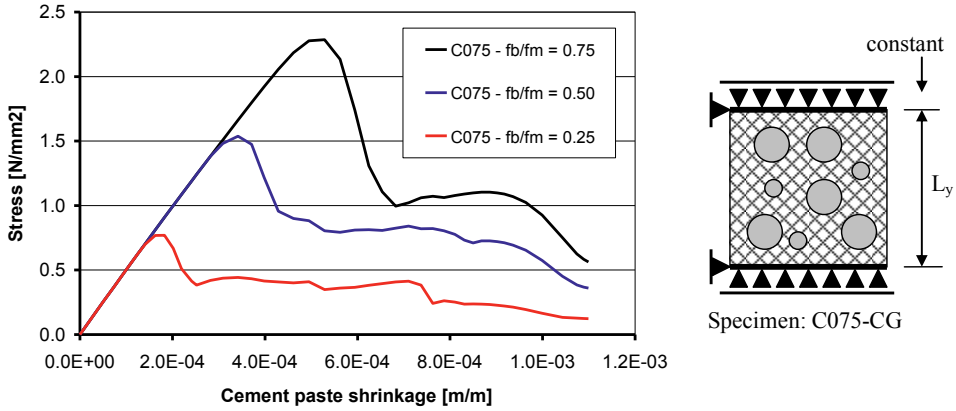

a. The *structural* eigenstress at macro-level, $\sigma_{se,macro}$, in the specimens C075-CG with stress relaxation

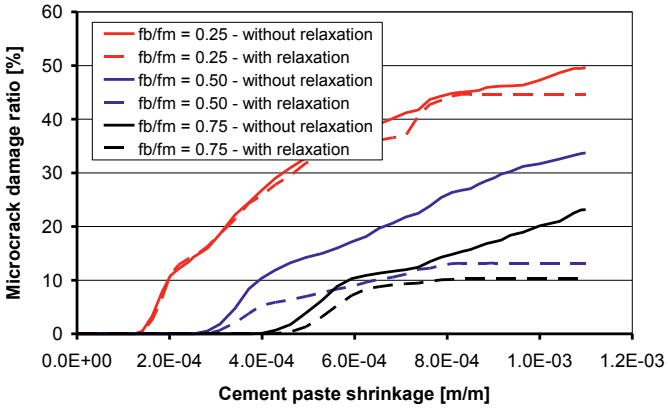

b. Microcrack damage ratios D_{mc} in specimens C075-CG with different bond strength

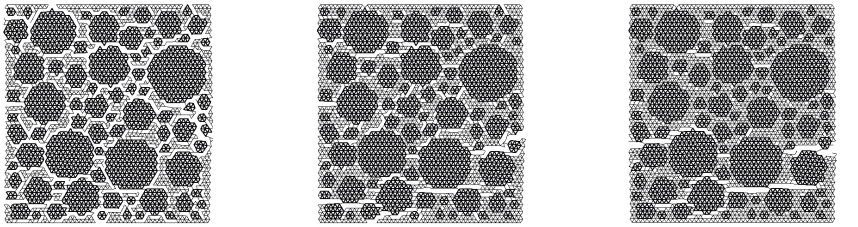

f_b/f_m = 0.25; D_{mc} = 44.7% f_b/f_m = 0.50; D_{mc} = 13.2% f_b/f_m = 0.75; D_{mc} = 10.2%

c. Crack patterns in specimen C075 at maximum cement paste shrinkage: $\varepsilon_{p,sh} = 1.1 \cdot 10^{-3}$ m/m. (situation with moderate relaxation).

Figure 5.11 *Structural* eigenstress $\sigma_{se,macro}$ (a), damage ratio D_{mc} and crack pattern at maximum imposed strain $1.1 \cdot 10^{-3}$ m/m (c) for specimens C075-CG with bond/matrix tensile strength ratios f_b/f_m = 0.75, 0.50 and 0.25, calculated without and with (moderate) relaxation.

This in contrast with the cases for the higher bond/matrix tensile strength ratios, i.e. f_b/f_m = 0.50 and 0.75. In those cases stress relaxation has a substantial influence on reducing the microcrack damage ratios. For f_b/f_m = 0.75 the final value of D_{mc} decreases from 23% (without stress relaxation) to 10% (with moderate stress relaxation). For f_b/f_m = 0.50 the reduction in the D_{mc} value is even larger, i.e. from 34% in the case without stress relaxation to 13% in the case with moderate stress relaxation.

The large effect of relaxation on the damage ratio for the mixture with high bond strength f_b explains the, at first sight, unexpected increase of stress in the post-peak stage of the stress-strain curve in figure 5.11a. A lower damage ratio means that more beams of the lattice model survive under the imposed shrinkage strain and are available for resisting forces generated by an additional strain increment.

The microcrack patterns in the stage that the full imposed shrinkage strain of $1.1 \cdot 10^{-3}$ m/m has been applied is shown in figure 5.11c. In the specimen with low bond strength, i.e. a bond/matrix tensile strength ratio f_b/f_m = 0.25, the crack pattern is dominated by the failure of the bond beams. With an increasing f_b/f_m ratio the microcracks are more concentrated and exhibit a more localized character.

5.5.2.2 Structural eigenstresses in specimen C045-CG – Effect of bond strength f_b

Figure 5.12a shows the calculated structural eigenstresses as a function of the imposed shrinkage strain for a mixture with a relatively low aggregate volume fraction of 45% and continuous aggregate grading. The peak values of the stress-strain curves for this mixture are quite similar to those presented in figure 5.11a for the mixture with an aggregate volume fraction of 75%. The eigenstresses at a maximum imposed strain of $1.1 \cdot 10^{-3}$ m/m are almost independent of the f_b/f_m ratio.

The microcrack damage ratio D_{mc} corresponding to the stress-strain curves of figure 5.12a are presented in figure 5.12b. Compared to the damage ratio curve presented in figure 5.11b for the mixture C075-CG, the damage ratios for mixture C045-CG are substantially lower. For a bond/matrix tensile strength ratio f_b/f_m = 0.25 the damage ratio D_{mc} at a maximum shrinkage strain of $1.1 \cdot 10^{-3}$ m/m has reached a value of 23% for the simulation with relaxation and 18% with relaxation for mixture C045-CG, whereas values of 50% and 44% were calculated for mixture C075-CG (Fig. 5.11b). The effect of relaxation on the damage ratio is more pronounced for higher bond strengths, i.e. higher values of the f_b/f_m ratio.

The crack patterns at the maximum strain of $1.1 \cdot 10^{-3}$ m/m are presented in figure 5.12c. Compared to the crack patterns in the mixture with an aggregate percentage of 75% (C075-CG), presented in figure 5.11c, the cracks seem to concentrate in areas with weak horizontal cross sections (see Fig. 5.12c).

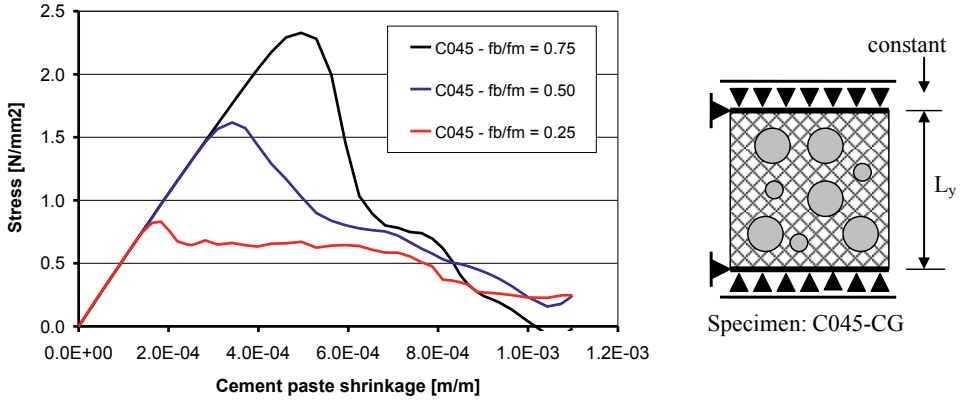

a. The *structural* eigenstress at macro-level, $\sigma_{se,macro}$, in the specimens C045-CG

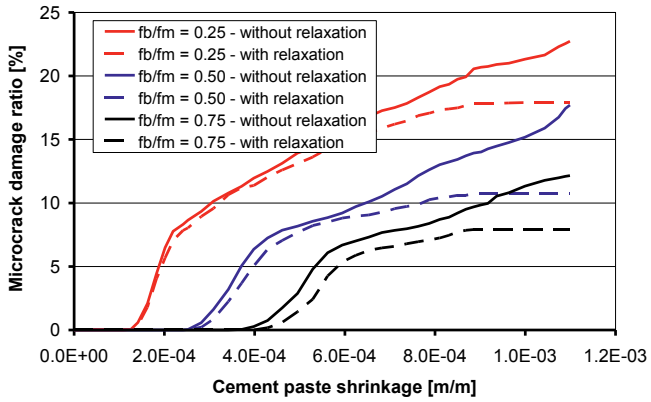

b. Microcrack damage ratios D_{mc} in specimens C045-CG with different bond strength

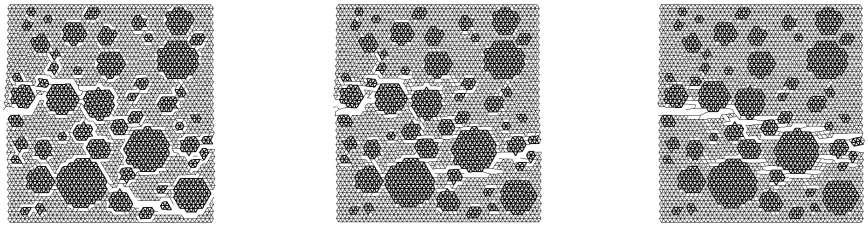

$f_b/f_m = 0.25$; $D_{mc} = 17.9\%$ | $f_b/f_m = 0.50$; $D_{mc} = 10.7\%$ | $f_b/f_m = 0.75$; $D_{mc} = 7.9\%$

c. Crack patterns in specimen C045 at maximum cement paste shrinkage: $\varepsilon_{p,sh} = 1.1 \cdot 10^{-3}$ m/m. (situation with moderate relaxation).

Figure 5.12 *Structural* eigenstress $\sigma_{se,macro}$ (a), damage ratio D_{mc} and crack pattern at maximum imposed strain $1.1 \cdot 10^{-3}$ m/m (c) for specimens C045-CG with bond/matrix tensile strength ratios f_b/f_m = 0.25, 0.50 and 0.75, calculated without and with (moderate) relaxation.

5.5.3 Structural eigenstresses and microcracking – Influence of aggregate stiffness E_a

The influence of aggregate stiffness on the magnitude of stresses and microcracking is analysed for mixture C075-CG. For the aggregate stiffness E_a values of 120 GPa, 70 GPa and 35 GPa are used. The calculations are carried out with and without and moderate stress relaxation. The tensile strength of the cement paste is f_m = 5.0 MPa and a bond/matrix tensile strength ratio of 0.75 is adopted. The test program with the specimens and material parameters is listed in Table 5.6.

Table 5.6 Test program: specimens and material parameters for the analysis of aggregate stiffness

Specimen Code (Table 5.1)	Aggregate Volume Fraction V_a [m^2/m^2]	Material parameters f_m [MPa]	f_b / f_m [-]	$E_m = E_b$ [GPa]	E_a [GPa]	Moderate relaxation U_0 [kJ/mol]
C075-CG	0.75	5.0	0.75	7.8	120	---
		5.0	0.75	7.8	120	12
		5.0	0.75	7.8	70	---
		5.0	0.75	7.8	70	12
		5.0	0.75	7.8	35	---
		5.0	0.75	7.8	35	12

Figure 5.13a shows the structural eigenstress as a function of the imposed shrinkage of mixtures C075-CG for different aggregate stiffness. As expected the stiffness of the specimens decreases with decreasing stiffness of the aggregate. With decreasing aggregate stiffness the maximum tensile eigenstress decreases slightly, irrespective of the presence of relaxation. In the post-peak stage, however, relaxation does have an effect. Because of stress relaxation more beams of the lattice model remain intact and remain available for the stiffness of the sample. This results in a slight increase of the stresses at increasing imposed strain. In the post-peak stage, from $0.7 \cdot 10^{-3}$ m/m to $1.0 \cdot 10^{-3}$ m/m, the specimen with aggregate stiffness E_a = 35GPa shows the highest eigenstresses with moderate stress relaxation, whereas the lowest eigenstresses are found in the specimen with an aggregate stiffness of 70 GPa.

The structural eigenstress at the maximum imposed shrinkage strain $\varepsilon_{p,sh} = 1.1 \cdot 10^{-3}$ m/m is about 0.5 – 0.7 N/mm^2, irrespective of the role of stress relaxation.

Figure 5.13b shows the evolution of the damage ratios as a function of the imposed shrinkage. In the crack propagation stage, from $0.4 \cdot 10^{-3}$ m/m to $0.7 \cdot 10^{-3}$ m/m, the stiffness of the aggregate does have an influence on the magnitude of microcracking. During further increase of the imposed shrinkage the aggregate stiffness hardly affects the magnitude of ongoing crack propagation. With increasing shrinkage strain, from about $0.7 \cdot 10^{-3}$ m/m to the maximum value of $\varepsilon_{p,sh} = 1.1 \cdot 10^{-3}$ m/m, the microcrack damage ratio remains about constant at 10% if relaxation is taken into account. In the case without stress relaxation the value of the microcrack damage ratio increases about linear with the increasing shrinkage strain.

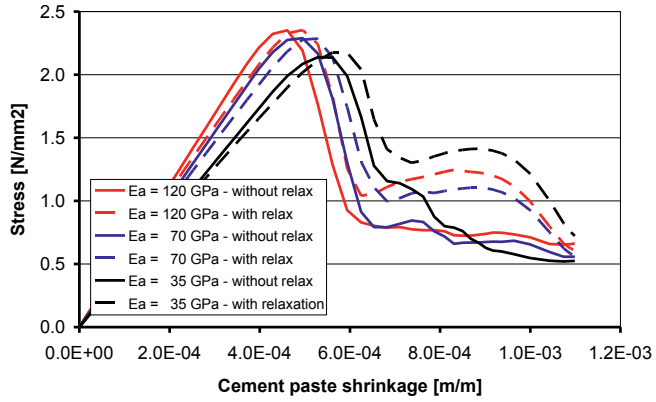

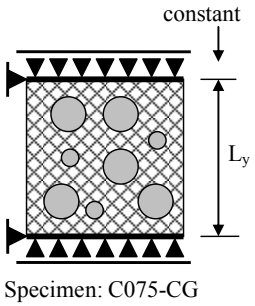

Specimen: C075-CG

a. *Structural* eigenstress at macro-level, $\sigma_{se,macro}$, in the specimens C075-CG

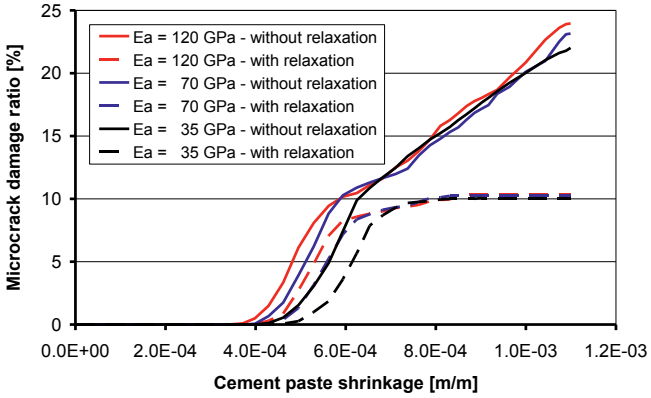

b. Microcrack damage ratios D_{mc} in specimens C075-CG with different bond strength

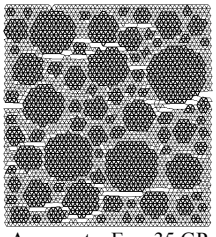

Aggregate: E_a = 35 GPa
D_{mc} = 10.1%

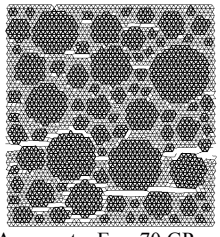

Aggregate: E_a = 70 GPa
D_{mc} = 10.2%

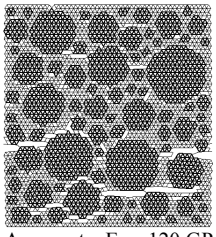

Aggregate: E_a = 120 GPa
D_{mc} = 10.3%

c. Crack patterns in specimen C075-CG with different aggregate stiffness for $\varepsilon_{p,sh} = 1.1 \cdot 10^{-3}$ m/m. (situation with moderate relaxation).

Figure 5.13 Structural eigenstress $\sigma_{se,macro}$ and crack patterns in specimen C075-CG with and without relaxation. Aggregate stiffness: E_a = 35, 70 and 120 GPa.

5.5.4 Eigenstresses and microcracking – Influence of particles size and grading

The influence of particle size and particle size distribution (PSD) of the aggregate on the magnitude of *structural* eigenstresses and microcracking is analysed for mixtures with aggregate volume fractions of 0.08 m^2/m^2 and 0.60 m^2/m^2. The calculations are carried out with and without (moderate) stress relaxation. The test program and material parameters – including notation of test specimens - are listed in Table 5.7.

Table 5.7 Test program: specimens and material parameters for the analysis of the effect of particle size and particle size distribution on structural eigenstress.

Specimen Code (Table 5.1)	Aggregate volume fraction V_a [m^2/m^2]	Material parameters f_m [MPa]	f_b / f_m [-]	$E_m = E_b$ [GPa]	E_a [GPa]	Moderate relaxation U_0 [kJ/mol]
C008-SP-16	0.08	5.0	0.75	7.8	70	---
	0.08	5.0	0.75	7.8	70	12
C008-MP-3 [1])	0.08	5.0	0.75	7.8	70	---
	0.08	5.0	0.75	7.8	70	12
C060-MP-3/16 [2])	0.60	5.0	0.75	7.8	70	---
	0.60	5.0	0.75	7.8	70	12
C060-MP-4 [3])	0.60	5.0	0.75	7.8	70	---
	0.60	5.0	0.75	7.8	70	12
C060-MP-8 [4])	0.60	5.0	0.75	7.8	70	---
	0.60	5.0	0.75	7.8	70	12
C060-CG	0.60	5.0	0.75	7.8	70	---
	0.60	5.0	0.75	7.8	70	12

1) C008-MP-3 multi particle specimen with 28∅3 mm (0.08 m^2/m^2)
2) C060-MP-3/16 multi particle specimen with 1∅16+176∅3 mm (0.60 m^2/m^2)
3) C060-MP-4 multi particle specimen with 115∅4 mm (0.60 m^2/m^2)
4) C060-MP-8 multi particle specimen with 29∅8 mm (0.60 m^2/m^2)

5.5.4.1 Structural eigenstress in the specimens C008-SP-16 and C008-MP-3

Figure 5.14 shows the evolution of the structural eigenstress as a function of the imposed shrinkage. In the pre-peak stage the eigenstresses are identical for both specimens. In the post-peak stage, i.e. for a shrinkage strain ≥ $0.7 \cdot 10^{-3}$ m/m, the eigenstress in specimen C008-SP-16 decreases to 0.3 – 0.5 N/mm^2, without relaxation, and to about 0.5 N/mm^2 in specimen C008-MP-3, also without stress relaxation. When relaxation is taken into account the eigenstresses in the post-peak stage in specimen C008-SP-16 (one aggregate particle ∅ 16 mm) are higher than the eigenstresses in specimen C008-MP-3 (28 particles ∅ 3 mm).

Figure 5.14b shows the damage ratio in the specimens C008-SP-16 and C008-MP-3 as a function of the imposed shrinkage, with and without stress relaxation. In specimen C008-SP-16 microcracking starts at a lower shrinkage strain than in specimen C008-MP-3.

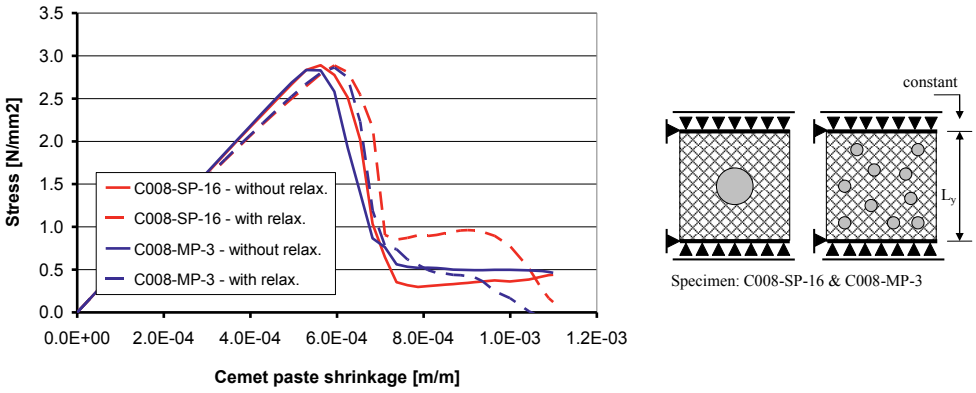

a. *Structural* eigenstress at macro-level, $\sigma_{se,macro}$, in the specimens C008-SP-16 and C008-MP-3

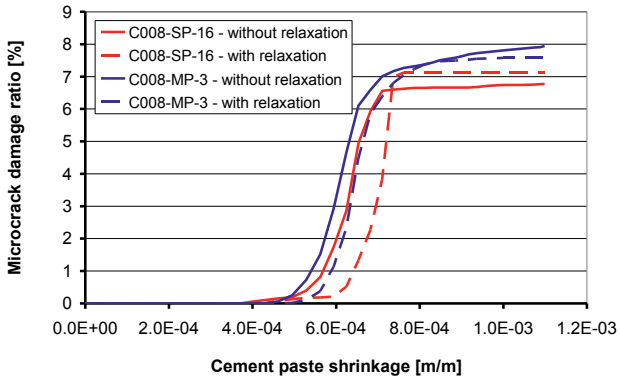

b. Microcrack damage ratios D_{mc} in specimens C008-SP-16 and C008-MP-3

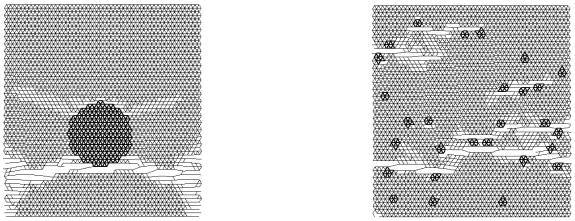

Specimen C008-SP-16
D_{mc} = 7.8%

Specimen C008-MP-3
D_{mc} = 7.6%

c. Crack patterns in specimen C008-SP-16 and C008-MP-3 at maximum shrinkage: $\varepsilon_{p,sh} = 1.1 \cdot 10^{-3}$ m/m. (situation with moderate relaxation).

Figure 5.14 The *structural* eigenstress $\sigma_{se,macro}$ in specimens with aggregate volume fraction 0.08 m^2/m^2 with different particle configuration (a), microcrack damage ratio D_{mc} (b), and crack patterns (c). Calculations with and without relaxation. Activation energy U_0 = 12 kJ/mol. Specimen code: see Table 5.1.

For the situation without relaxation the microcrack damage ratio for specimen C008-SP-16 remains lower (D_{mc} = 6.8%) than for specimen C008-MP-3 (D_{mc} = 8.0%). With moderate stress relaxation the microcrack damage ratio in specimen C008-SP-16 is a bit lower (7.1%) compared to the value (7.6%) in specimen C008-MP-3.

Figure 5.14c shows the crack patterns in the two specimens in the case of stress relaxation. In specimen C008-SP-16 microcracking is concentrated in the weakest cross-section at the bottom of the aggregate particle. Specimen C008-MP-3 has about the same number of microcracks as specimen C008-SP-16, but cracking is more spread over the specimen. An explanation for this is that the number of relatively weak bond-beams in specimen C008-MP-3 is much higher than in specimen C008-SP-16. In specimen C008-MP-3 the number of bond-beams relative to the total number of beams is 7.2%, whereas in specimen C008-SP-16 this number is 1.5%.

5.5.4.2 Structural eigenstress in C060-MP-3/16, C060-MP-4, C060-MP-8 and C060-CG

Stress-strain curves for the multi particle specimens C060-MP-3/16, C060-MP-4, C060-MP-8 and C060-CG are presented in figure 5.15. In these mixtures the aggregate volume fraction is the same, i.e. 60%.

Figure 5.15a shows that the evolution of the structural eigenstresses is more or less independent of the mix composition, both in the pre-peak and post-peak stage and irrespective of relaxation. The eigenstresses at the maximum imposed strain of $1.1 \cdot 10^{-3}$ m/m are about 0.3 – 0.6 N/mm^2.

The effect of the particle size and particle size distribution on the evolution and magnitude of the microcrack damage ratio is presented in figure 5.15b. For all mixtures the figure shows a clear effect of relaxation. In the case without stress relaxation the microcrack damage ratio D_{mc} continuously increases with increasing imposed strain. The damage ratio is higher the greater the mean value of the particle size of the aggregate. Specimen C060-MP-8 (mean aggregate size is ∅8 mm) has the highest D_{mc} (19.4%). Specimens C060-MP-4 (particle size ∅4 mm) and C060-CG (mean particle size ∅4.9 mm) have about the same damage ratio, viz. 17.3%. Specimen C060-MP-3/16, with a mean aggregate size of ∅3.1 mm, shows the lowest microcrack damage ratio, i.e. 15.7%.

When relaxation is taken into account the evolution and final value of the microcrack damage ratio is about the same for all specimens. Obviously the damage ratios are predominantly determined by the boundary conditions (full restraint), while the effect of the aggregate grading appears to be less.

Figure 5.15c shows the crack patterns in the four specimens C060-SP-3/16, C060-MP-4, C060-MP-8 and C060-CG. For specimen C060-CG with continuous particle grading the crack patterns are shown for the situation without and with relaxation. The crack patterns of the specimens C060-SP-3/16, C060-MP-4, C060-MP-8 show that with increasing aggregate particle size the microcracking is more concentrated in a smaller number of macro-cracks.

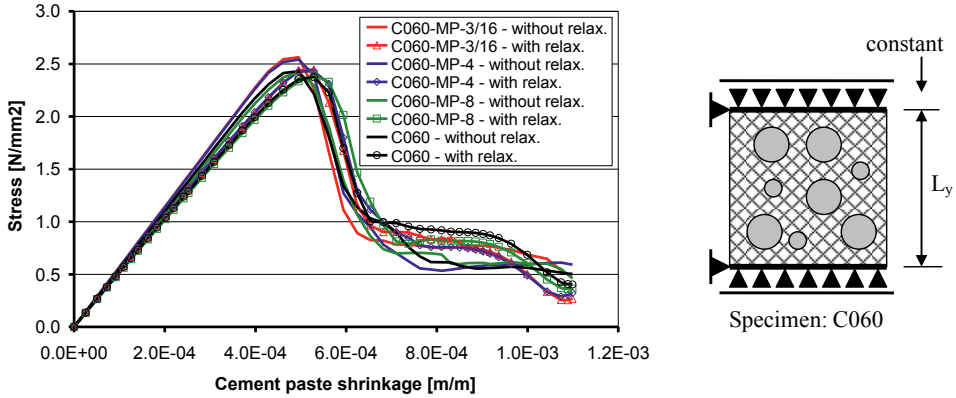

a. *Structural* eigenstress $\sigma_{se,macro}$ in specimens C060-MP-3/16, C060-MP-4, C060-MP-8, C060-CG

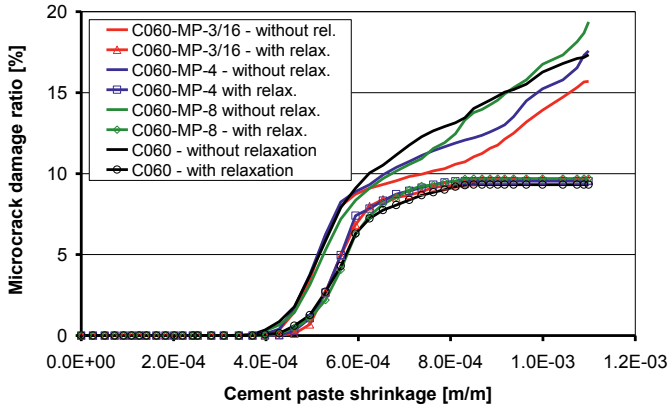

b. Microcrack damage ratios D_{mc} in specimens C060-MP-3/16, C060-MP-4, C060-MP-8, C060-CG

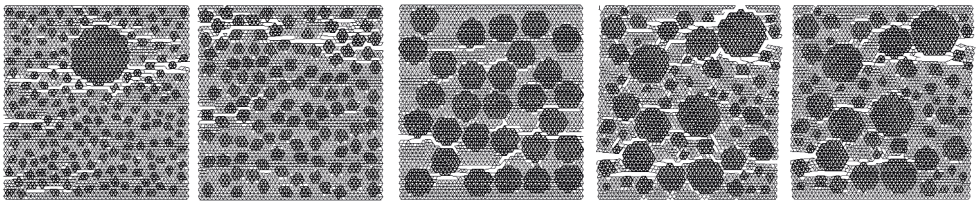

C060-MP-3/16	C060-MP-4	C060-MP-8	C060-CG	C060-CG
D_{mc} = 9.6%	D_{mc} = 9.5%	D_{mc} = 9.7%	D_{mc} = 17.3%	D_{mc} = 9.3%
:			No relaxation	With relaxation

c. Crack patterns in specimen C060-MP-3/16, C060-MP-4, C060-MP-8, C060-CG at $\varepsilon_{p,sh}=1.1\cdot10^{-3}$ m/m (situation with moderate relaxation).

Figure 5.15 *Structural* eigenstress $\sigma_{se,macro}$ in specimens with aggregate volume fraction 0.60 m^2/m^2, without and with moderate stress relaxation for specimen C060-SP-3/16, C060-MP-4, C060-MP-8 and C060-CG. Activation energy U_0 = 12 kJ/mol.

In the case with stress relaxation cracking concentrates mainly in the bond beams. In specimen C060-MP-3/16 (D_{mc} = 9.6%) with 8.2% in bond beams; C060-MP-4: (D_{mc} = 9.5%) with 8.5% in bond beams; C060-MP-8: (D_{mc} = 9.7%) with 8.1% in bond beams; C060-CG: (D_{mc} = 9.3%) with 8.2% in bond beams.

The crack pattern in specimen C060-CG shows that the microcracking tends to concentrate at the top and bottom of the bigger particles and individual microcracks merge to macrocracks. Microcracking is reduced to a great extent (about 50% at an imposed strain of 1.1 10^{-3} m/m) when stress relaxation is taken into account.

5.5.5 Effect of activation energy on relaxation of structural eigenstresses

The influence of the magnitude of the activation energy U_0 on the relaxation of eigenstresses and microcracking is analysed for a specimen made of cement paste and specimens with aggregate volume fractions V_a = 0.08 and 0.60 m^2/m^2. The calculations are carried out with three values of the initial activation energy U_0, viz. U_0 = 20 kJ/mol (low stress relaxation), U_0 = 12 kJ/mol and 10 kJ/mol. The test program with the specimens and material parameters is listed in Table 5.8.

Table 5.8 Test program: specimens and material parameters for the analysis of the effect of the magnitude of relaxation on eigenstresses.

Specimen Code (Table 5.1)	Aggregate Volume Fraction V_a [m^2/m^2]	Material parameters				
		f_m [MPa]	f_b / f_m [-]	$E_m = E_b$ [GPa]	E_a [GPa]	U_0 [kJ/mol]
Matrix	---	5.0	---	7.8	---	---
		5.0	---	7.8	---	20
		5.0	---	7.8	---	12
		5.0	---	7.8	---	10
C008-SP-16 [1])	0.08	5.0	0.75	7.8	70	---
	0.08	5.0	0.75	7.8	70	20
	0.08	5.0	0.75	7.8	70	12
	0.08	5.0	0.75	7.8	70	10
C060-MP-3/16 [2])	0.60	5.0	0.75	7.8	70	---
	0.60	5.0	0.75	7.8	70	20
	0.60	5.0	0.75	7.8	70	12
	0.60	5.0	0.75	7.8	70	10
C060-CG	0.60	5.0	0.75	7.8	70	---
	0.60	5.0	0.75	7.8	70	20
	0.60	5.0	0.75	7.8	70	12
	0.60	5.0	0.75	7.8	70	10

1) C008-SP-16 : single particle specimen with 1∅16 mm (0.08 m^2/m^2)

2) C060-MP-3/16 : multi particle specimen with 1∅16+176∅3 mm (0.60 m^2/m^2)

5.5.5.1 Structural eigenstresses in cement paste specimen - Effect of relaxation

Figure 5.16 shows the evolution of structural eigenstresses in a cement paste specimen of which the shrinkage is restrained. Without stress relaxation the eigenstress is a linear function of the imposed shrinkage strain until the moment the tensile strength (f_m = 5.0 N/mm^2) is

reached. In the case with low stress relaxation (U_0 = 20 kJ/mol) microcracking does occur. With higher stress relaxation, i.e. U_0 = 12 kJ/mol, the eigenstress is reduced and the tensile strength is not reached. With a still higher stress relaxation, i.e. U_0 = 10 kJ/mol, the stresses are even further reduced.

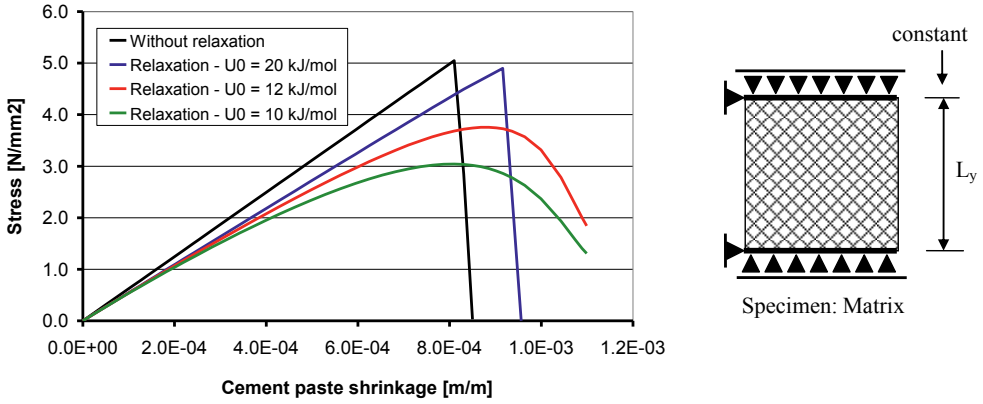

Figure 5.16 *Structural* eigenstress $\sigma_{se,macro}$ in cement paste specimen without relaxation, with low stress relaxation (U_0 = 20 kJ/mol) and increasing stress relaxation (U_0 = 12 and 10 kJ/mol).

Note that with increasing cement paste stiffness (E_m) the effect of relaxation is not always high enough to prevent cracking to occur (see Fig. 5.8). If stress relaxation is taken into account, the tensile eigenstresses at the end of the simulation period are in the order of 1.0 to 2.0 N/mm^2.

5.5.5.2 Structural eigenstress in specimen C008-SP-16: Effect of relaxation

Figure 5.17 shows the evolution of the structural eigenstresses in a specimen containing one aggregate particle with diameter 16 mm, C008-SP-16, without stress relaxation and with moderate and high stress relaxation. In all the cases the specimen failed, irrespective of the presence of relaxation. The effect of the magnitude of stress relaxation in specimen C008-SP-16 is that high stress relaxation lowers the eigenstresses in the post-peak stage. The residual eigenstresses in this specimen at maximum shrinkage are all around 0.5 N/mm^2.

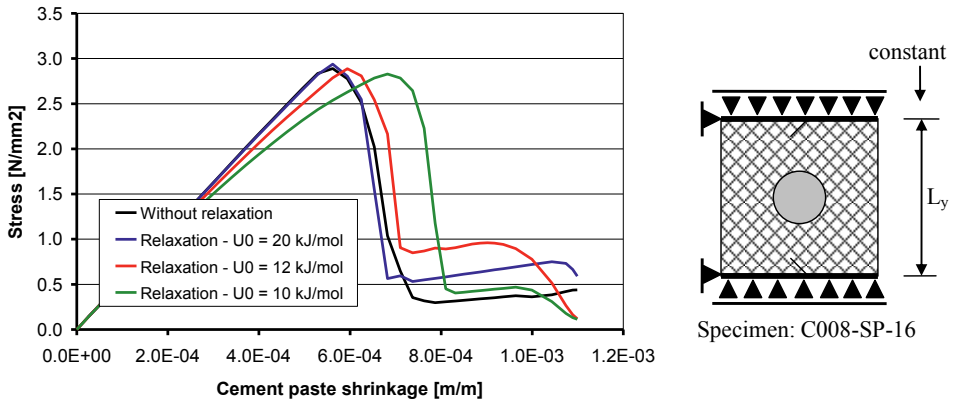

Figure 5.17 The *structural* eigenstress at macro-level ($\sigma_{SE(macro)}$) in specimen C008-SP-16 without relaxation and with stress relaxation (U_0 = 20, 12 and 10 kJ/mol).

5.5.5.3 Structural eigenstress and cracking - Continuous aggregate grading

C060-MP-3/16 and C060-CG: Effect of relaxation

Figure 5.18 shows the structural eigenstresses and microcrack damage ratio in specimens C060-MP-3/16 and C060-CG for a situation without relaxation and with moderate and high relaxation.

The evolution of the structural eigenstresses is presented in figure 5.18a. The figure shows that in specimen with high relaxation the occurrence of the peak stress was somewhat postponed compared to the peak stresses in the specimen without and with moderate and low relaxation. In the post-peak stage the eigenstresses in the specimens without relaxation and moderate relaxation are about the same.

The evolution of the microcrack damage is illustrated in Figure 5.18b. The figure shows that without stress relaxation the microcrack damage ratio increases about proportional with increasing shrinkage strains. The value of the microcrack damage ratio in specimen C060-CG at the end of the simulation period is higher compared to the damage ratio in specimen C060-MP-3/16 (17.3% versus 15.7%). The reason for this is that the mean value of the aggregate size in the specimen with the continuous aggregate grading, C060-CG, is higher than the mean aggregate size in specimen C060-MP-3/16 (∅4.9 mm in specimen C060-CG and ∅3.1 mm in specimen C060-MP-3/16).

With low stress relaxation, i.e. U_0 = 20 kJ/mol, the values of the microcrack damage ratios in both specimens (C060-MP-3/16 and C060-CG) are somewhat lower compared to the case without relaxation, but still show almost identical values at the end of the simulation period.

With stress relaxation with U_0 = 12 kJ/mol the evolution of the microcrack damage ratios in the specimens C060-MP-3/16 and C060-CG is about the same. In the case with U_0 = 10 kJ/mol specimen C060-CG performs slightly better with a residual microcrack damage ratio of 6.3% compared to the residual microcrack damage ratio of 7.5% in specimen C060-MP-3/16.

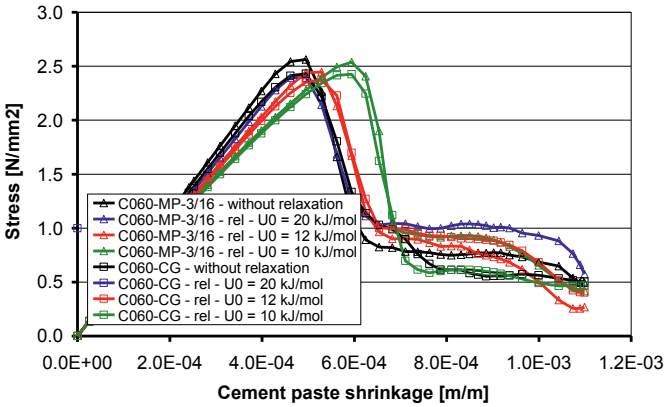

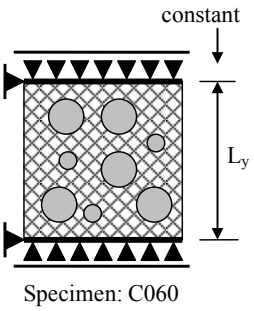

a. Effect of relaxation on the evolution of *structural* eigenstresses $\sigma_{se,macro}$

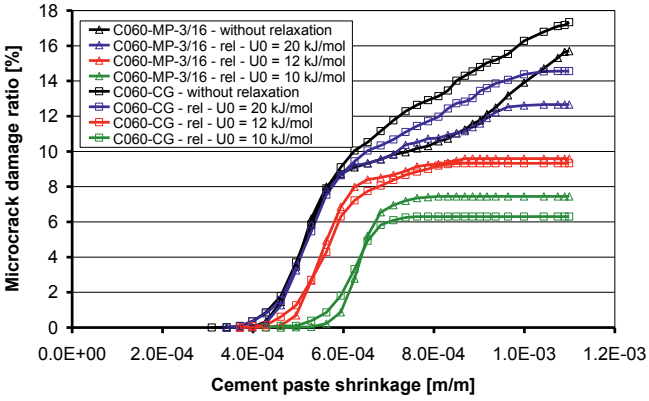

b. Effect of relaxation on the evolution of microcracking

Figure 5.18 Evolution of structural eigenstresses and microcracking in specimens C060-MP-3/16 and C060-CG without relaxation and with relaxation. Low relaxation for U_0 = 20 kJ/mol, and higher relaxation for U_0 = 12 and 10 kJ/mol.

5.6 Distribution of stresses in the cross-section of cement paste

5.6.1 Description of procedure for numerical stress analysis

In the previous sections the evolution of the structural (eigen)stresses, $\sigma_{se,macro}$, and the intensity of microcracking were analysed for a variety of specimen parameters. These structural eigenstresses and the microcracking were the result, at macroscopic level, of the shrinkage of the paste. In this section the focus will be on the development of the stresses in the cement paste in an arbitrary cross-section of the specimen. These analyses will be carried out for

specimen C045-CG. For that specimen the evolution of the structural eigenstress $\sigma_{se,macro}$ is presented in figure 5.12a. A schematic picture of the relationship between the macro stress $\sigma_{se,marco}$ and the imposed shrinkage ε_{sh} is shown in the top-right part of figure 5.19. For the imposed shrinkage strains $\varepsilon_{sh,A}$, $\varepsilon_{sh,B}$ and $\varepsilon_{sh,C}$ the stresses in the cement matrix in an arbitrarily chosen cross-section, viz. y = 32.5 mm from the bottom of the specimen, are indicated schematically in figure 5.19 (middle of the figure). For equilibrium makes that the mean stress in the cross-section equals the macroscopic stress $\sigma_{se,macro}$.

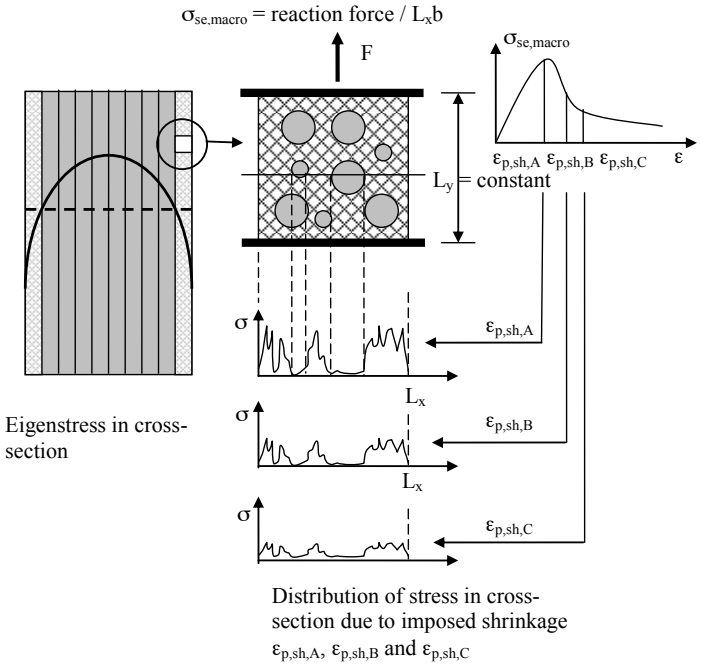

Figure 5.19 Schematic representation of distribution of eigenstresses in an arbitrarily chosen cross-section of a concrete specimen at different values of the imposed shrinkage, i.e. $\varepsilon_{sh,A}$, $\varepsilon_{sh,B}$, $\varepsilon_{sh,C}$.

5.6.2 Results of numerical stress analyses in arbitrary cross section

The distribution of stresses in specimen C045-CG for both $f_b/f_m = 0.75$ and 0.25 is analysed. Figures 5.20 and 5.21 give an overview of the stresses for $f_b/f_m = 0.75$ and 0.25, respectively.

Figure 5.20a shows the specimen of which the distribution of stresses is analysed. Figure 5.20b shows the (structural) stress-strain curve and the three strains $\varepsilon_{sh,A}$, $\varepsilon_{sh,B}$, $\varepsilon_{sh,C}$ for which the stresses in the cross-section at y = 32.5 mm are calculated. In the figures 5.20c, 5.20d and 5.20e the distributions of stresses in the cross-section are plotted for $f_b/f_m = 0.75$. The figures 5.21c, 5.21d and 5.21e show the stress distributions for the case when $f_b/f_m = 0.25$.

Figure 5.20a (and 5.21a) shows that in the cross-section at y = 32.5 mm three aggregate particles are present. Stresses in the aggregate particles are not presented in the stress histograms.

Figure 5.20c and 5.21c show the stresses in the matrix at the imposed shrinkage strain for which no cracking has occurred yet (damage ratio $D_{mc} = 0$). The stress distributions over the cross-section in the figures 5.20c and 5.21c are almost the same, beit that the stress level in the specimen with the high bond strength (Fig. 5.20c, $f_b/f_m = 0.75$) is substantially higher that in the specimen with low bond strength (Fig. 5.21c, $f_b/f_m = 0.25$).

Figures 5.20d shows the stresses in the matrix for the situation with a maximum structural eigenstress. For the specimen with strong paste-aggregate bond, $f_b/f_m = 0.75$, this maximum tensile stress is 2.3 MPa at an imposed strain of $495 \cdot 10^{-6}$ m/m (Fig. 5.20b). In the cross-section y = 32.5 mm the tensile stresses ranged from 0.5 to 3.5 MPa. At that moment the damage ratio D_{mc} was 1.4% (Fig. 5.20d).

For the specimen with low bond strength, $f_b/f_m = 0.25$, the maximum tensile stress is 0.8 MPa at an imposed strain of $182 \cdot 10^{-6}$ m/m (Fig. 5.21b). In the cross-section y = 32.5 mm the stresses in the not broken beams range from 0.3 to 1.4 MPa. The damage ratio at that moment was 4.1 % (Fig. 5.21d).

The stress distributions at high imposed shrinkage strains are shown in the Figures 5.20e and 5.21e. At shrinkage strains of $682 \cdot 10^{-6}$ m/m and $1043 \cdot 10^{-6}$ m/m for the specimens with strong and weak bond strength, respectively, microcracking has further continued. The damage ratio had reached a value of 6.5% and 17.9%, respectively. In those stages of the cracking process compressive stresses in the matrix appear. This illustrates internal redistribution of forces caused by disturbed force equilibria that result from microcracking.

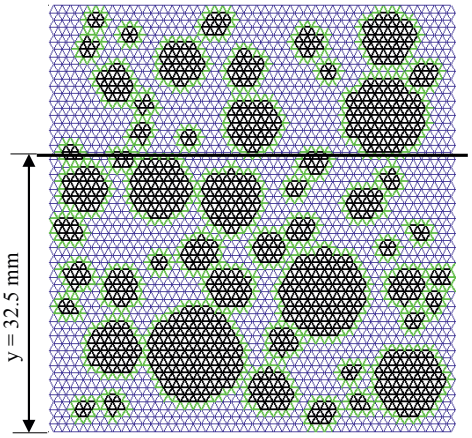

Fig. 5.20a Specimen C045-CG with cross-section for stress analysis

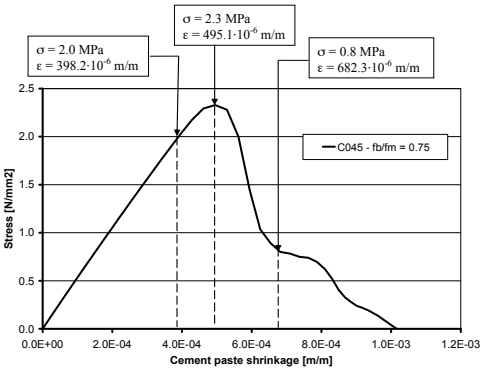

Fig. 5.20b Structural eigenstress in specimen C045-CG under imposed strain. $f_b/f_m = 0.75$

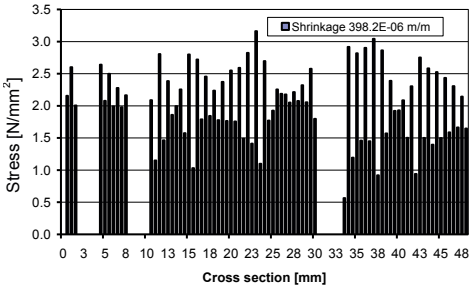

Fig. 5.20c Distribution of stresses in the matrix for imposed strain $\varepsilon = 398\ 10^{-6}$ m/m. Damage ratio: Dmc = 0% (no cracking)

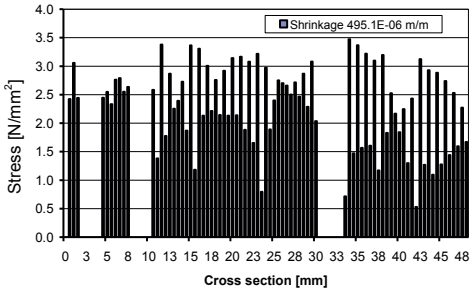

Fig. 5.20d Distribution of stresses in the matrix for imposed strain $\varepsilon = 495 \cdot 10^{-6}$ m/m. Damage ratio: Dmc = 1.4% (minor cracking)

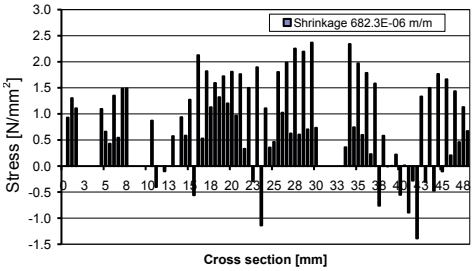

Fig. 5.20e Distribution of stresses in the matrix for imposed strain $\varepsilon = 682 \cdot 10^{-6}$ m/m. Damage ratio: Dmc = 6.5% (progressive cracking)

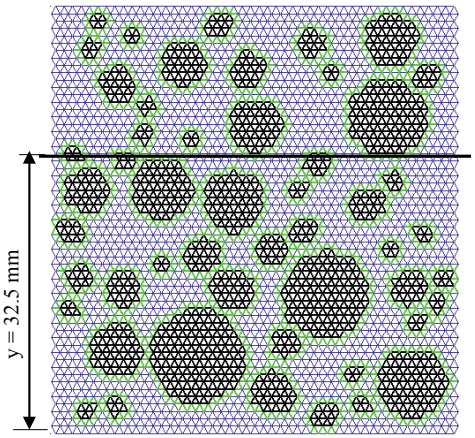

Fig. 5.21a Specimen C045-CG with cross-section for stress analysis

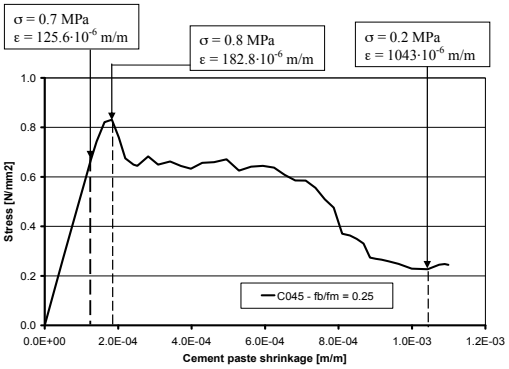

Fig. 5.21b Structural eigenstress in specimen C045-CG under imposed strain. $f_b/f_m = 0.25$

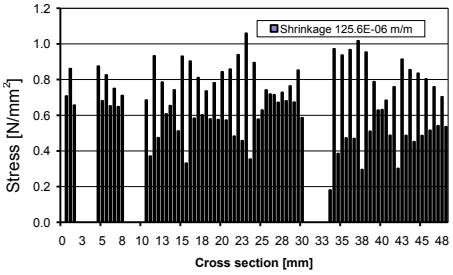

Fig. 5.21c Distribution of stresses in the maxtrix for imposed strain $\varepsilon = 126\ 10^{-6}$ m/m. Damage ratio: Dmc = 0% (no cracking)

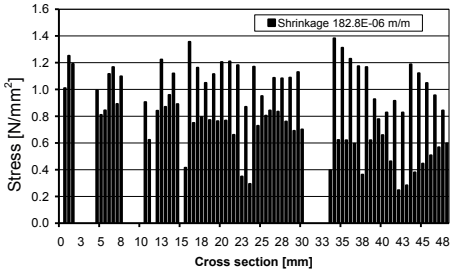

Fig. 5.21d Distribution of stresses in the matrix for imposed strain $\varepsilon = 183\ 10^{-6}$ m/m. Damage ratio: Dmc = 4.1% (cracking started)

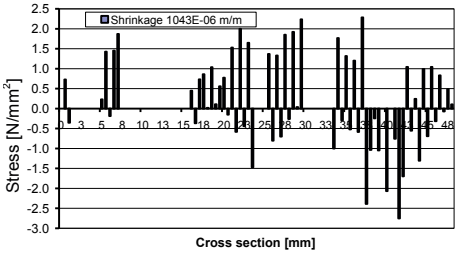

Fig. 5.21e Distribution of stresses in the matrix for imposed strain $\varepsilon = 1043 \cdot 10^{-6}$ m/m. Damage ratio: Dmc = 17.9% (severe cracking)

5.7 Material restraint versus structural restraint – Internal stresses

5.7.1 Specimen and materials

In the foregoing sections the overall response of 2D-specimens exposed to an imposed shrinkage strain has been evaluated. The figures 5.20 and 5.21 show that stresses in individual beams can be substantially different. Depending on their position in the specimen some beams crack, while other beams may even experience compression.

In this section the evolution of stresses in two matrix beams of a lattice will be monitored during the shrinkage process. The imposed shrinkage curve is the one presented in figure 5.6. The 2D-model is shown in figure 5.22. With L_x = 30 mm and L_y = 31.5 mm the specimen is slightly smaller than the specimen used in the previous sections (in order to reduce computation time). The aggregate volume fraction is 0.562 m^2/m^2, and the specimen is denoted as C0562. The E-modulus E_a of the aggregate is 70.0 GPa, and of the matrix and bond beams: $E_m = E_b$ = 7.8 GPa. The tensile strength of the matrix beams f_m = 5 MPa and for the bond beams f_b = 3.75 MPa (f_b/f_m = 0.75).

The two beams of which the evolution of stresses will be monitored are beams 1568 and 323, respectively (see Fig. 5.22). These are both matrix beams, located close to aggregate particles and also close to the ring of bond beams (green) surrounding these aggregate particles.

Two boundary conditions of the specimen will be considered, viz. *full* external restraint (structural restraint) and *no* external restraint (material restraint). Due attention will be given to the effect of relaxation on the stress evolution of the individual beams.

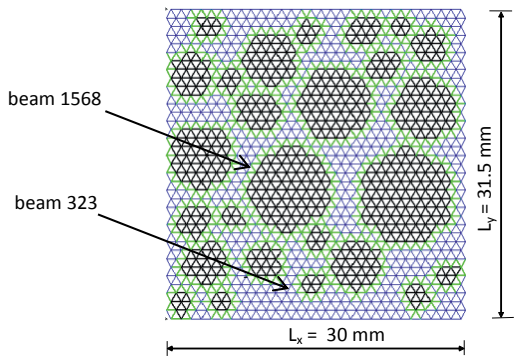

Figure 5.22 2D-specimen (C0562) used for analysis of the evolution of stresses in matrix beams 1568 and 323 of the lattice model. Specimen size L_x = 30 mm and L_y = 31.2 mm. Imposed shrinkage curve according to figure 5.6.

5.7.2 Structural restraint: Stresses in beams 1568 and 323

Figure 5.23 shows the evolution of the eigenstresses (Fig. 5.23a) and of the microcrack damage ratio's (Fig. 5.23b) in beams 1568 and 323, with and without stress relaxation.

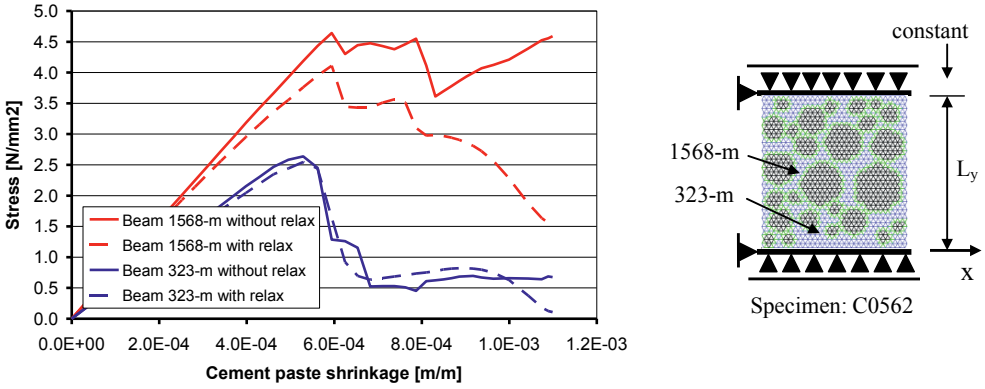

a. Stresses in beams 323 and 1568 of specimen C0562 in case of full (structural) restraint

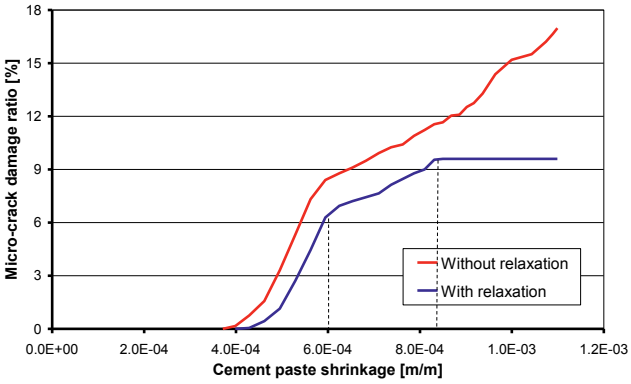

b. Microcrack damage ratios D_{mc} in specimen C0562 in case of full (structural) restraint

Figure 5.23 a) Eigenstresses and b) damage ratio D_{cm} in beams 323 and 1568 in specimen C0562 (Fig. 5.22) due to imposed shrinkage without relaxation and with stress relaxation (U_0 =12 kJ/mol). *Full* external restraint. f_m = 5.0 MPa, $E_m = E_b$ = 7.8 GPa, E_a = 70.0 GPa.

Deformations in vertical direction at y = 0 and y = L_y are completely restrained. Effect of relaxation on the generated stress is calculated for an activation energy U_0 = 12 kJ/mol.

In the initial linear elastic non-cracked stage the stresses in the beams are a linear function of the imposed shrinkage strain. Relaxation causes a slight reduction of the stresses. Because of the relatively short duration of the time under load the effect of relaxation remains limited. Neither beam 1568 nor beam 323 reach their tensile strength of 5 MPa. The reason for this is the occurrence of cracking in adjacent bond beams. Cracking of adjacent beams reduces the local degree of restraint of the beams 1568 and 323, causing a drop of the stress in those beams. The successive stress drops in beam 1568 are also caused by cracking of adjacent

beams. Especially in the case without relaxation the sudden stress drops due to cracking of adjacent beams are very clear.

The decrease of stresses in the beams 1568 and 323 caused by cracking of adjacent beams can be further explained with figure 5.23b. In this figure the damage ratio D_{mc} of the specimen is shown as a function of the imposed strain. The curves show that microcracking starts at an imposed shrinkage strain of $\approx 400 \cdot 10^{-6}$ m/m if no relaxation of stresses occurs, and at a shrinkage strain of $\approx 430 \cdot 10^{-6}$ m/m in case stress relaxation is considered. This means that at the moment that in the beams 1568 and 323 maximum stresses are reached (i.e. at imposed shrinkage strains of about $600 \cdot 10^{-6}$ m/m and $520 \cdot 10^{-6}$ m/m), microcracking has already started to affect the stress evolution in other beams in the specimen. This influences the stresses in the beams 1568 and 323. Before the stress in the latter beams could reach the beam tensile strength of 5 MPa, cracking of adjacent beams causes release of stress.

Even though the beams 1568 and 323 are both located close to bond beams and may have experienced the effect of cracking in adjacent bond beams, the stress evolution in these two beams is still much different. The local packing of aggregate particles appears to have a dominant impact on the evolution of stresses in individual beams.

The impact of cracking dominates the effect of relaxation. Only in the uncracked stage a small impact of relaxation can be observed. The impact of relaxation appears to be too small to prevent cracking of the beams to occur.

Figure 5.23b shows that in case stress relaxation is considered, no further microcracking occurs when the shrinkage strain has reached the value of about $830 \cdot 10^{-6}$ m/m.

5.7.3 Material restraint (no external restraint): Stresses in beams 1568 and 323

Figure 5.24 shows the evolution of stresses in beams 1568 and 323 in the case of *no* external restraint of the imposed shrinkage strains, i.e. material restraint. In this case the rigid aggregate particles determine the degree of restraint experienced by the matrix beams. Moreover, the position of the matrix beams relative to the aggregate particles and/or the free boundaries of the specimen is important. Beam 1568 is located close to the surface of a relative large aggregate particle. The restraint by this aggregate particle has a major inpact / influence on the (tensile) stress in this beam. Matrix beam 323 is located relatively close to a free boundary of the specimen and will experience much less restraint.

In the case without relaxation microcracking in the specimen results in a reduction of the stress in beam 1568 at an imposed strain of about $7.5 \cdot 10^{-4}$ m/m. At further developing shrinkage the stress in the beam increases again (see Fig. 5.24a). The tensile strength of 5 MPa was reached at an imposed strain of $1.1 \cdot 10^{-3}$ m/m and the beam failed.

The stress in beam 323, located close to the free boundary of the specimen, increased very slowly and almost linearly with increasing shrinkage strain. Stress relaxation in beam 323 is negligible as a result of the very low strain rate.

Figures 5.24b shows that in the case without stress relaxation microcracking starts at an imposed deformation of $5.6 \cdot 10^{-4}$ m/m. Compared to the case of structural restraint the moment of first cracking is slightly postponed. At a maximum imposed shrinkage strain of $1.1 \cdot 10^{-3}$ m/m the damage ratio reached the value $D_{mc} = 9.1\%$. In the simulations with relaxation the stresses did not reach the tensile strength and cracking did not occur.

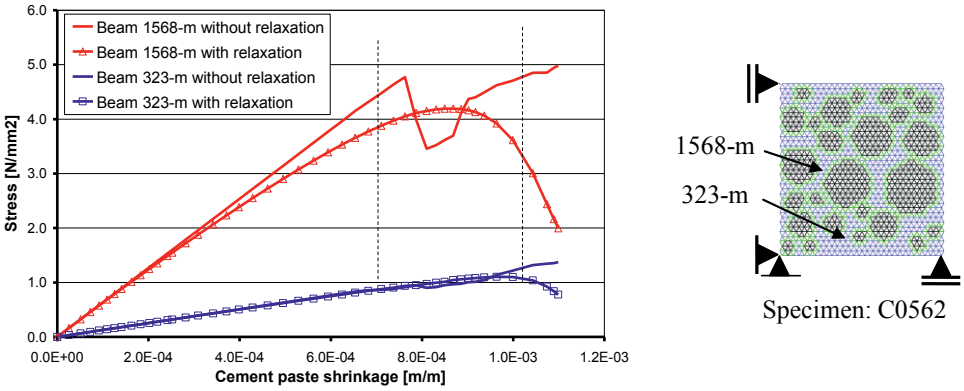

a. Specimen C0562: evolution of stress in beams 1568 and 323 in case of material restraint (no external restraint)

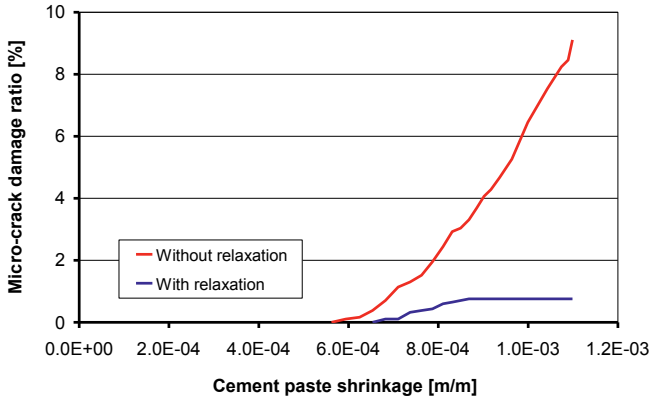

b. Microcrack damage ratio D_{mc} in specimen C0562 in case of no external restraint (material restraint).

Figure 5.24 Evolution of stresses (a) and damage ratio D_{cm} (b) in beams 323 and 1568 in specimen C0562 Analysis without and with stress relaxation (U_0 =12 kJ/mol). *No* external restraint. f_m = 5.0 MPa, $E_m = E_b$ = 7.8 GPa, E_a = 70.0 GPa.

5.8 Influence of the rate of shrinkage on eigenstresses

5.8.1 Imposed shrinkage curves and mixture composition of numerical test specimen

All the numerical analyses presented in the sections 5.5 to 5.7 were performed with the imposed shrinkage curve of the cement paste given in figure 5.6. In this section the effect of the shape of the shrinkage curve on the evolution and magnitude of eigenstresses and microcracking will be analysed. Two additional shrinkage curves will be considered namely, curves 2 and 3, which are both presented in figure 5.25, together with the original shrinkage curve 1 from figure 5.6.

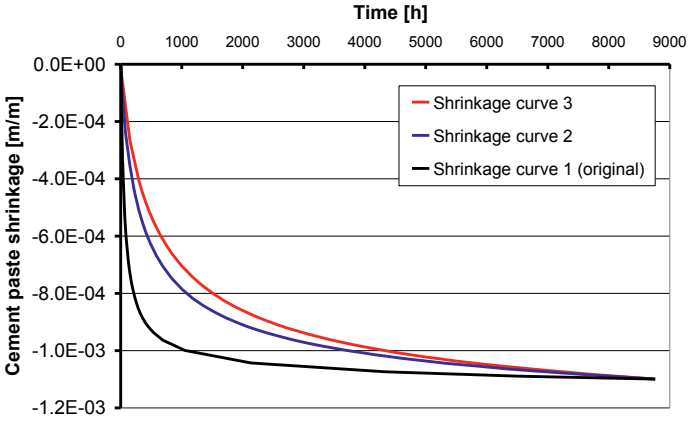

Figure 5.25 Original shrinkage curve (1) with two additional curves 2 and 3, used as input for numerical analysis of the effect of the rate of shrinkage development on stresses and cracking.

The shrinkage curves in figure 5.25 have in common that they all reach the maximum shrinkage (~ $1.1 \cdot 10^{-3}$ m/m) after 8760 h. The initial rate of shrinkage of the shrinkage curve 2 is lower compared to the original shrinkage curve 1 and that of curve 3 is lower than that of curve 2. Since the effect of relaxation is strain rate dependent, the stresses generated by the three shrinkage curves will be different.

The analyses will be carried out for mixture C075-CG (see also Table 5.1). Data of the mixture composition of the numerical test specimen and other input parameters are summarized in Table 5.9.

Table 5.9 Test program: specimen and material parameters for the analysis of the effect of the shrinkage strain rate on the magnitude of relaxation of eigenstresses.

Specimen Code (Table 5.1)	Aggregate Volume Fraction V_a [m^2/m^2]	Material parameters				
		f_m [MPa]	f_b/f_m [-]	$E_m = E_b$ [GPa]	E_a [GPa]	Relaxation Act.energy U_0 [kJ/mol]
075-CG	0.75	5.0	0.75	7.8	70	12

5.8.2 Evolution of stresses without relaxation (linear elastic analysis)

In the case without stress relaxation the eigenstresses in the specimen follow from the imposed strains, beam stiffnesses and microcracking. Figure 5.26 shows the structural eigenstress at macro-level in specimen C075-CG, calculated without stress relaxation, as a function of the imposed shrinkage strain. The figure shows that for the case *without* stress relaxation the different shrinkage curves do not influence the evolution of the eigenstress. Curves for shrinkage curves 1, 2 and 3 are identical, figure 5.26 shows only one curve, the curves coincide. The increase of eigenstress is linear in the non-cracked stage up to a shrinkage strain of about $370 \cdot 10^{-6}$ m/m is reached.

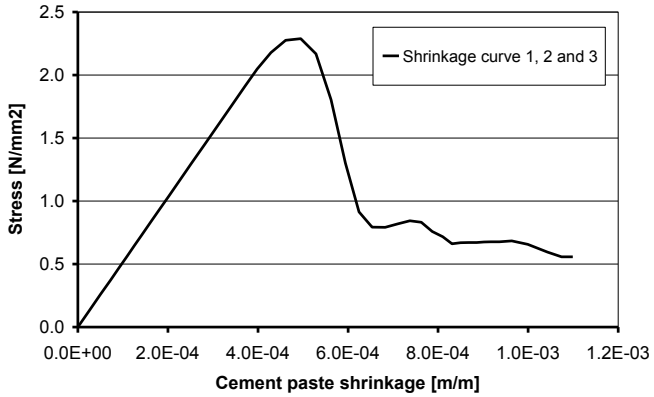

Figure 5.26 The *structural* eigenstress at macro-level ($\sigma_{se,macro}$) in specimen C075-CG, without stress relaxation, due to imposed shrinkage according to three different shrinkage curves 1, 2 and 3 (Fig. 5.25).

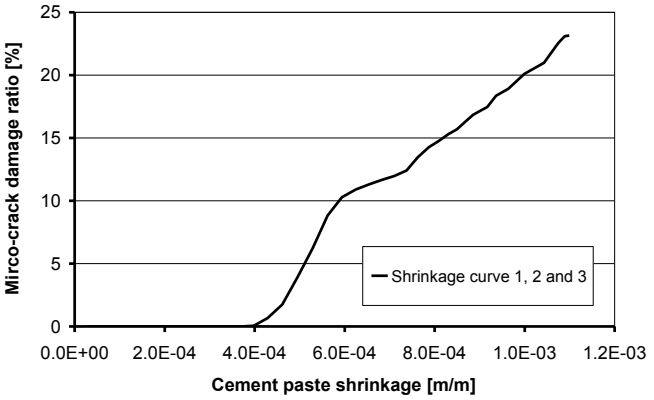

Figure 5.27 Microcrack damage ratios in specimen C075-CG without stress relaxation.

Further increase of the eigenstress is limited by failure of bond beams in the pre-peak stage up to a peak tensile stress of about 2.3 N/mm^2, which reached at a shrinkage strain of ≈ 530·10^{-6} m/m. When the maximum eigenstress of 2.3 N/mm^2 is reached the microcrack damage ratio D_{cm} = 3.9%. In the post-peak stage the eigenstress decreases due to the simultaneous failure of bond- and matrix-beam. Figure 5.27 shows the evolution of the damage ratio D_{cm} in the specimen. Also in this case the three curves coincide.

5.8.3 Evolution of stresses with relaxation

In the case with stress relaxation the stresses in the ascending branch of the stress curves, calculated with an activation energy U_0 = 12 kJ/mol, are slightly higher for the original strain curve 1 compared to the imposed strain curves 2 and 3 (Fig. 5.28).

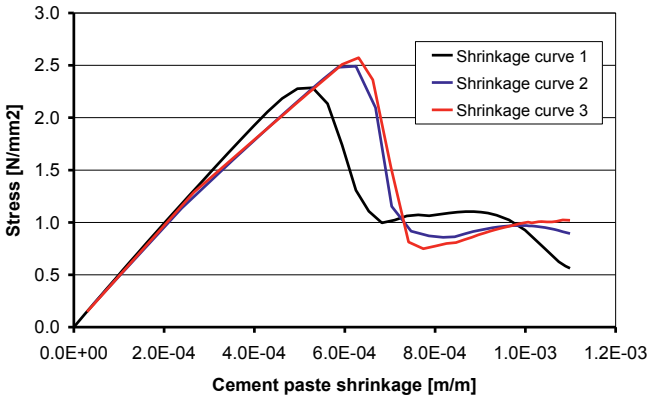

Figure 5.28 The *structural* eigenstress at macro-level ($\sigma_{se,,macro}$) in specimen C075-CG, with stress relaxation (activation energy U_0 = 12 kJ/mol).

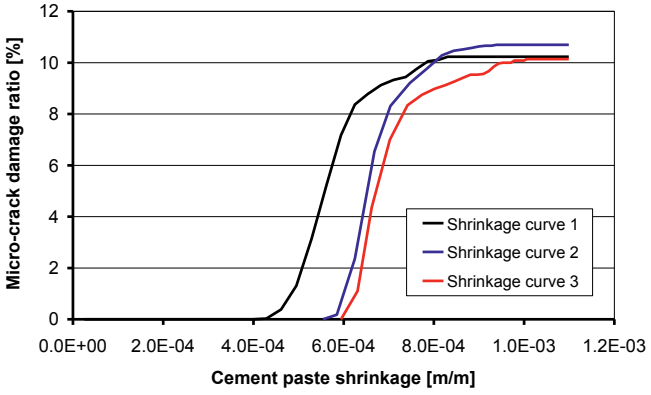

Figure 5.29 Microcrack damage ratios in specimen C075-CG with stress relaxation (activation energy U_0 = 12 kJ/mol).

The maximum stress in the specimen generated by the original shrinkage curve was about 2.3 N/mm^2 at an imposed strain of about $530 \cdot 10^{-6}$ m/m. The maximum stresses generated by the strain curves 2 and 3 are about 2.5 N/mm^2 at a strain of about $625 \cdot 10^{-6}$ m/m. The stresses in the ascending branch generated by the shrinkage curves 2 and 3 are lower compared to those generated by the original shrinkage curve 1. Obviously, there was more time available for relaxation to develop and to reduce the generated stresses. The occurrence of cracking was postponed.

Figure 5.29 shows the damage ratio D_{cm} calculated for the three imposed shrinkage curves. The delay of cracking in the samples simulated with the strain curves 2 and 3 compared with the cracking generated by the original shrinkage curve 1 is obvious. The intensity of microcracking, as indicated by the damage ratio, reaches a value a little higher than 10%.

5.9 Role of microcracking on concrete shrinkage

5.9.1 Potential role of microcracking on macroscale shrinkage

In the preceding sections the focus of the analyses was on the effect of the aggregate particles and aggregate content on the evolution of shrinkage-induced stresses and the intensity of microcracking. Both the restraining effects of the aggregate particles and the microcracking have an effect on the resulting concrete shrinkage. If microcracking occurs, the concrete shrinkage observed at macroscale will be less compared to an non-cracked specimen. This is shown schematically in Figure 5.30. In this section the influence of microcracking on the shrinkage of concrete will be analyzed in more detail.

The magnitude of concrete shrinkage depends on the concrete composition (aggregate volume fraction, stiffness of aggregate and cement paste) and on the magnitude of microcracking in the cement paste matrix. The effect of microcracking on the resulting shrinkage of the

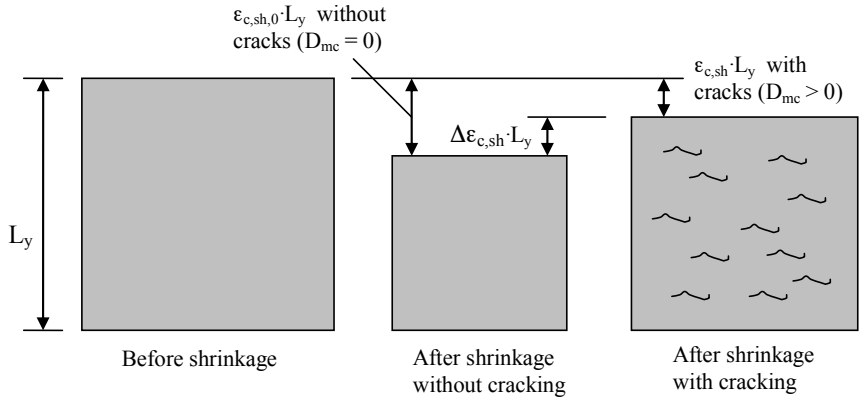

Figure 5.30 Schematic representation of the BLM (material restrained) with shrinkage deformation without microcracking ($D_{mc} = 0$) and with microcracking ($D_{mc} > 0$).

simulated concrete is analysed with the beam lattice model (BLM) for the situation of *material restraint*.

For the analyses a BLM specimen with a length L_y = 50.2 mm is used. With the mean value of shrinkage-induced vertical displacements (y-direction) of the nodes in the BLM at the horizontal edges at the bottom (Δy_{bottom}) and top side (Δy_{top}), the concrete shrinkage $\varepsilon_{c,sh}$ can be written as:

$$\varepsilon_{c,sh} = \frac{\Delta y_{top} - \Delta y_{bottom}}{L_y} \tag{5.4}$$

For the BLM analyses numerical specimens with continuous grading (CG) and nominal aggregate volume fractions of 0.75 m^2/m^2 (C075-CG), 0.60 m^2/m^2 (C060-CG) and 0.45 m^2/m^2 (C045-CG) are used. In these analyses the cement paste shrinkage as described in figure 5.6 (section 5.4.1) is used. The material parameters used in the analyses are summarized in Table 5.10.

For the analysis of the influence of the aggregate volume fraction (AVF) on concrete shrinkage, the shrinkage of concrete specimens is first calculated assuming that no microcracking occurs. To (numerically) prevent the occurrence of cracking the matrix tensile strength is set at a high fictitious value, i.e. $f_{m,fict.}$ = 50 MPa. For evaluating the effect of microcracking on shrinkage of concrete specimens the shrinkage strains after 1 year (8760 hrs) are compared.

Table 5.10 Material parameters of specimens C075-CG, C060-CG and C045-CG.

Specimen code	Aggregate volume fraction V_a [m^2/m^2]	Mix nr.	Without cracking	With cracking	Strength ratio	Stiffness cement paste and aggregate	
			$f_{m,fict}$ [MPa]	f_m [MPa]	f_b / f_m [-]	$E_m = E_b$ [GPa]	E_a [GPa]
C075-CG	0.75	1	50	5	0.75	7.8	70
C075-CG	0.75	2	50	5	0.75	15.1	70
C075-CG	0.75	3	50	5	0.75	23.2	70
C045-CG	0.45	4	50	5	0.75	15.1	70
C045-CG	0.45	5	50	5	0.75	15.1	35
C060-CG	0.60	6	50	5	0.75	15.1	70

- f_b/f_m = bond / matrix tensile strength ratio
- For the cases *without* microcracking a fictitious tensile strength is used: $f_{m,fict.}$ = 50 MPa.
- C075-CG: D_{max} = 14 mm; C060-CG: D_{max} = 13 mm; C045-CG: D_{max} = 12 mm;
- Relaxation with activation energy U_0 = 12 kJ/mol.

5.9.2 Shrinkage and stress predictions in microcrack-free specimens

The effect of aggregate volume fraction on shrinkage of an uncracked concrete specimen is presented in figure 5.31 for specimens C075-CG and C045-CG. For comparison the free

shrinkage of the cement paste is shown as well. In specimen C045-CG the shrinkage ratio 'concrete shrinkage/free cement paste shrinkage' ($\varepsilon_{c,sh}$ /$\varepsilon_{p,sh}$) = 0.57, while in the specimen C075-CG this ratio is 0.34 (ratio's after 8769 hrs, i.e. 1 year).

Figure 5.31 shows that a higher aggregate volume fraction results in lower visable / external shrinkage (Fig. 5.31a) and higher stresses (Fig. 5.31b) in the cement paste.

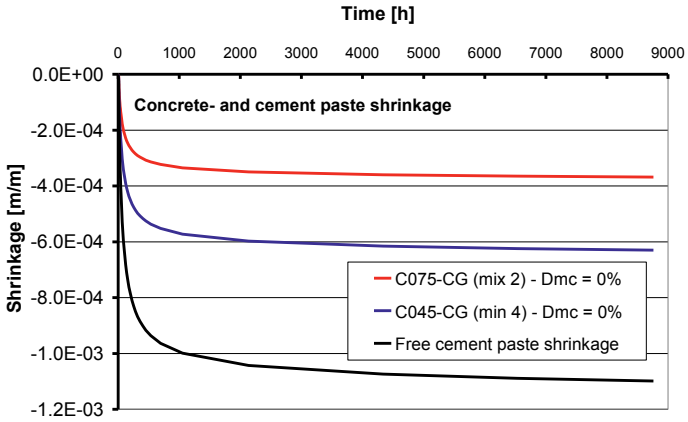

a. Shrinkage of concretes with different aggregate volume fraction.
Without relaxation and no microcracking (D_{mc} = 0%).

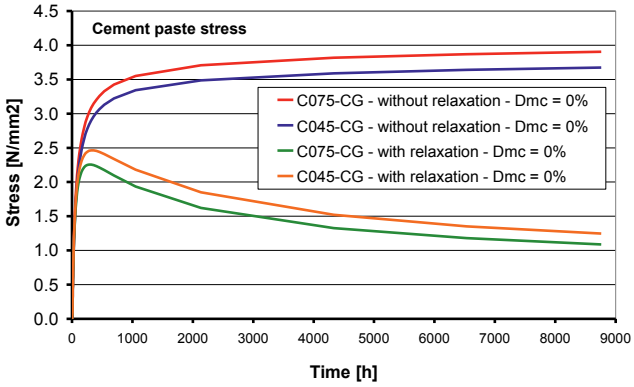

b. Stresses in cement paste of concrete with different aggregate volume fraction.
No microcracking. Stresses calculated with and without relaxation.

Figure 5.31 Calculated shrinkage and stresses in specimens C075-CG and C045-CG. No microcracking
a. Calculated shrinkage. No relaxation considered.
Maximum free cement paste shrinkage $\varepsilon_{p,sh} = 1.1 \cdot 10^{-3}$ m/m.
b. Calculated stresses, without and with relaxation of stresses (relaxation: U_0 = 12 kJ/mol).
Note: The calculated stress represents the mean value of all the stresses in the matrix- and bond beams in the BLM.

5.9.3 Effect of microcracking and relaxation on shrinkage of concrete specimens

With microcracking in the cement paste a part of the mobilised shrinkage energy is lost. This leads to a reduction of the externally visible concrete shrinkage compared to the shrinkage of a specimen without microcracking. Stress relaxation has a mitigating effect on microcracking, with the consequence that the concrete shrinkage increases.

Figure 5.32 shows the concrete shrinkage without and with microcracking of the specimens C075-CG and C045-CG. In specimen C075-CG the shrinkage ratio ($\varepsilon_{c,sh}/\varepsilon_{p,sh}$) after 1 year is 0.30 and 0.23 for, respectively, with and without relaxation. The shrinkage ratio after 1 year for C045-CG is 0.54 and 0.44 for, respectively, with and without relaxation.

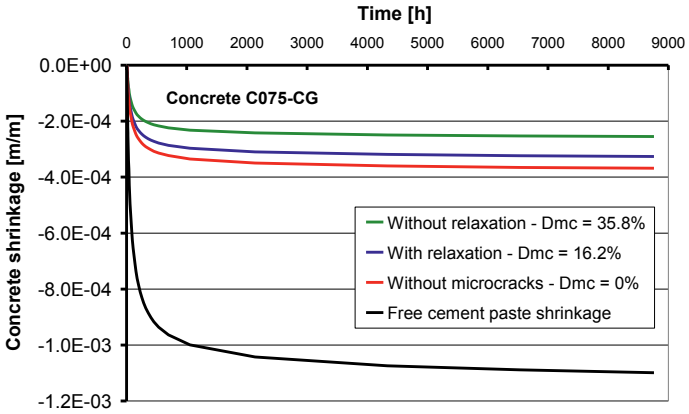

a. Concrete shrinkage in specimen C075-CG with Mix 2 (E_m = 15.1 GPa, E_a = 70 GPa).

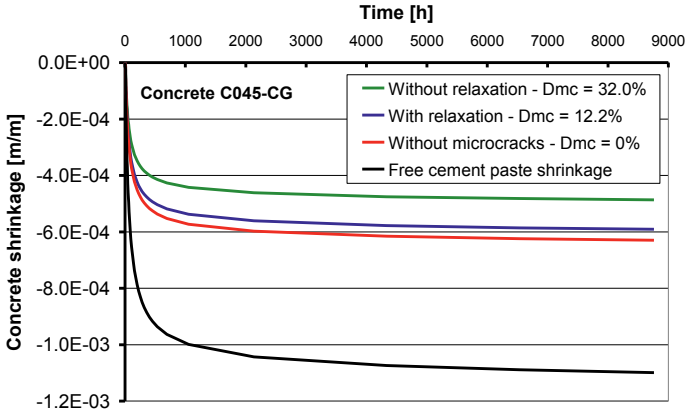

b. Concrete shrinkage in specimen C045-CG with Mix 4 (E_m = 15.1 GPa, E_a = 70 GPa).

Figure 5.32 Influence of microcracking on concrete shrinkage in specimens C075-CG (a) and specimen C045-CG (b). Maximal free cement paste shrinkage $\varepsilon_{p,sh} = 1.1 \cdot 10^{-3}$ m/m.

5.9.4 Effect of aggregate stiffness on concrete shrinkage

Beside the aggregate *volume fraction* also the aggregate *stiffness* affects the concrete shrinkage. The concrete shrinkage of specimen C045-CG is analysed, therefore, with aggregate stiffness values of 70 and 35 GPa (Table 5.10: Mix 4 and Mix 5). Calculations are performed with and without microcracking, whereas stress relaxation was not considered. Figure 5.33 shows the evolution of the concrete shrinkage under the different conditions.

In the case *without* microcracking the difference in aggregate stiffness results in a difference in concrete shrinkage after 1 year of $\approx 29 \cdot 10^{-6}$ m/m (see Fig. 5.33). With microcracks this difference is larger, viz. $\approx 36 \cdot 10^{-6}$ m/m.

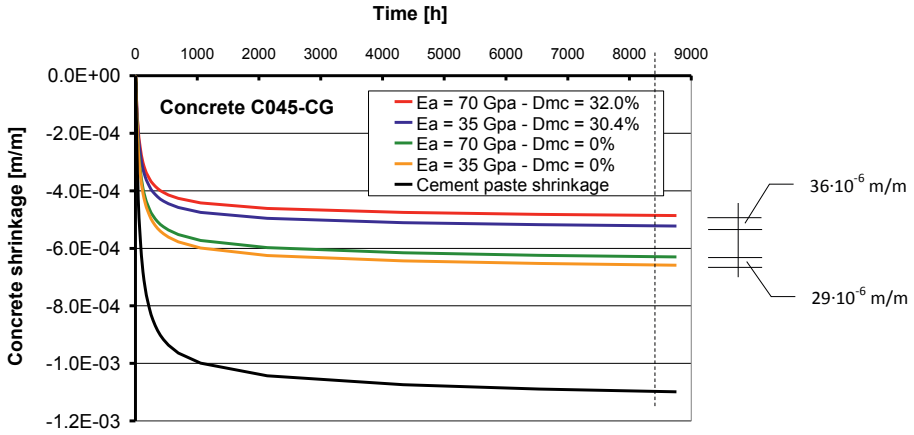

Figure 5.33 Concrete shrinkage in specimen C045-CG with aggregate E_a = 70 GPa and 35 GPa (Table 5.10, Mix 4 and Mix 5). Maximum free cement paste shrinkage $\varepsilon_{p,sh} = 1.1 \cdot 10^{-3}$ m/m.

5.9.5 Estimation of the role of microcracking on concrete shrinkage

The analyses in previous sections show that the aggregate volume fraction and microcracking affect the magnitude of concrete shrinkage. Moreover, the role of relaxation appears to be substantial as well. The effect of these three influencing factors on the shrinkage strains after 1 year (8760 hrs) was, therefore, calculated and compared for three concrete mixtures. The three mixtures were Mix 4, 6 and 2 of Table 5.10, with aggregate volume fractions 0.45, 0.60 and 0.75, respectively. The imposed shrinkage of the cement paste was the shrinkage curve given in figure 5.6. In Table 5.11 the calculated shrinkage strains after 1 year are given. The calculations were performed *without* allowing microcracking to occur, *with* microcracking and for microcracking *plus* relaxation.

The strain calculated without microcracking (column 4 of Table 5.11) is used as a reference. In the columns 5 and 7 the calculated shrinkage after 1 year is presented for the situations with microcracking and microcracking plus relaxation. The reduction of the shrinkage strains due to microcracking is shown in the columns 6 and 8.

Table 5.11 Shrinkage reduction due to microcracking in the specimens C075-CG, C060-CG and C045-CG with E_m = 15.1 GPa and E_a = 70 GPa. Cement paste shrinkage $\varepsilon_{p,sh} = 1.1 \cdot 10^{-3}$ m/m.

Specimen	Mix nr.	Aggregate volume fraction V_a [-]	Calculated shrinkage strain after 1 year (8760 hrs)				
			Without cracks	With cracks		With cracks and relaxation	
			$\varepsilon_{c,sh}$ [m/m]	$\varepsilon_{c,sh}$ [m/m]	%	$\varepsilon_{c,sh}$ [m/m]	%
C045-CG	4	0.45	$-630 \cdot 10^{-6}$	$-485 \cdot 10^{-6}$	22.8	$-590 \cdot 10^{-6}$	6.2
C060-CG	6	0.60	$-500 \cdot 10^{-6}$	$-370 \cdot 10^{-6}$	26.2	$-470 \cdot 10^{-6}$	6.3
C075-CG	2	0.75	$-370 \cdot 10^{-6}$	$-255 \cdot 10^{-6}$	30.8	$-325 \cdot 10^{-6}$	11.5

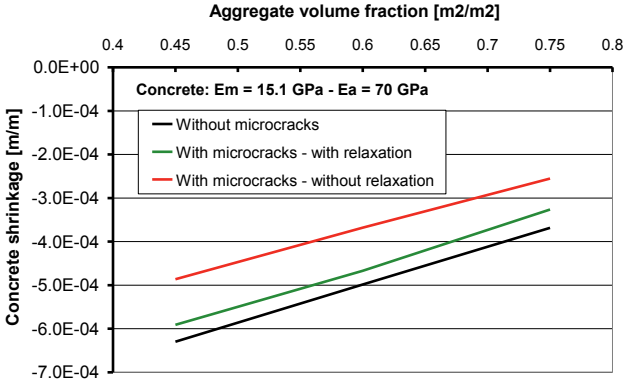

a. Concrete shrinkage as function of the aggregate volume fraction (AVF).

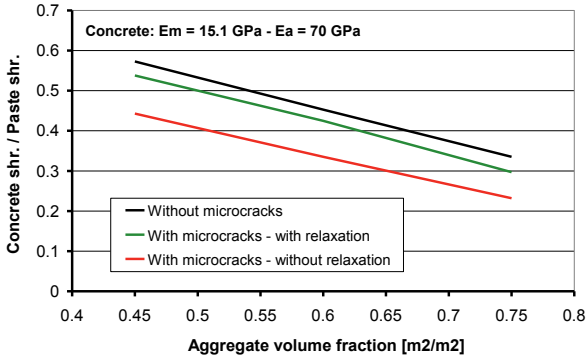

b. Concrete shrinkage ratio ($\varepsilon_{c,sh}$ /$\varepsilon_{p,sh}$) as function of the aggregate volume fraction (AVF).

Figure 5.34 Calculated concrete shrinkage as function of aggregate volume fraction. Calculations with and without microcracking and with and without relaxation.
a. concrete shrinkage as function of the AVF
b. shrinkage ratio as function of the AVF.

The values given in column 6 show that due to microcracking the shrinkage strain after 1 year is reduced by 20 to 30% when compared to specimens without cracks. Due to relaxation microcracking is postponed and shrinkage reduction is smaller, viz. between 6 and 12% of the shrinkage strain of uncracked specimens, depending on the aggregate volume fraction.

Figure 5.34 shows the influence of microcracking and relaxation on the calculated concrete shrinkage as function of the aggregate volume fraction of the specimens. The figure shows that the magnitude of concrete shrinkage is about linear when related to the aggregate volume fraction. The effect of microcracking and relaxation do not affect this linear correlation.

5.10 Discussion

The main objective of the numerical analyses presented in this chapter was to study the effect of relaxation on the magnitude of stresses caused by shrinkage of the cement paste and to investigate whether the effect of relaxation would be large enough to prevent the occurrence of (micro)cracking. The numerical analyses were performed with a lattice-type numerical model. The basic structure of this model, a Beam Lattice Model (BLM), was presented briefly in chapter 3. In that chapter it was also explained how the lattice model was made suitable for taking relaxation of stresses into account. All the numerical analyses described in this chapter were carried out with a 2D-version of the beam lattice model (2D-BLM).

The numerical 2D-simulations were carried out on small virtual concrete specimen with size L_x = 48 mm and L_y = 52 mm. Two kinematic boundary conditions were considered, viz. *full external restraint (structural restraint)*, simulating structural eigenstresses, and *aggregate or material restraint,* i.e. no external restraint of the specimen.

The concrete is modelled as a three-phase material: aggregate, cement paste matrix and an intermediate layer (ITZ). The tensile strength of the paste-aggregate interfacial zone was varied from 0.5 to 0.75 times the tensile strength of the bulk paste. Different values of the modulus of elasticity of the cement paste and the aggregates were considered.

Five types of specimens were considered. Differences concerned the size and distribution of the aggregate particles, the stiffness of the aggregate particles and the volume of the aggregate particles in the specimens (see Tables 5.1 and 5.2).

The majority of analyses were carried out with the same imposed shrinkage curve of the cement paste (see Fig. 5.6). The effect of the shape of the shrinkage curve, i.e. the rate of shrinkage, was analysed separately in section 5.8. The effect of microcracking on concrete shrinkage was analysed in section 5.9.

The intensity of (micro)cracking was indicated using a damage ratio D_{mc}, defined as the percentage of broken cement paste beams relative to the total number of paste beams.

Cement paste stiffness E_m - Full restraint (par. 5.5.1)

With increasing cement paste stiffness E_m the stiffness of the simulated 'paste only' specimen increased as well (Fig. 5.8). Because of the increased stiffness the stresses caused by the imposed shrinkage strains are higher and microcracking is initiated at a smaller imposed shrinkage. For the cement pastes with a high stiffness the effect of relaxation is noticeable, but not

enough to prevent the occurrence of cracking at the imposed shrinkage strain. For the cement paste with a relatively low stiffness, i.e. E_m = 7.8 GPa, relaxation of the stresses could prevent cracking to occur.

The effect of the cement paste stiffness remains in case aggregate particles are considered in the specimen. The stiffer the cement paste, the higher the stiffness of the specimen and the higher the damage ratio D_{mc} (Fig. 5.9a,b and 5.10a,b).

Due the microcracking the structural tensile stress of the composite, $\sigma_{se,macro}$, does not reach the tensile strength of the cement f_m, i.e. 5 MPa. In a specimen with one single aggregate particle the maximum tensile stress reached values between 2.9 and 4.6 MPa (Fig. 5.9a), whereas the maximum tensile stress in a continuous aggregate grading model reached a maximum tensile stress of no more than 2.4 to 3.3 MPa, depending on the stiffness of the cement paste (Fig. 5.10a).

After imposing the total shrinkage strain of $\varepsilon_{p,sh} = 1.1 \cdot 10^{-3}$ m/m, the residual structural eigenstresses, $\sigma_{se,macro}$, vary between 0.2 and 0.7 MPa, which is in the order of 4-14% of the cement paste tensile strength of 5 MPa.

Bond/matrix tensile strength ratio f_b/f_m - Full restraint (section 5.5.2)

The effect of matrix-aggregate bond strength on the performance of concrete under an imposed shrinkage strain was investigated for specimens with an aggregate volume fraction of 75% and 45%. Constant values for the stiffness of the cement paste and the aggregate particles were assumed. The numerical analyses showed a significant effect of the paste-aggregate bond strength on the maximum stress caused by the imposed shrinkage strain (Fig. 5.11a and 5.12a). In the specimens with an aggregate volume fraction of 75% and 45%, the maximum structural eigenstresses are more or less proportional to the bond strength: the higher the bond strength, the higher the structural eigenstresses (Fig. 5.11a and Fig. 5.12a).

Microcracking increases with a decreasing bond strength (Fig. 5.11b, 5.12b). The effect of relaxation on the development of stresses and microcracking is higher for a specimen with a higher bond strength. In such a specimen the structural eigenstresses are higher, which explains a higher effect of relaxation. A significant effect of relaxation on the damage ratio D_{mc} was observed (Fig. 5.11b and 5.12b). This effect was higher the stronger the paste-aggregate bond. A relaxation-induced reduction of the damage ratio, and thus less microcracking, implies that relaxation has a positive effect on the resistance against ingress of liquid substances into the specimens.

Aggregate stiffness E_a - Full restraint (section 5.5.3)

The effect of aggregate stiffness on the development of stresses and microcracking was analysed for a specimen with continuous grading of the aggregate and an aggregate volume fraction of 75% (C075-CG). The stiffness of the aggregates ranged from 35 to 120 MPa. Bond strength was constant at f_b = 3.75 MPa (= 0.75 f_m). For a specimen with a higher aggregate stiffness the shrinkage-induced structural eigenstresses increased somewhat faster, but the maximum stress reached was about 2.3 MPa in all the simulations (Fig. 5.13a).

In the post-peak stage there was a significant effect of relaxation. Relaxation appeared to have a mitigating effect on the damage ratio D_{mc}. From this observation it could be inferred that relaxation can have a substantial mitigating effect on the intensity of microcracking caused by imposed shrinkage strains.

Another effect of relaxation on the development of structural eigenstresses is the increase in stress at an increase of the shrinkage strain after the stress-strain curve reached a local minimum. In Fig. 5.13a this occurs for all the specimens, irrespective of the stiffness of the aggregate, at shrinkage strains larger than about $0.7 \cdot 10^{-3}$ m/m. Obviously stress relaxation in beams has delayed cracking, thus enabling the model to resist higher forces at higher imposed strains.

Particle size and particle size distribution – Full restraint (section 5.5.4)
Other parameters of the simulated specimens being the same, changes in the particle size and particle size distribution did not significantly change the shape of the shrinkage-induced stress-strain curves, as shown in figure 5.14a for specimens with an aggregate volume fraction of 8% and in figure 5.15a for an aggregate volume fraction of 60%. The crack patterns, however, differed considerably, as shown in the figures 5.14c and 5.15c. Due to relaxation the damage ratio was significantly reduced, particular at shrinkage strains greater than about $0.7 \cdot 10^{-3}$ m/m (Fig. 5.15b).

Stress relaxation – Full restraint (section 5.5.5)
The effect of relaxation on the development of shrinkage-induced structural eigenstresses and microcracking was analysed for specimens without aggregate and with aggregate (see Table 5.8).
In the matrix-specimen (without aggregate) cracking can be avoided with moderate stress relaxation (U_0 = 12 kJ/mol, see fig. 5.16). By adding a single particle (1∅16 mm: 0.08 m^2/m^2) stress relaxation can not prevent microcracking (Fig. 5.17).

In the cases with specimens with a multi particle and continuous aggregates grading, stress relaxation seems to have a limited effect on the shrinkage-induced peak stress (Fig. 5.18a). High relaxation caused a delay of the moment the peak stress was reached. The stresses at the end of the simulation period are almost the same and in the order of 5-10% of the cement paste tensile strength (f_m = 5 MPa).

Stress relaxation influences the number of microcracks to a great extent. Relaxation increases the strain at which microcracking starts and results in lower values of the damage ratio (Fig. 5.18b). This observation suggests that relaxation has a substantial contribution to the potential resistance of concrete against ingress of hazardous substances.

Stress distribution in arbitrary cross-section of concrete specimen (section 5.6)
Detailed analyses of the stress distribution in an arbitrary cross section were performed. At locations where peak tensile stresses were generated these stresses reached the tensile strength of the paste. The occurrence of microcracks caused a rigorous redistribution of the stresses. Once a beam of the lattice model cracks, the local equilibrium of forces has to be restored. Some adjacent beams may take over a part of the force of a broken beam, while at

the same time the forces in other beams may decrease and even change from tension into compression (Fig. 5.20e and 5.21e). The latter occurs when aggregate particles start to 'move' as result of a changing stress field in the paste. The analyses show that a great difference between the macro-scale stresses, i.e. structural eigenstresses, and the local stresses in the matrix can occur. This is typical for heterogeneous materials. For the specimen with a high bond strength (f_b = 0.75 f_m), figure 5.20e shows the stress distribution at an imposed shrinkage strain of $682 \cdot 10^{-6}$ m/m. At that strain the local tensile stress reaches values up to 2.4 MPa, whereas the average tensile stress at that shrinkage strain is 0.8 MPa (Fig. 5.20b). In the specimen with low bond strength (f_b = 0.25 f_m), figure 5.21e shows that at an imposed shrinkage strain of $1043 \cdot 10^{-6}$ m/m the local stresses in a cross-section range from -2.8 MPa to 2.2 MPa, whereas the structural eigenstress at this imposed shrinkage strain is 0.2 MPa. The possible discrepancy between stresses at structural level (macroscale) and microscale complicates the evaluation of the stress state in heterogeneous materials based on macrolevel considerations only.

Stress evolution in individual beams of the lattice model (section 5.7)
The stress evolution in individual lattice beams was further studied in section 5.7. The effect of cracking of adjacent beams on the stresses in the monitored beams was evaluated. A redistribution of forces after the occurrence of local cracking implies that local stresses continuously change. This redistribution of stresses is considered to play an important role in the long-term performance of the material.

Influence of the shape of the shrinkage curve, i.e. strain rate, on eigenstresses (section 5.8)
The influence of the shape of the shrinkage curve on eigenstresses was analyzed for three shrinkage curves (Fig. 5.25). The shrinkage curves had in common that the final shrinkage value was the same. The curves, however, had different initial strain rate values.

In the case without stress relaxation the shape of the shrinkage curve does not have influence on the evolution of the eigenstresses in terms of stress versus the magnitude of the imposed strain. When stress relaxation is taken into account the evolution of eigenstresses can be described by using three different stages. In the initial stage without microcracking the increase of eigenstress over time is proportional to the magnitude of the shrinkage strain rate. The start of the microcracking stage is reached earlier in case of a higher initial strain rate. The consequence of this is that with increasing initial strain rates the maximum value of the eigenstress remains lower. This is caused by the earlier start of failure of beams that are then no longer available for load transfer in a later stage. The same holds for the residual value of the eigenstress.

Role of microcracking on concrete shrinkage (section 5.9)
The role of microcracking on concrete shrinkage was studied with a BLM with 'material restraint' boundary conditions. The analyses were carried out with specimens with different aggregate volume fractions (AVF). In the case without microcracking and without stress relaxation, the concrete shrinkage is proportional to the reciprocal value of the AVF (Fig. 5.31a). When the occurrence of microcracking is prevented , the tensile eigenstresses in the cement paste matrix increase with increasing AVF in cases with and without stress relaxation.

In cases with microcracking (without relaxation) it was found that microcracking reduced the concrete shrinkage proportional to the AVF. In cases with microcracking and stress relaxation, the reductions in concrete shrinkage were lower since the magnitude of microcracking is reduced by relaxation. Aggregate stiffness has only little influence on the magnitude of microcracking. It was found that increasing the aggregate stiffness by a factor 2 resulted in a 7% reduction of concrete shrinkage. The reduction is even less in the cases without microcracking (Fig. 5.33). The final conclusion is that the AVF affects concrete shrinkage substatntially . Results of the calculations showed that reductions in concrete shrinkage are about 6 to 12% when stress relaxation and microcracking are taken into account compared to (hypothetically) uncracked concrete (Table 5.11).

5.11 Conclusions and outlook

The numerical tests with the 2D-BLM were carried out with the focus on the magnitude of residual tensile eigenstresses and microcracking in the cement paste of concrete specimen. The cover zone of a concrete element (slab, wall) is modeled with a two-dimensional beam lattice model (BLM). The imposed shrinkage simulates a possible shrinkage evolution under drying conditions in the concrete cover zone. The shrinkage of cement paste is assigned to the paste beams (matrix-beams and bond-beams) of the BLM. The strength and stiffness parameters of the modelled concrete mixture are taken into account with constant values.

The main objective of the numerical stress analyses was to quantify the effect of relaxation of the cement paste on the magnitude of the residual eigenstresses. The numerical analyses revealed that, for the mixtures and boundary conditions considered in this chapter, relaxation certainly has a stress mitigating effect, but not to an extent that microcracking can be prevented. Due to relaxation microcracking is postponed, but not prevented. Less intensive microcracking is beneficial in view of transport properties, since it reduces the probability of the formation of an interconnected internal network of microcracks. The concrete remains denser and less permeable.

Since, according to the numerical simulations, microcracking cannot be prevented, it remains to be checked whether the intensity of the simulated microcracking is in agreement with observations. A preliminary step to validate the numerical predictions with the 2D-BLM is presented in the next chapter.

Chapter 6

6. Eigenstress-induced microcracking and transport properties

This chapter deals with the question whether the calculation procedure used in this thesis for concrete microcracking is sufficiently accurate to quantify the effect of microcracking on the transport properties of concrete, i.e. chloride penetration in concrete exposed to thermal and hygral cycles. Results of chloride penetration tests, of which the chloride ingress is proposed to be enhanced by microcracking, are analysed. Chloride profiles are calculated with an apparent chloride diffusion coefficient, or chloride penetration coefficient, in which the influence of microcracking is incorporated. The predicted effect of microcracking on transport properties is compared with transport properties inferred from measured large-scale chloride penetration tests.

6.1 Introduction

In chapter 5 the influence of strength and stiffness of cement paste and aggregate particles on (residual) eigenstresses and microcracking in concrete exposed to imposed shrinkage strains of cement paste were analysed. The main purpose of the analyses was to quantify the effect of relaxation on the magnitude of stresses caused by imposed shrinkage strains and to see whether relaxation could reduce or even prevent shrinkage-induced microcracking. The general conclusion from the analyses was that for the adopted imposed shrinkage strains microcracking was almost unavoidable. So far, however, the numerical results were not validated. Unfortunately, experimental data for validating numerical predictions of microcracking caused by imposed deformations is scarce.

In the absence of suitable experimental data for validating the results of the numerical analyses presented in Chapter 5, an alternative way was adopted for validating the microcracking predictions. It is believed that microcracking increases the permeability of concrete and enhances the rate of penetration of chloride ions into concrete. The influence of eigenstresses and eigenstress-induced microcracking on chloride penetration has been examined experimentally in a large-scale test set-up by Taheri-Motlagh (1998). His test setup was later on used to investigate the chloride penetration in lightweight aggregate concrete (LWAC) and normal weight concrete (NWC) (Van Breugel 2000). In these large-scale chloride penetration tests the top-side of a large concrete beam was exposed to thermal and hygral cycles while chloride containing water was poured on the top of the beam. The thermal and hygral loads were supposed to be large enough to cause (micro-)cracking in the top layer of the concrete beam, which cracks would then promote the penetration of chloride ions into the concrete.

In this chapter the relevant details of the test set-up will presented as well as the main test results. The beam lattice model will be used to simulate the performance of the top layer of

the beam under the imposed strains. It will be checked whether the observed effect of microcracking on the chloride penetration matches with the numerically predicted degree of damage caused by the imposed deformations.

6.2 Large-scale chloride penetration tests

6.2.1 Background and principle of the experiment

Chloride-induced rebar corrosion is one of the most frequent reasons for deterioration of concrete structures. Service life predictions, therefore, often focus on predicting the rate of chloride penetration. Although the ingress of chloride ions is determined by several mechanisms, chloride transport is often considered as being a diffusion process. The process is described with Fick's second law, which operates with a time-dependent diffusion coefficient D(t), which is usually determined experimentally on uncracked specimens. In practice, however, concrete structures are exposed to thermal and hygral strains, large enough to cause microcracking in the surface zone of the concrete. Microcracks may increase the rate of ingress of chloride ions into the concrete. A prediction of chloride penetration with a diffusion coefficient derived from a standard lab-test will then result in an underestimation of the actual rate of chloride penetration and an overestimation of the service life of the concrete structure.

With the goal to quantify the effects of temperature and shrinkage-induced microcracking on the rate of chloride transport in concrete structures, Taheri-Motlagh (1998) developed a large-scale test. The principle of the experiment is shown in figure 6.1. A large concrete beam, $6.00 \times 0.75 \times 0.40$ m^3, is at the top exposed to thermal and hygral cycles. Under these cycles the top layer of the beam expands and/or shrinks, while the bottom part of the beam restraints the imposed strains. This is illustrated schematically in figure 6.2. In this figure a thermal load ΔT is shown, subdivided in a mean temperature, a temperature differential and eigen-temperatures. The mean temperature causes an axial deformation of the beam. Assuming that the beam can deform freely in axial direction, the mean temperature will not generate stresses. Assuming further that bending is prevented to occur by the dead weight of the

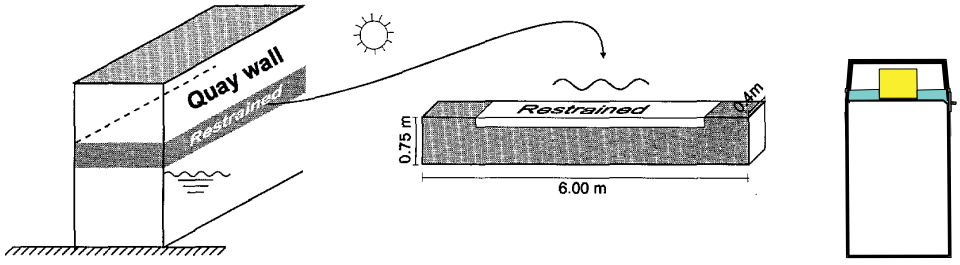

Figure 6.1 Set-up of large-scale experiment. A concrete beam (right) is exposed to thermal and hygral loads, simulating the exposure condition of a marine concrete structure (after Taheri-Motlag, 1998)

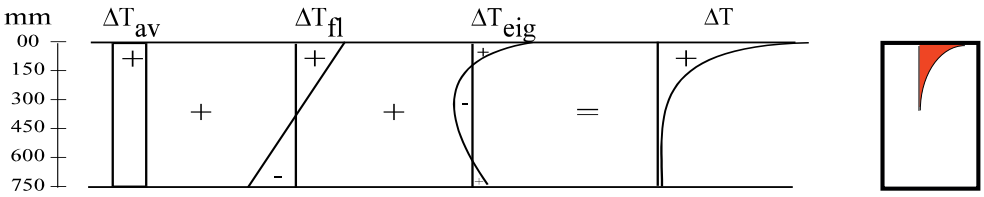

Figure 6.2 Imposed temperature distribution in the beam (right) and its components ΔT_{av} (mean temperature) ΔT_{fl} (temperature differential) and ΔT_{eig} (eigen temperatures)

beam, the temperature differential and eigen-temperatures are the stress-generating components of the thermal load. Similarly a moisture profile caused by drying of the beam at the top surface can be subdivided in three components. Only the shrinkage differential and the shrinkage eigenstrain will generate stresses.

An overview of the test set-up used by Taheri-Motlagh is shown in figure 6.3. Three beams are shown, of which two are covered with a thermal insulation and one (in front) serves as a reference beam that is subjected to alternating drying and wetting only.

Figure 6.3 View of the test set-up with the thermal isolated beams 1 and 2 and the control-beam 3 in the front, used only for alternate wetting and drying (AWD) (Taheri-Motlagh 1998, Van Breugel 2000).

6.2.2 Test parameters

6.2.2.1 Degree of restraint

For the determination of the effect of restraint on the degree of microcracking and transport properties special procedures were defined for creating conditions of *material* restraint and *structural* restraint.

Material restraint was obtained by pre-drilling cores, as schematically shown in Fig. 6.4. After pre-drilling the cores were left in position. The annular space between the core and the surrounding concrete was sealed with an elastic material. In this way boundary conditions were created under which the specimens could deform freely under imposed thermal and hygral cycles. Apart from the pre-drilled cores, the top layer of the beam experiences full

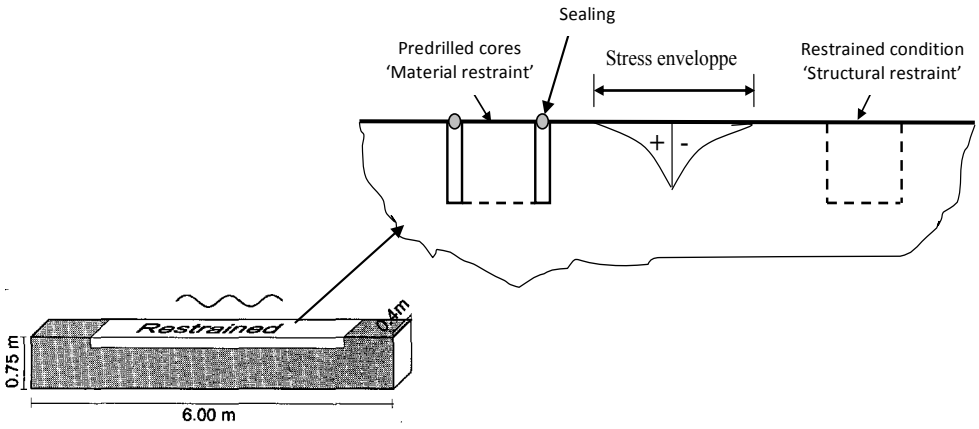

Figure 6.4 Top surface of the test beams with the unrestrained pre-drilled specimens and the restrained specimens.

restraint, i.e. structural restraint. By comparing the chloride profiles in unrestrained and restrained cores, the effect of microcracking on chloride penetration can be determined.

6.2.2.2 Effect of aggregate stiffness

Large-scale tests were performed on normal strength concrete made with *dense aggregate* (Normal Weight Concrete, NWC) and with *lightweight aggregate,* i.c. Liapor and Lytag (Lightweight Aggregate Concrete, LWAC). (Mixtures are defined in section 6.4.2) The effect of the stiffness of dense aggregate and lightweight aggregate particles on the materials restraint was reported to be significant (Van Breugel 2000; see section 6.2.4). Since the stiffness of aggregate particles is a parameter in the numerical simulation model, the published results were expected to provide suitable validation data for the numerical simulations. Figure 6.5 shows how the concretes to be tested were cast as top layers on the large concrete beam. The bottom part of the beam provides the (structural) restraint of the top layer.

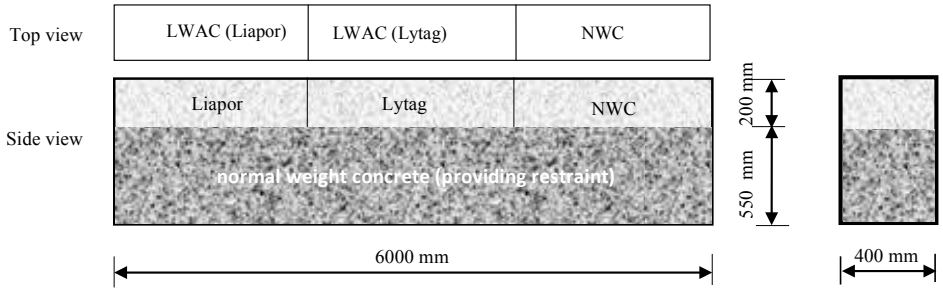

Figure 6.5 Top and side view of test beams (after Van Breugel 2000)

6.2.3 Curing and exposure conditions

6.2.3.1 Curing

After casting the beams were covered with plastic sheets to avoid plastic shrinkage and possible early microcracking. Average curing temperature was about 20°C. These conditions were maintained until the moment of exposing the top of the beam to hygral and thermal cycles. It was considered plausible by Taheri-Motlagh that under these curing conditions no microcracking had taken place prior to exposing the concrete to thermal and hygral cycles.

6.2.3.2 Exposure conditions

After the curing period the concrete beams were exposed at the top to alternating drying-wetting cycles and thermal cycles. One exposure cycle is shown in figure 6.6. A cycle consists of three thermal cycles over a period of 42 hours, followed by a wetting period of 6 hours. Wetting was done with water with a chloride content of 5% by weight.

One of the beams was exposed to drying-wetting cycles only. During the drying period this beam was exposed to the temperature and RH of the laboratory, i.e. about 20°C and RH between 40 and 60%. The experiment lasted 6 months. In this period 87 "complete exposure cycles" were applied in the exposure test.

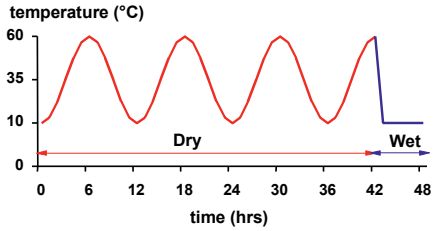

Figure 6.6 One complete 48 h exposure cycle applied to the top of the beams (Beams Fig. 6.5).

6.2.4 Measured effect of restraint conditions of chloride profiles

The chloride concentration at different depths in the concrete was measured by chemical analysis of cores drilled from the top of the beam. The chloride profiles in the "unrestrained cores" and in the "restrained beam section" were measured after 1 month and 6 months of exposure. Figure 6.7 shows a typical example of the chloride profiles measured in the normal weight concrete (NWC) and lightweight aggregate concrete (LWAC-Lytag) after 1 month exposure. The profiles convincingly show the effect of restraint: the ingress of chloride ions in a (structural) restrained specimen is larger than in unrestrained specimens (material restraint only). Microcracking due to structural restraint is assumed to be the reason for this effect.

It is noted that the ingress of chloride is not only promoted by the presence of microcracks, but also by the temperature itself and by the cyclic character of the exposure condictions. In this study, however, only the effect of microcracking on transport properties is considered.

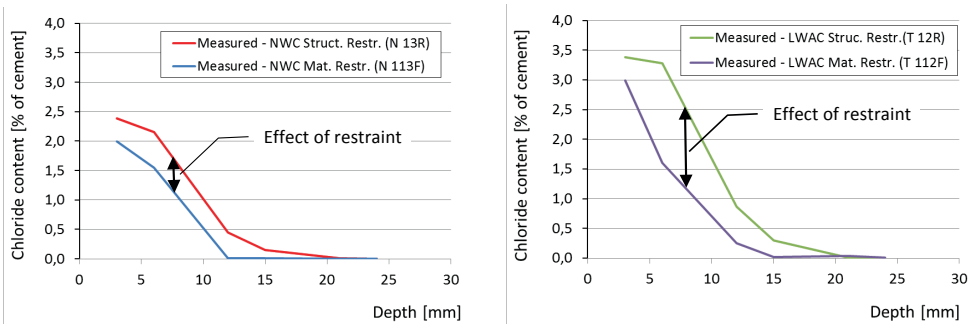

Figure 6.7 Measured chloride profiles for NWC and LWAC (Lytag) after 1 month under structural restraint and material restraint ('free') conditions (Van Breugel 2000).

This will complicate the comparison of the simulations results with the experimental findings. It is conceivable that a comparison of trends is the best we can get of this validation study.

6.3 Chloride penetration in concrete

Even though it is plausible that microcracking promotes the ingress of chloride ions in concrete, little information is available about quantification of the effect of microcracking on the transport properties. A complicating factor is the experimental determination of the degree of microcracking. The ultrasonic pulse velocity technique has been shown valuable for detecting cracking in concrete (Bungey et al., 1996). Since the pulse cannot travel through air, the presence of cracks on the wave path increases the path length and increases the transit time of the wave pulse. The effect of the intensity of microcracking on transport properties has been studied by Wang et al., (2016). Wang's approach will be briefly outlined in the following section and is leading for a proposed method to correlate the transport properties to the damage ratio D_{mc} defined in section 5.4.3.

6.3.1 Chloride transport in crack-free concrete

The chloride penetration in uncracked concrete is often calculated with the one-dimensional solution of Fick's second law of diffusion. For the chloride concentration at depth x in the concrete at time t it holds (Crank 1975):

$$C(x,t) = C_s - (C_s - C_i)\mathrm{erf}\left(\frac{x}{2\sqrt{D_a.t}}\right) \tag{6.1}$$

in which C_s and C_i are the chloride concentrations [kg/m^3] at the surface of the concrete and the initial chloride content in the concrete, respectively. The term D_a [m^2/h] is the apparent diffusion coefficient, which is often written as a function of time (Maage et al., 1996), viz.:

$$D_a(t) = D_{RCM,0}\left(\frac{t_0}{t}\right)^n \tag{6.2}$$

in which $D_{RCM,0}$ is the diffusion (i.e. migration) coefficient determined in the Rapid Chloride Migration test, executed that time t_0 on uncracked concrete. The factor n is an experimentally obtained ageing factor. With elapse of time the apparent diffusion coefficient *decreases*. This decrease is assumed to be caused by densification of the microstructure over time.

6.3.2 Chloride penetration in concrete specimen loaded in compression

Wang et al., (2016) studied the chloride penetration in concrete specimens, 100 mm in diameter and 80 mm thick, in which microcracking was created by compressive loading. The internal damage caused by the compressive load was determined by measuring the ultrasonic pulse velocity (UPV) prior and after application of the load. From these measurements the damage degree D_{upv} was defined as:

$$D_{UPV} = \frac{v_0 - v}{v_0} = \frac{\Delta v}{v_0} \tag{6.3}$$

in which v_0 and v are the pulse velocity before and after loading of the specimen, respectively. The chloride transport through the specimens was tested in accordance with the NT BUILD 492 test procedure (Nordtest –NT BUILD 492). The tests were performed on non-loaded and loaded concrete specimen, resulting in chloride migration coefficients $D_{RCM,0}$ and $D_{RCM,load}$. The increase of chloride migration due the microcracking was described with a normalised migration coefficient $D_{RCM,n} = D_{RCM,load}/D_{RCM,0}$. Figure 6.8 shows the increase of chloride penetration, expressed with the normalised migration coefficient $D_{RCM,n}$, as function of the UPV damage degree D_{upv}. This relationship was based on results from tests on

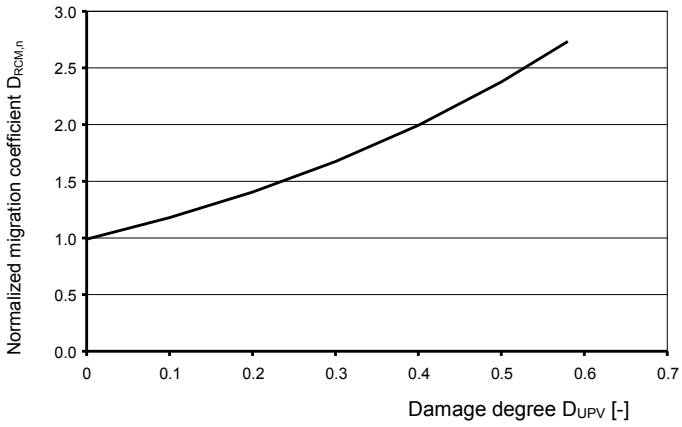

Figure 6.8 Relation between the normalised chloride migration coefficient $D_{RCM,n}$ and the UPV damage degree D_{upv} (Wang et al., 2016).

concretes with different binders and w/b ratios 0.45 and 0.65. For the correlation between the normalised migration coefficient $D_{RCM,n}$ and the UPV damage degree D_{upv}, Wang found an exponential relationship (Wang et al., 2016):

$$D_{RCM,n} = \frac{D_{RCM,load}}{D_{RCM,0}} = 0.99\, e^{1.75\, D_{upv}} \tag{6.4}$$

It is now assumed that there is a strong (linear) correlation between the damage degree D_{upv} given with eq. (6.3) and the calculated damage degree D_{mc} (see section 5.4.3):

$$D_{mc} = \frac{\text{number of broken cement paste beams}}{\text{total number of cement paste beams}} = \frac{N_0 - N}{N_0} = \frac{\Delta N}{N_0} \tag{6.5}$$

In eq. (6.3) the term Δv indicates the degree of damage, while in eq. (6.5) the degree of damage is indicated with the term ΔN. Based on this assumed correlation between D_{upv} and D_{mc}, eq. (6.4) could be replaced by a similar one, viz.:

$$\frac{D_{RCM,load}}{D_{RCM,0}} = 0.99\, e^{1.75\, D_{mc}} \approx e^{1.75\, D_{mc}} \tag{6.6}$$

or:

$$D_{RCM,load} = D_{RCM,0}\, 0.99\, e^{1.75\, D_{mc}} \approx D_{RCM,0}\, e^{1.75\, D_{mc}} \tag{6.7}$$

Note that $D_{RCM,load}$ has to be considered as an *apparent* diffusion coefficient. It stands for a term that determines the rate at which chloride ions penetrate into the concrete, irrespective of the mechanism responsible for this transport. Due to microcracking the diffusion coefficient $D_{RCM,load}$ will *increase* with time (see also Fig. 6.8). The apparent diffusion efficient $D_a(t)$ given with eq. (6.2) is supposed to *decrease* with time. To avoid confusion the terms $D_{RCM,load}$ and $D_a(t)$ will be considered in this chapter.

6.4 Comparison of predicted and measured of chloride penetration

6.4.1 Set-up of numerical simulation program

The imposed hygral and thermal strains will be largest at the top surface of the beam and decrease with increasing depth. For simulating the decreasing effect of imposed strains with increasing depth, numerical simulations with the BLM will be carried out at several depths. below the concrete surface, as illustrated in figure 6.9. The top layer of the concrete is subdivided in 6 layers for which numerical analyses of stresses and microcracking will be performed. The analyses will be performed for the boundary conditions full restraint and material restraint, as illustrated earlier in figure 5.3.

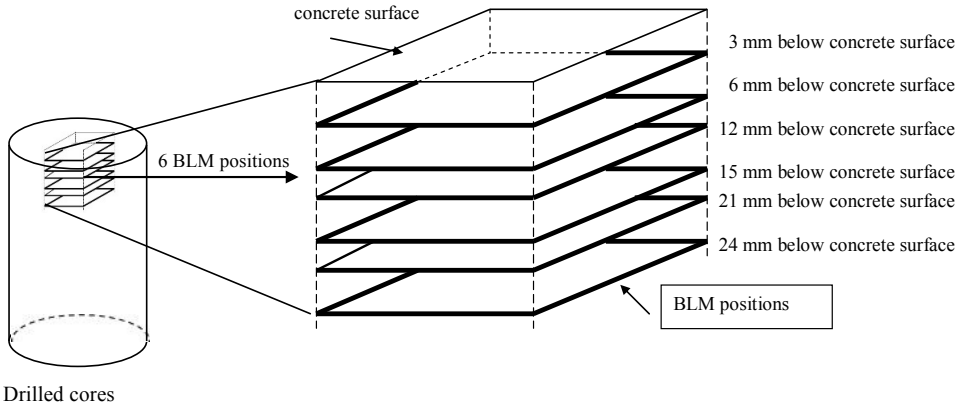

Figure 6.9 Position of beam lattices in concrete cores parallel with the concrete surface.

6.4.2 Concrete mixtures and material properties

The analyses of stresses and microcracking in the top layer of the beam will be performed for two mixtures, i.e. normal weight concrete (NWC) and lightweight aggregate concrete (LWAC). The concretes were made with ordinary Portland cement CEM I 32.5 N. In the NWC natural sand (0 – 4 mm) was used with 'normal' density aggregate (river gravel, 4 – 16 mm). In the LWAC natural sand (0 – 4 mm) was used with Lytag as lightweight aggregate in the fraction 4 – 8 mm. The concrete mix compositions and physical properties are given in Table 6.1. The aggregate volume fraction V_a of the mixtures is 0.70 [-]. A continuous aggregate grading is used.

Table 6.1 Composition and physical properties of concrete mixes at 28-days (Van Breugel 2000)

Code	Composition	w/b-ratio	Cement [kg/m^3]	Silica fume [kg/m^3]	$f_{cm,cube}$ [MPa]	$f_{ctm,cube}$ [MPa]	E_c [MPa]
NWC	PC + 4.7% SF	0.45	361	17	62.5	3.9	34500
LWAC	PC + 4.7% SF	0.45	361	17	61.2	4.3	26803

$f_{cm,cube}$ = mean compressive strength of 150 mm cubes; $f_{ctm,cube}$ = mean tensile splitting strength of 150 mm cubes;
E_c = modulus of elasticity of 100 x 100 x 400 mm^3 prisms

Values of material properties, like E-moduli of aggregate and cement paste and tensile strength of the cement paste, have been determined by back-calculation from assumed reasonable values of the mechanical properties of the concrete. For the aggregate stiffness 70 GPa is used for NWC. Equal stiffness of the cement paste is assumed in NWC and LWAC. With the model of Counto (1964) the stiffnesses of the cement paste and the aggregate in the LWAC are calculated from the measured concrete stiffness E_c (Table 6.1). The calculated values are presented in Table 6.2. The material parameters used in the analyses are summarized in Table 6.3.

Table 6.2 Cement paste stiffness E_p calculated with the model of Counto (1964).

Concrete type	Concrete E_c [MPa]	Aggregate E_a [MPa]	Aggregate volume fraction V_a [m^3/m^3]	Cement paste E_p [MPa]
NWC	34500	70000	0.70	10800
LWAC (Lytag)	26803	42000	0.70	10800

Table 6.3 Material parameters for numerical analyses with the 2D-BLM model.

Specimen code	Aggregate volume fraction V_a [m^2/m^2]	Material parameters				
		f_m [MPa]	f_b / f_m [-]	$E_m = E_b = E_p$ [GPa]	E_a [GPa]	Activation energy [kJ/mol]
NWC	0.70	7.5	0.75	10.8	70	12
LWAC (Lytag)	0.70	7.5	0.75	10.8	42	12

f_b/f_m = bond / matrix tensile strength ratio

6.4.3 Imposed strains

6.4.3.1 Drying shrinkage

The imposed drying shrinkage of the cement paste matrix is assumed to be a linear function of the relative humidity of the cement paste (Wittmann 1977):

$$\Delta\varepsilon_{p,ds} = \alpha_{ds}\Delta h \tag{6.8}$$

with: $\Delta\varepsilon_{p,ds}$ [m/m] increase of cement paste drying shrinkage, α_{ds} [m/m] the coefficient of linear drying shrinkage and Δh the decrease of relative humidity in the cement paste.

In the large-scale beam experiments the drying period is 42 hours. During this period only the top layer of the beam experiences drying. The moisture profiles are calculated up to a depth of 75 mm with a (one-dimensional) second order partial differential equation (Sadouki et al., 2000):

$$\frac{\partial h_p}{\partial t} = D_h \frac{\partial^2 h_p}{\partial x^2} \tag{6.9}$$

in which h_p [-] is the relative humidity in the cement paste at depth x [m] from the concrete surface at time t [h]. D_h is the moisture diffusion coefficient for cement paste [m^2/h]. During the drying period the ambient temperature is assumed to be constant at T = 20°C and the relative humidity RH = 50%.

Figure 6.10 shows the evolution of the calculated RH-profiles over the depth of the concrete. From these RH-curves, shrinkage curves are determined with eq. (6.8) for a coefficient of linear drying shrinkage α_{ds} = 0.01 m/m (Idiart et al., 2010). The shrinkage profiles are presented in figure 6.11.

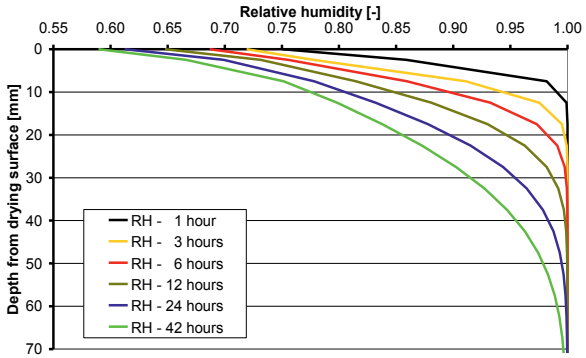

Figure 6.10 Calculated RH-profiles in concrete under drying conditions. Drying period 42 hrs.

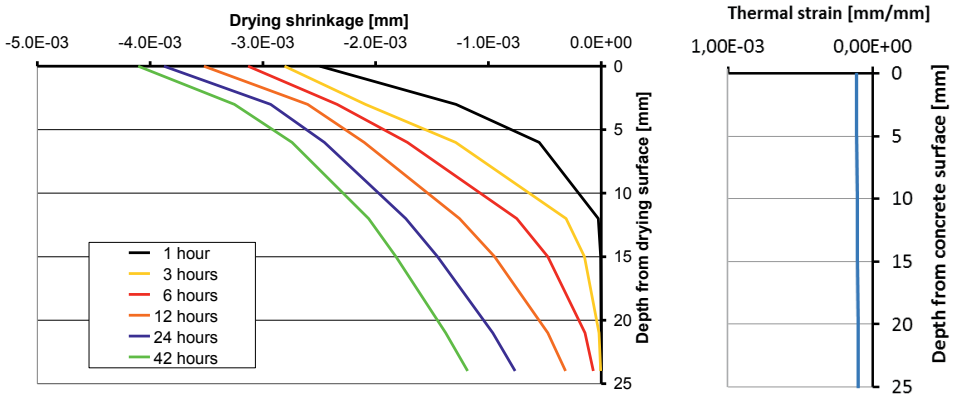

a. Strains due to drying

b. Thermal strain

Figure 6.11 Calculated strain profiles in the top 25 mm of the concrete beam

a. Drying shrinkage during period of 42 hrs. Calculations with eq. (6.8) for RH-values presented in figure 6.10.

b. Temperature-induced strain, inferred from Taheri-Molagh's thesis (1998).

6.4.3.2 Temperature-induced strain

In the experiments not only the strains caused by drying, but also temperature-induced strains are generated. For short periods, directly after applying water on top of the beams, temperature-induced shrinkage strains and associated thermal tensile stresses have been calculated (Taheri-Motlagh 1998). The maximum thermal shrinkage strains in the top 25 mm of the beam are presented in figure 6.11b. It is clear that the strain caused by drying shrinkage (Fig. 6.11a) is much larger than the temperature-induced strains. Moreover, the temperature gradient in the top layer of the beam was found to be less steep than the moisture gradient. Hence, the gradient of the temperature-induced strain is also much smaller than that of the moisture-induced strain, even hardly noticeable on the scale presented in figure 6.11b.

It is noted that in the case of material restraint the imposed thermal strains will not cause stresses, provided that the coefficients of thermal expansion of the cement paste and the aggregate particles are equal. This condition is assumed to be satisfied. Hence, only in the case of structural restraint the imposed thermal strains have to be taken into account.

The calculated strains, presented in figure 6.11, are the input for the numerical analyses of shrinkage induced stresses and microcracking with the BLM. As discussed in section 6.4.1, the BLM-calculations will be performed at six levels below the concrete top surface.

6.5 Numerical simulations with Beam Lattice Model

6.5.1 Microcracking and apparent diffusion coefficient $D_{RCM,load}$

Simulations of microcracking with the BLM are performed for the boundary conditions 'structural restraint' and 'material restraint'. In the stress calculations relaxation was taken into account (activation energy U_0 = 12 kJ/mol). The microcracking after 42 hours drying shrinkage in different layers (6 to 24 mm) is presented in figure 6.12 for the mixtures NWC and LWAC, for both structural restraint and material restraint (free). For each layer the microcrack damage ratio D_{mc} is calculated. Drying shrinkage and cracking are highest in the top layer. The results are in line with those of Wu et al., (2015).

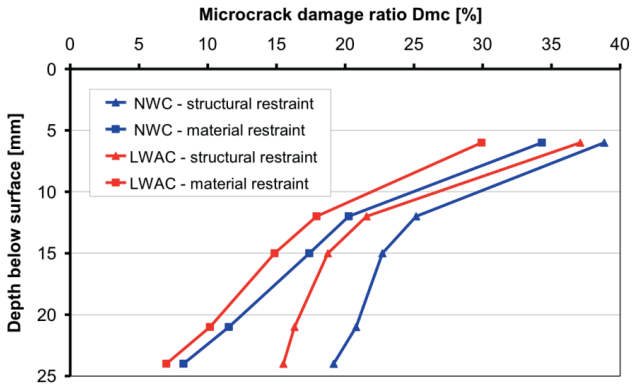

Figure 6.12 Calculated shrinkage-induced microcrack damage ratio D_{mc} of NWC and LWAC specimens after 42 hrs drying (material restraint) and drying plus temperature strain (structural restraint). Stress relaxation is taken into account with U_0 = 12 kJ/mol.

Figure 6.12 shows that at the concrete surface the microcrack damage ratio D_{mc} of the normal weight concrete increases from 34% to 39% for material restraint and structural restraint, respectively. For lightweight aggregate concrete these numbers are 30% and 37%, respectively. At a depth of 24 mm the D_{mc} of the normal weight concrete increases from 8%

Table 6.4 Apparent diffusion coefficient $D_{RCM,load}$ (eq. 6.7) as a function of the calculated damage ratio D_{mc} at depths of 6 mm and 24 mm below the concrete surface. D_{mc}-values calculated after 42 hrs. drying.

Concrete	6 mm depth					24 mm depth				
	D_{mc} [--]		$D_{RCM,load}$ (eq. 6.7) [$*D_{RCM,0}$]		$D_{RCM,Struct.restr.}$/ $D_{RCM,Mat.restr.}$	D_{mc} [--]		$D_{RCM,load}$ (eq. 6.7) [$*D_{RCM,0}$]		$D_{RCM,Struct.restr.}$/ $D_{RCM,Mat.restr.}$
	Struc. restr.	Mat. restr.	Struc. restr.	Mat. restr.		Struc. restr.	Mat. restr.	Struc. restr.	Mat. restr.	
NWC	0.39	0.34	1.98	1.81	1.09	0.19	0.08	1.39	1.15	1.21
LWAC	0.37	0.30	1.91	1.69	1.13	0.16	0.07	1.32	1.13	1.17

to 19% and for lightweight aggregate concrete from 7% to 16% for material restraint and structural restraint, respectively. These values are presented in Table 6.4.

For the D_{mc}-values presented in Table 6.4 the increase of the apparent diffusion coefficient $D_{RCM,0}$ due to microcracking can be calculated with eq. (6.7). At 6 mm depth microcracking causes an increase of the apparent diffusion coefficient of NWC by a factor 1.98 and 1.81 for structural restraint and material restraint, respectively. For LWAC these factors were 1.91 and 1.69. At 24 mm depth these values were 1.39 and 1.15 for NWC and 1.32 and 1.13 for LWAC. These factors show that the enhancement factors in case of structural restraint are slightly higher than for material restraint. At 6 mm depth the difference is 9% for NWC and 13% for LWAC (Table 6.4, column 6), whereas at 24 mm depth the difference is 21% for NWC and 17% for LWAC.

6.5.2 Calculated effect of microcracking on chloride profiles

With the measured chloride profiles for NWC and LWAC, shown in figure 6.7, the apparent diffusion coefficients D_a and the chloride contents at the concrete surface C_s are determined by curve fitting, using eq. (6.1). The internal chloride content C_i in eq. (6.1) is taken as zero. Results of these curve fit analyses are shown in Table 6.5 and figure 6.14. In the fitting procedure the measured chloride contents at 3 mm depth were not considered, since those values were supposed to be too much affected by the dry-wet cycles and not representative for the diffusion process as presumed with Fick's second law, i.e. eq. (6.1). In the last column of Table 6.5 the ratios between the apparent diffusion coefficients for structural and materials restraint are presented. It is noted that for a good fit of the measured chloride profiles both the surface chloride content C_s and the apparent diffusion coefficient D_a are involved. Moreover, the measured chloride profiles are not only the result of diffusion, as presumed when using Fick's second law, but also by convection. It is well known, therefore, that care should be exercised with the interpretation of the results of curve fit analysis.

During the 1 month test period 15 exposure cycles were imposed (see figure 6.6). Each cycle had a wet period of 6 hours during which the concrete surface was in contact with chloride-containing water. In the simulation it is assumed that the total period during which the top of the beam was exposed to chloride-containing water lasted $15 \times 6 = 90$ hours. In reality chloride penetration also continued in each drying period when the thermal cycles were imposed.

Table 6.5 Apparent diffusion coefficients D_a and surface chloride contents C_s determined by curve fitting from measured chloride profiles. Assumed exposure time: 90 hrs.

Concrete	Structural restraint		Material restraint		$D_{a,Struc.restr.}/D_{a,Mat.restr.}$
	D_a [m^2/h]	C_s [%]	D_a [m^2/h]	C_s [%]	
NWC	$2.1 \cdot 10^{-7}$	3.7	$1.2 \cdot 10^{-7}$	3.5	1.75
LWAC	$2.5 \cdot 10^{-7}$	5.3	$1.8 \cdot 10^{-7}$	2.9	1.39

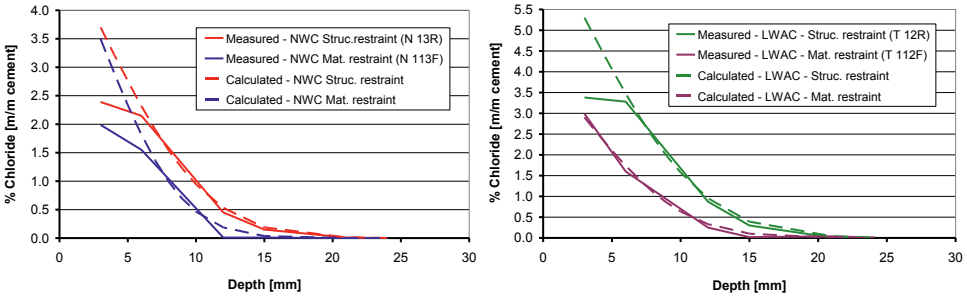

Figure 6.13 Measured and calculated chloride profiles in NWC (left) and in LWAC (right).

6.5.3 Evaluation of the effect of microcracking and type of restraint on chloride ingress

From both measurements and numerical simulations an increase of the apparent diffusion coefficient caused by microcracking can be inferred. In case of structural restraint the effect of microcracking is larger than in case of material restraint. The ratio of the apparent diffusion coefficients for structural and material restraint, determined from the damage ratios D_{mc} and presented in columns 6 and 11 from Table 6.4, are substantially smaller than the corresponding ratios determined by curve fitting form the measured chloride profiles, presented in column 6 of Table 6.54. Probably the most important reason for this difference is that the chloride profiles in the experiment were determined after 15 exposure cycles, whereas in the simulation not any effect of cyclic loading was considered. It is conceivable that due to cyclic loading the degree of microcracking has increased. This effect might have been more severe in case of structural restraint than in case of material restraint, since the stress level in case of structural restraint was higher than in case of material restraint.

6.6 Conclusions

In this chapter experimental data presented in literature on chloride ingress in the top layer of concrete beams was used for comparison with numerical simulations. The top layer of the beams was exposed to both thermal and hygral cycles, large enough the generate microcracking in the concrete. The experiment was designed such that both structural restraint and material restraint could be simulated.

From the imposed drying regime the shrinkage strains were determined to which the concrete of the top layer of the beam had been exposed. These strains were then used to calculate the damage ratio D_{mc} at different depths from the concrete surface. The apparent chloride diffusion coefficient was considered to increase with increasing damage ratio D_{mc} according the a correlation similar to the correlation between the apparent chloride diffusion coefficient and the UPV-damage degree D_{UPV} of concrete loaded in compression.

In the beam experiments microcracking was one of the parameters that affected the chloride ingress in the concrete. It is noted that the resulting chloride profiles were not only the result of microcracking, but also reflected the effect of different transport mechanisms, i.e. convection, diffusion and temperature. In the numerical simulations only the effect of microcracking on the transport properties was considered. This complicates a direct comparison of the simulations with the experimentally obtained results.

Unrestrained specimens (material restraint)

Drying shrinkage of the cement paste of the concrete of the pre-drilled cores was restrained by the aggregate particles and microcracking will have occurred (material restraint). Since the stiffness of dense aggregate is larger than that of lightweight aggregate, the degree of microcracking in NWC is expected to be more pronounced than in LWAC. Hence, the apparent diffusion coefficient of NWC was expected to be higher than that of the LWAC.

The calculated effect of microcracking on the apparent diffusion coefficients was indeed in line with these expectations. Results are given in Table 6.4. At a depth of 6 mm and 24 mm the calculated values of $D_{RCM,load}$ of NWC are higher than those of LWAC, although the difference is not very large.

The apparent diffusion coefficients derived from measured chloride profiles exhibit a different behaviour. Otherwise than expected, the apparent diffusion coefficients for NWC are lower than those of LWAC (See Table 6.5). A reason for this could be, that in real concrete the matrix-aggregate interfacial zone (ITZ) has a substantial effect on the chloride penetration in the concrete. It is plausible that in LWAC the ITZ is stronger and denser that in NWC, resulting in a lower rate of chloride penetration. In the calculations any effect of the ITZ on the chloride penetration is ignored. In the experiments, however, the contribution of the ITZ on the transport properties cannot be ignored.

Restrained specimens

The upper region of the test beams is fully restrained and is supposed to perform similar to the structural restraint conditions in the calculations. Beside microcracking induced by shrinkage additional damage will be caused by the temperature-induced strains (Fig. 6.11b). The effect of microcracking on the transport properties is, therefore, assumed to be more pronounced than in the case of material restraint.

As for the case of material restraint, also for the case of structural restraint the calculated apparent diffusion coefficient of NWC is slightly higher than that of LWAC (Table 6.4). The type of restraint, i.e. either structural or material restraint, appears of have a substantial effect. At 6 mm and 24 mm depth the apparent diffusion coefficient in case of structural restraint is larger than in case of material restraint. This is in line with the expectations.

Also the apparent chloride diffusion coefficients, determined by curve fitting of the measured chloride profiles, show that the effect of structural restraint on the apparent diffusion coefficient is larger than that of material restraint (Table 6.5). In the experiments, however, the effect of the degree of restraint appeared to be larger than in the numerical simulations (Table 6.4). One of the reasons for this could be the effect of cyclic loading in the experiment, which effect is not considered in the numerical simulations.

Overall conclusion

From the comparison of numerical simulations with experimental data it can be concluded that the effect of the type of restraint and restraint-induced microcracking on the apparent diffusion coefficient can be simulated to some extent. More than finding a trend with the simulations could hardly be expected. A detailed simulation of transport processes in cracked concrete would require a different and more sophisticated approach. In this chapter the focus was on the effect of the type of restraint on the degree of microcracking and the influence of microcracking on the transport properties.

As regards the degree of microcracking on the transport properties it has to be remarked, that in the simulations microcracking was considered as a *global* transport-enhancing effect. In reality an increasing intensity of microcracking may result in *clustering* of cracks, i.e. formation of wider penetrating cracks. Clustering or agglomeration of (micro)cracks has also been observed in the simulations presented in chapter 5. Clustered cracks may be more effective for transport than isolated cracks. This may also explain why the simulated effect of microcracking on the apparent diffusion coefficient was less pronounced than the effect observed in the experiments.

Chapter 7

7. Conclusions and recommendations

7.1 Evaluation

Whether concrete structures can fulfil their functional requirements during their service life depends, among others, on the ability of the concrete to withstand physical, chemical and mechanical 'loads'.

An important aspect in this respect is the intensity of microcracking in the concrete. In the design process and calculations an engineering approach is followed. This inplies that structural concrete is often assumed to be a initially homogenous defect and stress free material. In reality concrete is a non-linear viscous elastic solid where stress, and thus also cracks, are not only initiated by imposed (external) loads, but also by imposed (internal) deformations of the cement paste. Cement paste deformations due to shrinkage are (partially) restrained by aggregates. This is denoted as material restraint. Structural restraint due to a non-uniform strain field in a structural element is also investigated. This restraint might result in eigenstresses and microcracking.

The questions adressed in this research with respect to eigenstress en microcracking in concrete are:

- What is the influence of the cement paste properties (stiffness, bond/matrix tensile strength) and aggregate characteristics (size, aggregate volume fraction (AVF)), particle size distribution (PSD), stiffness) on the residual eigenstresses and microcracking?
- What is the influence of stress relaxation on the magnitude of the residual eigenstresses and microcracking?
- What is the influence of the microcracking, induced by eigenstresses, on transport properties, like chloride ingress, of concrete?

These questions lead to the following research question:

What is the effect of stress relaxation on residual eigenstresses and microcracking?

In this study concrete is modelled with a two-dimensional beam lattice model (BLM) with three element types: aggregate beams, cement paste matrix beams and bond beams between the matrix and the aggregates, representing the interfacial transition zone (ITZ).

The 'load' on the matrix- and bond beams is an imposed shrinkage strain deformation that is applied in increments. The method used for the stress calculation in each beam element is described in chapter 3.

Stress relaxation as a result of cement paste creep is calculated using the activation energy approach.

7.2 Conclusions

The results of the numerical analyses are described in chapter 5. The following conclusions were drawn:

- Stress relaxation can not prevent microcracking due to eigenstress to occur.
- Stress relaxation does not influence the magnitude of the maximum tensile eigenstress that occurs, but promotes the redistribution of eigenstresses. This results in a substantial reduction of the number of microcracks in the concrete.
- With a decreasing *cement paste stiffness* ($E_p = E_m = E_b$) the initiation of microcracking is postponed to a stage with higher shrinkage. The maximum structural eigenstress and the magnitude of microcracking, expressed with the microcrack damage ratio (D_{mc}), decrease, see section 5.5.1.
- With a decreasing *bond / matrix tensile strength ratio* (f_b/f_m) the maximum and residual structural eigenstress decreases while the magnitude of the microcracking (D_{mc}) increase, see section 5.5.2.
- The *aggregate stiffness* (E_a) influences the stiffness of the concrete in the non-cracked stage but has no significant influence on the maximum eigenstress the residual eigenstress and the magnitude of microcracking (D_{mc}), see section 5.5.3.
- Given a specific aggregate 'volume' fraction (AVF), the *aggregate particle size (d) and particle size distribution (PSD)* have no significant influence on the magnitude of the eigenstresses and microcracking when stress relaxation is taken into account. A small *aggregate particle size (d)* results in a fine mesh of microcracks in the specimen, see section 5.5.4.
- With a increasing *stress relaxation* the maximum structural eigenstress is reached at a greater shrinkage and the magnitude of microcracking (D_{mc}) decreases, see section 5.5.5.
- The *shape of the shrinkage curve* does not have influence on the evolution of the eigenstress and magnitude of microcracking in the case without stress relaxation. The maximum value of the shrinkage strain then controlls the eigenstress and microcracking, see section 5.8.2.
- The *shape of the shrinkage curve* controlls the magnitude of stress relaxation such that at a slower increasing shrinkage strain in the pre-peak stage the magnitude of stress relaxation increases which results in an increasing maximum structural eigenstress due to delayed microcrack initiation, see section 5.8.3.
- Microcracking substantially reduces the magnitude of concrete shrinkage (about 30% shrinkage reduction in concrete with an AVF of 0.75 m^2/m^2), see section 5.9.5, table 5.11.

- Stress relaxation reduces the magnitude of micro-cracking and thus has an increasing effect on the magnitude of concrete shrinkage (about 12% shrinkage reduction in concrete with an AVF of 0.75 m^2/m^2), see section 5.9.5, table 5.11.

The influence of shrinkage induced microcracking on the transport properties of concrete is dealt with in chapter 6. Conclusions in this respect are:

- Microcracking promotes the transport properties in concrete in such a way that with increasing microcracking the chloride content and penetration depth also increases.
- Microcracking due to shrinkage results in an increasing chloride ingress, expressed with the apparent diffusion coefficient $D_{RCM,load}$ (eq. 6.7) , while in practice the apparent diffusion coefficient D_a (eq. 6.2) reduces over time. An explanation for this phenomenon can be that self healing of the microcracks reduces the transport properties over time.
- Shrinkage is the major source for microcracking while environmental temperature chances have only limited inpact on the creation of microcracks.

7.3 Recommendations

1. The magnitude of microcracking is to a great extent controlled by relaxation of eigenstresses in the cement paste. The approach for calculating stress relaxation, used in this research, is based on the activation energy theory with parameters representing the energy state with respect to the mobility of cement paste material. Some values of these parameters are given in literature but the knowledge is limited and, when available, shows a wide scatter. Investigations with respect to the evolution and magnitude of the parameters (activation energy and activation volume) controlling the stress relaxation in cement paste can improve the reliability of microcrack prediction.
2. The magnitude of concrete shrinkage is not only controlled by the cement paste matrix shrinkage and aggregate restraint but is also influenced (reduced) by micro-cracking. Further research on its effect on concrete shrinkage is important for the analysis of the performance of concrete structures in practice.
3. An important parameter with respect to the evolution of eigenstresses and microcracking due to shrinkage is the evolution of the local restraints of the cement paste in the concrete. In this study a number of influencing parameters is analysed with a two- dimensional (2D) beam lattice model. Further research in this field with a tree- dimensional (3D) beam lattice model with the capability to take into account stress relaxation in a similar way as in this study is recommended.
4. Microcracking promotes the transport properties of concrete while measurements on structures in practice show a decreasing effect of the transport properties over time (expressed with the apparent diffusion coefficient D_a (eq. 6.2)). Further research on the processes which are responsible for this decreasing effect is important to improve the durability of concrete.

References

Alexander, M., Otieno, M., Beushausen, H. (2012), Cracking and durability of reinforced concrete structures. Proc. 2nd Int. Conf. on Microstructure-related Durability of Cementitious Composites. Amsterdam, pp. 88-97.

ASTM C597 (1997), Standard Test Method for Pulse Velocity through Concrete.

Bamforth, P.B. (2007), Early-age thermal crack control in concrete, CIRIA Publication 660, CIRIA, London, 112 p.

Bernard, F., Kamali-Bernard, S., (2010), Multi-scale modelling to predict ion diffusivity of cracked cement-based materials. Proc. 2nd Int. Symp. On Service Life Design for Infrastructure, Delft. Vol. 1, p. 157-166.

Bisschop, J.; Mier, J.G.M. (1999), Quantification of shrinkage microcracking in Young mortar with fluorescence light microscopy and ESEM, HERON, Vol. 44, No. 4, pp. 245-255.

Bisschop, J. (2002), Drying shrinkage microcracking in cement-based materials, Doctoral Thesis, Faculty of Civil Engineering, Delft University of Technology, 198 p.

Bouquet, G.Chr. Breugel, K. van (2007), Krimp van beton: een nadere beschouwing, CEMENT No. 7, pp. 73-78 (in Dutch language).

Bouquet, G.Chr., Braam, C.R. (2007), Scheurbeheersing in constuctief beton onder invloed van temperatuureffecten en krimp, CEMENT No. 8, pp. 63-67 (in Dutch language).

Bouquet, G.Chr., Braam, C.R. (2017), Numerical Anaysis of Long Term Effects on Eigenstresses and Micro-cracking in Concrete, Proceedings of the 2017 *fib* Symposium, Maastricht, The Netherlands, pp. 56-64.

Bungey, J.H., Millard, S.G. (1996), Testing of Concrete in Structures, Blackie Academic & Professional, London, 286 p.

Carlson, R.W. (1937), Drying shrinkage of Large Concrete Members, Journal of the American Concrete Institute, pp. 327-336.

Carlson, R.W; Houghton, D.L.; Polivka, M. (1979), Causes and Control of Cracking in Unreinforced Mass Concrete, ACI Structural Journal, Vol. 76, No. 7, pp. 821-838.

Counto, W.J. (1964), The effect of the elastic modulus of the aggregate on the elastic modulus, creep and creep recovery of concrete, Magazine of Concrete Research, Vol. 16, No. 48, pp. 129-138.

Covarrubias, J.P. (2007), Specification for concrete cracking. Concrete International, 29 (9), pp 50-54.

Crank, J. (1975), The mathematics of diffusion, Clarendon Press, Oxford, 414 p.

Daian, J.F., Saliba, J. (1993), Transient moisture transport in a cracked porous medium. In: Transport in Porous Media, Kluwer Academic Publishers, Vol 13. pp. 265-260.

Day, R.L., Gamble, B.R. (1983), The effect of changes in structure on the activation energy for the creep of concrete. Cement and Concrete Research, Vol. 13, No. 4, pp. 529-540.

Desmettre, C., Charron, J.-P., (2013), Water permeability of reinforced concrete subjected to cyclic tensile loading. ACI Materials Journal, Vol. 110, No. 1, pp. 79-88.

Eberhardt, M., (1993), Rissgefahr in jungem beton, MSc-thesis, Delft/Darmstadt.

Emborg, M. (1985), Thermal Stresses in Massive Concrete Structures – Viscoelastic Models and Laboratory Tests. Division of Structural Engineering, Lulea University of Technology, Licentiate Thesis 1985:011L, 2nd Edition 1988, 163 p.

Emborg, M. (1989), Thermal Stresses in Concrete Structures at Early Ages. Division of Structural Engineering, Lulea University of Technology, Doctoral Thesis 1989:73D, 285 p.

Emborg, M. et al. (1994), Models and methods for computation of thermal stresses and cracking risks. Springenschmid, R. (editors), International Symposium Thermal Cracking in Concrete at Early Ages, State-of-the-Art Report, RILEM TC 119-TCE.

Emborg, M. (1998), Models and Methods for Computation of Thermal Stresses. RILEM Report 15, Prevention of Thermal Cracking in Concrete at Early Ages, E & FN Spon, London, New York, pp. 178-230.

Emborg, M.; Bernander, S. (1994), Assessment of the Risk of Thermal Cracking in Hardening Concrete. Journal of Structural Engineering (ASCE), Vol. 120, No. 10, pp. 2893-2912.

EN 12390-4:2000, Testing of concrete – Part 4: Compressive strength – Specifications for testing machines, European Committee for Standardisation – CEN, Brussels, Belgium.

EN 1991-1-5:2003+C1:2011, Eurocode 1: Actions on structures – Part 1-5: General actions – Thermal actions, European Committee for Standardisation – CEN, Brussels, Belgium.

EN 1992-1-1+C2:2011, Eurocode 2: Design of concrete structures – Part 1-1, General rules and rules for buildings, European Committee for Standardisation – CEN, Brussels, Belgium.

EN 1992-2:2005+C1:2008, Eurocode 2: Design of concrete structures – Part 2, Concrete Bridges – Design and Detailing Rules, European Committee for Standardisation – CEN, Brussels, Belgium.

EN 1992-3:2006, Eurocode 2: Design of concrete structures – Part 3: Liquid retaining and containment structures, European Committee for Standardisation – CEN, Brussels, Belgium.

Eyring, H. (1935), The Activation Complex in Chemical Reactions, Journal of Chemical Physics, Vol. 3, No. 2, p. 107.

Fabien, A., Choinska, M., Bonnet, S., Pertue, A., Khelidj, A. (2012), "Experimental study of aggregate size effects on mechanical behaviour and permeability of concrete". Proc. 2nd Int. Conf. on Microstructure-related Durability of Cementitious Composites. Amsterdam, pp. 412-420.

Garboczi, E.J., Benz, D.P. (1998), Multiscale Analytical / Numerical Theory of the Diffusivity of Concrete, Advanced Cement Based Materials, No. 8, pp. 77-88.

Grassl, P., Wong, H.S., Buenfeld, N.R. (2010), Influence of aggregate size and volume fraction on shrinkage induced microcracking of concrete and mortar, Cement and Concrete Research, No. 40, pp. 85-93.

Grassl, P., Fahy, C., Gallipoli, D., Bolander, J.E. (2012), A lattice model for facture and mass transport in concrete. Proc. 2nd Int. Conf. on Microstructure-related Durability of Cementitious Composites. Amsterdam, pp. 969-977.

Gutsch, A., Rostàsy, F.S. (1994), Young concrete under high tensile stresses –Creep, Relaxation and Cracking. Proc. RILEM Symp. Thermal Cracking in Concrete at Early Ages", Munich, pp. 111-118.

Hansen, W. (1987-a), Drying Shrinkage Mechanisms in Portland Cement Paste, ACI Materials Journal, Vol. 70, No. 5, pp. 323-328.

Hansen, W. (1987-b), Constitutive Model for Predicting Ultimate Drying Shrinkage of Concrete, ACI Materials Journal, Vol. 70, No. 5, pp. 329-332.

Hansen, T.C.; Nielsen, K.E.C. (1965), Influence of aggregate properties on concrete shrinkage. ACI Materials Journal, Vol. 62, No. 7, pp. 783-794.

Hearn, H. (1999), Effect of Shrinkage and Load-Induced Cracking on Water Permeability of Concrete, ACI Materials Journal, March-April, pp. 234-240.

Hermann, H.J.; Hansen, A.; Roux, S. (1989), Fracture of disordered, elastic lattice in two dimensions, Physical Reviev B, Vol. 39, No. 1, pp. 637-648.

Hobbs, D.W. (1974), Influence of aggregate restraint on the shrinkage of concrete, ACI Materials Journal, No.71, pp. 445-450.

Hofstetter, G., Mang, H.A. (1995), Computational mechanics of reinforced concrete structures. Vieweg, Weisbaden.

Hsu, T.T.C., Slate, F.O. (1963-a), Tensile bond strength between aggregate and cement paste or mortar, ACI Journal Proceedings Vol. 60, No. 4, pp. 465-486.

Hsu, T.T.C., Slate, F.O., Sturman, G.M., Winter, G. (1963-b), Microcracking of plain concrete and the shape of the stress-strain curve, ACI Materials Journal, Vol. 60, pp. 209-224.

Idiart, A.E., Lopez, C.M., Carol, I. (2011), Modeling of drying shrinkage of concrete specimen at the meso-level. Materials & Structures, Vol. 44, pp. 415-435.

Jankovic, J.; Mier, J.G.M. (2001), Crack Development in Concrete due to Moisture Flow, HERON, Vol. 46, No. 3, pp. 169-179.

Jensen, A.D.; Chatterji, S. (1996), State of the Art Report on Microcracking and Lifetime of Concrete – Part 1, Materials and Structures, Vol. 29, No. 1, pp. 3-8.

Jun, T.-S., Korsunsky, A.M. (2010), Evaluation of residual stresses and strains using the Eigenstrain Reconstruction Method. Int. J. of Solid and Structures, 42, pp. 1678-1686.

Klug, P., Wittmann, F. (1969), Activation energy of creep of hardened cement paste, Materials and Structures, Vol. 2, No. 1, pp. 11-16.

Klug, P., Wittmann, F.H. (1974), Activation Energy and Activation Volume of Creep of Hardened Cement paste, Materials Science and Engineering, Vol. 15, pp. 63-66.

Koenders, E.A.B. (1997), Simulation of Volume Changes in Hardening Cement-Based Materials, Faculty of Civil Engineering, Delft University of Technology, Doctoral Thesis, 171 p.

Koenders, E.A.B., Breugel, K. van (1998), Modelling dimensional changes in low water/cement ratio pastes, Proceedings of the International Workshop organized by JCI, Edited by Ei-ichi Tazawa, Hiroshima, pp. 289-298.

Krausz, A.S., Eyring, H. (1975), Deformation kinetics, John Wiley & Sons, Inc. New York – London, 398 p.

Krausz, A.S., Krausz, K. (1996), The Constitutive Law of Deformation Kinetics, in Unified Constitutive Laws of Plastic Deformation, Edited by A.S. Krausz and K. Krausz, Academic Press, Inc., pp. 229-279.

Küter, A., Geiker, M.R., Olesen, J.F., Stang, H., Dauberschmidt, C., Raupach, M. (2005), Chloride ingress in concrete cracks under cyclic loading. Proc. of ConMat'05, Vancouver, BC, Canada, 10p.

Landis, E.N.; Shah, S.P. (1995), The influence of Microcracking on the Mechanical Behavior of Cement Based Materials, Advanced Cement Based Materials, No. 2, pp. 105-118.

Larson, M. (2000), Estimation of Crack Risk in Early Age Concrete – Simplified Methods for Practical Use. Department of Civil and Mining Engineering, Division of Structural Engineering, Licentiate Thesis 2000:10, 156 p.

Leonhardt, F. (1987), Cracks and crack control at concrete structures. IABSE Proceedings, Vol. 11, pp 25-44.

Li, F.; Li, Z. (2000), Acoustic Emission Monitoring of Fracture of Fiber-Reinforced Concrete in Tension, ACI Materials Journal, Vol. 97, No. 6, pp. 629-636.

Lilliu, G., Mier, J.G.M. van (2003), 3D lattice type fracture model in concrete, Engineering Fracture Mechanics, Vol. 70, No. 7-8, pp. 927-941.

Lilliu, G. (2007), 3D Analysis of Fracture Processes in Concrete, Doctoral Thesis, Delft University of Technology, Delft, The Netherlands, 151 p.

Lindquist W.D., Darwin, D., Browning, J., Miller, G.G. (2006), Effect of cracking on chloride content in concrete bridge decks. ACI Mat.erials Journal, Vol. 103, No. 6, pp. 467-473.

Locoge, P., Massat, M., Ollivier, J.P., Richet, C. (1992), Ion diffusion in microcracked concrete. Cement and Concrete Research, Vol. 22, No. 2-3, pp. 431-438.

Lopez, C., Carol, I., Murcia, J. (2001), Meso-structural modelling of basic creep at various stress levels In: Creep, shrinkage and durability mechanics of concrete and other quasi-brittle materials. Ed. F.-J. Ulm, Bazant, Z.P., Wittmann, F.H. Elsevier Science, pp. 101-106.

Lokhorst, S.J. (2001), Deformational behaviour of concrete influenced by hydration related changes of the microstructure. Report 25.5-99-05, TU Delft.

Lura, P. (2003), Autogeous Deformation and Internal Curing of Concrete, Doctoral thesis, Delft University of Technology, Delft, The Netherlands, 189 p.

Maage, M., Helland, S., Poulsen, E., Vennesland, O., Carlsen, J.E. (1996), Service life prediction of existing concrete structures exposed to marine environment, ACI Materials Journal, Vol. 93, No. 6, pp. 602-608.

Maso, J.C. editor (1996), Interfacial Transition Zone in Concrete, Ed. by J.C. Maso, State-of-Art Report prepared by RILEM Technical Committee 108-ICC, Interfaces in Cementitious Composites, RILEM Report 11, E & FN Spon, London, 179 p.

Marchand, J., Gerard, B., Delagrave, A. (1998), Ion transport mechanisms in cement-based materials and composites. In: Materials Science of Concrete, Ed. J.P. Skalny, American Ceramic Society, Vol. V, pp. 307-400.

Markeset, G., Skjølsvold, O., (2010), Time dependent chloride diffusion coefficient – Field studies of concrete exposed to marine environment in Norway. RILEM Proceedings pro070: 2nd International Symposium on Service Life Design for Infrastructure, pp. 83-90.

Melchers, R.E., Li, C.Q. (2006), Phenomenological modelling of corrosion loss of steel reinforcement in marine environments. ACI Materials Journal, Vol. 103, No. 1, pp 25-32.

Mohammed, T.U., Hamada, H., Yamaji, T. (2004), Concrete after 30 years of exposure: Mineralogy, microstructures, and interfaces. ACI Materials Journal, Vol. 101, No. 1; Part I: pp 3-12, Part II: 13-18.

Morrison, C.N.; Zhang, M.; Jivkov, A.P.; Yates, J.R. (2014), A Discrete Lattice Model of Quasi-brittle Fracture in Porous Graphite, Materials Performance and Characterization, Vol. 3, No. 3, pp. 414-428.

Moukarzel, C.; Hermann, H.J. (1992), A vectorizable random lattice, Journal of Statistical Physics, Vol. 68, No. 5-6, pp. 911-923.

Mu, S.; Schutter, G. de; Ma, B.G. (2013), Non-steady state chloride diffusion in concrete with different crack densities. Materials and Structures, Vol. 46, No. 1-2, pp. 123-133.

Mura, T. (1982), Micromechanics of Defects in Solids, Martinus Nijhoff Publishers, The Hague.

Nielsen, E.P.; Geiker, M.R. (2003), Chloride diffusion in partially saturated cementitious material, Cement and Concrete Research, Vol.33, No.1, pp.133-138.

Neville, A.M. (2010), Properties of Concrete, Fourth and Final Edition, Longman Group Ltd., England, 844 p.

Nilsson, L-O. (2012), Transport processes in the microstructure of concrete and their relevance for durability. Proc. 2nd Int. Conf. on Microstructure-related Durability of Cementitious Composites. Amsterdam, pp. 10-21.

Niu, J., Niu, D., Song, H., Liu, W. (2008), Durability of concrete structures under load. Proc. 1st Int. Conf. on Microstructure Related Durability., Nanjing, Vol. 1, pp. 517-524.

NT Build 492 (1999), Nordtest method, Concrete, Mortar and Cement-Based Repair Materials: Chloride Migration Coefficient from Non-Steady-State Migration Experiment, Nordtest, Espoo, Finland.

Orta, L., Bertlett, F.M., (2014), Stresses due to restrained shrinkage in concrete deck overlays. ACI Materials Journal, Vol. 111, No. 6, pp.701-710.

Padevět, P., Otcovská, T., Zobal, O. (2014), Variation of Material Properties of Cement Pastes with Various types of Fly Ash During Maturation, WSEAS Transportations on applied and theoretical mechanics, Vol. 9, pp. 88-96.

Pickett, G. (1956), Effect of Aggregate on Shrinkage of Concrete and Hypothesis Concerning Shrinkage, ACI Materials Journal, Vol. 52, No. 5, pp. 581-590.

Reissner, H. (1931), Eigenspanniung und Eigenspannungsquellen, Zeitschrift für Angewandte Mathematik und Mechanik, Vol. 11, No. 1, pp. 1-8.

Roelfstra, P.E. (1989), A Numerical Approach to Investigate the Properties of Concrete, Doctoral Thesis EPFL, Lausanne, 199 p.

Röhling, S. (2005), Zwangsspannungen infolge Hydratationswärme, Verlag Bau+Technik GmbH, Düsseldorf, Deutschland, 308 p.

Rostásy, F.S., Tanabe, T., Laube, M. (1998), Assessment of External Restraint, RILEM Report 15, Prevention of Thermal Cracking in Concrete at Early Ages. Edited by R. Springenschmid, E & FN Spon, London UK, pp. 149-177.

Sadouki, H., Wittmann, F.H. (1988), On the analysis of the failure process in composite materials by numerical simulation. Materials Science and Engineering, A / Vol. 104, pp. 9-20.

Sadouki, H., Wittmann, F.H. (2000), Shrinkage and iternal damage iduced by drying and endogenous drying, Proceedings of the International RILEM Workshop on Shrinkage of Concrete – Shrinkage 2000 (PRO 17), Paris, pp. 299-314.

Samaha, H.R., Hover, K.C. (1992), Influence of microcracking on the mass transport properties of concrete. ACI Materials Journal, Vol. 89, No. 4, pp. 416–424.

Sanahuja, J., Dormieux, L., Chanvillard, G. (2007), Modelling elasticity of a hydrating cement paste, Cement and Concrete Research, No. 37, pp. 1427-1439.

Schlangen, E. (1993), Experimental and numerical analysis of fracture processes in concrete, Doctoral Thesis, Delft University of Technology, Delft, The Netherlands, 121 p.

Schlangen, E. (2008), 3D modelling of fracture in concrete based on CT-scan observations. Proc. Int. RILEM symposium on Concrete Modelling – CONMOD'08. Delft, pp. 567-575.

Schlangen, E., Garboczi, E.J. (1997), Fracture simulation of concrete using lattice models: computational aspects. Engineering Fracture Mechanics, 57(2/3), pp. 319-332.

Schlangen, E., Koenders, E.A.B., Breugel, K. van (2004), Formation of eigenstress and cracks due to autogenous shrinkage, Proceedings FraMCoS-5, Vail, USA, paper 053, 8 p.

Schlangen, E., Mier, J.G.M. van (1992), Experimental and numerical analysis of micro-mechanics of fracture of cement-based composites. Cement and Concrete Composites, Vol. 14, No. 2, pp. 105-118.

Sluijs, L.J. (1992), Wave propagation localization and dispersion in softening solids. PhD Thesis, TU Delft.

Taheri-Motlagh, A. (1998), Durability of reinforced concrete structures in aggressive marine environment. PhD Thesis, Delft, 193 p.

Tasdemir, C., Tasdemir, M.A., Lydon, F.D., Barr, B.I.G. (1996), Effects of silica fume and aggregate size on the brittleness of concrete, Cement and Concrete Research, Vol. 26, No. 1, pp. 63-68.

Tawfiq, K., Armaghani, J., Vysyaraju, J.-R. (1996), Permeability of concrete subjected to cyclic loading. In: Transportation Research Record. Vol. 1532. No. 1, pp. 51-59.

Tegguer, A.D., Bonnet, S., Khelidj, A., Baroghel-Bouny, V. (2013), Effect of microcracking on gas permeability and chloride diffusion of concrete. 8th International Conference on Fracture Mechanics of Concrete and Concrete Structures – FraMCo-8, Toledo, Spain, pp. 1-12.

Timoshenko, S.P., Goodier, J.N. (1970), Theory of elasticity, Third Edition, McGraw-Hill Boor Company, New York, USA, 567 p.

Tognazzi, C. (1998), Couplage fissuration-dégradation chimique dans les matériaux cimentaires: caractérisation et modélisation. PhD Thesis, France, INSA Toulouse.

Töllner, M. (1995), Temperatur- und Spannungsentwicklung in hochfesten Bauteilen während der Hydratation. MSc-thesis, TH Darmstadt, TU Delft.

Traute, M., (1994), Reissneigung des hochfesten Betons im jungen Alter. Delft/Darmstadt, 161 p.

Ujike, I., Sato, R., Okazaki, S. (2010), Proposal of effective concrete cover in consideration of deterioration by internal cracking. Proc. 2nd Int. Symp. On Service Life Design for Infrastructure, Delft. Vol. 1, p. 41-48.

Unger, J.F., Eckhardt, S. (2011), Multiscale modelling of concrete. In: Archives of Computational methods in Engineering – State of the Art Reviews. Ed. Kleiber & Onate. Vol. 18, Nr. 3, pp. 341-393.

Van Breugel, K. (1980), Relaxation of young concrete, TU-Delft, Stevin report-5-80-D8.

Van Breugel, K. et al. (1996), Concrete structures under imposed thermal and shrinkage deformations – Theory and Practice (version 1996: in Dutch; version 2013: in English). Betonpraktijkreeks 2. Den Bosch. 214 p.

Van Breugel, K. (2000), Large-scale chloride penetration tests on beams exposed to thermal and hygral cycles, State-of-the-art report on LWAC – Material properties Report 1.2, EuroLightCon – Economic Design and Construction with Light Weight Aggregate Concrete, European Union – Brite EuRam III, Delft University of Technology, 41 p.

Vervuurt, A.H.J.M. (1997), Interface Fracture in Concrete, Faculty of Civil Engineering, Delft University of Technology, Doctoral Thesis, 164 p.

Vliet, M.R.A. van (2000), Size effect in tensile fracture of concrete and rock, Doctoral thesis, Delft University of Technology, Delft, The Netherlands, 192 p.

Wang, J., Basheer, P.A.M., Nanukuttan, S.V., Long, A.E., Bai, Y. (2016), Influence of service loading and the resulting microcracks on chloride resistance of concrete, Construction and Building Materials, Vol. 108, pp. 56-66.

Wang, K.J., Daniel, C.J., Surendra, P.S. (1997), Permeability study of cracked concrete. Cement & Concrete Research, 27, (3), pp. 381-393.

Wang, L.C. (2014), Experimental Study on Water Absorption by Concrete Damaged by Uniaxial Loading, 4th International Conference on the Durability of Concrete Structures, Purdue University, West Lafayette, USA, pp. 198-204.

Wang, L.C., Bao J.W. (2015), Influence of cracks and saturation on mass transport into concrete by mesoscale computational method. Proc. 3rd International Symposium on Concrete Modelling. Beijing, pp. 314-327.

Wang, Z.P., Wu, K.R., Ruan, S.G. (2001), Study of gas permeability of concrete under uniaxial compression. Journal of Building Materials, 4 (2), pp. 127-131.

Wittmann, F.H., et al. (1968), Surface tension, shrinkage and strength of hardened cement paste, Materials and Structures, RILEM, Vol.1, pp. 547-552.

Wittmann, F.H. (1974), Bestimmung physikalischer Eigenschaften des Zementsteins, Deutscher Ausschuss für Stahlbeton (DAfStb), Heft 232, Verlag Wilhelm Ernst & Sohn, Berlin, pp. 1-63.

Wittmann, F.H. (1977), Grundlagen eines Modells zur Beschreibung charakteristischer Ei genschaften des Betons, Deutscher Ausschuss fur Stahlbeton (DAfStb), Heft290, Verlag Wilhelm Ernst & Sohn, Berlin, pp. 43-101.

Wittmann, F.H. (1982), Creep and Shrinkage Mechanisms – Chapter 6 (pp. 129-161) in Creep and Shrinkage in Concrete Structures, Ed. Z.P. Bazant & F.H. Wittmann, John Wiley & Sons Ltd., 363 p.

Wittmann, F.H. (2008), On the development of models and their application in concrete science. Proc. Int. RILEM Symp. On Concrete Modelling CONMOD'08. Delft, pp. 1-11.

Wu, S., Wong H.S., Buefeld, N.R. (2015), Influence of drying-induced microcracking and related size effects on mass transport properties of concrete, Cement & Concrete Research, Vol. 68, pp. 35-48.

Yang, Y., Tong, H., Xu, S., Han, Y. (2008), Effect of load level on water permeability of concrete. Proc. 1st Int. Conf. on Microstructure Related Durability., Nanjing, Vol. 1, pp. 545-552.

Yang, Z.; Weiss, W.J.; Olek, J. (2005), Interaction between Microcracking, Cracking, and Reduced Durability of Concrete: Developing Methods for Considering Cumulative Damage in Life-Cycle Modeling, Final Report FHWA/IN/JTRP-2004/10, Purdue University, West Lafayette, IN 47907, 243 p.

Yu, Z. (2015), Microstructure development and transport properties of Portland Cement – Fly Ash binary systems. Doctoral Thesis, Delft University of Technology, Delft, 160 p.

Zhao, T.J. (2006), Concrete permeability. Science Press. Beijing, pp. 114-118.

Zheng, J.J., Li, C.Q., Zhou, X.Z. (2005), Thickness of interfacial transition zone and cement content profiles between aggregates, Magazine of Concrete Research, Vol. 57, No. 7, pp. 397-406.

CURRICULUM VITAE

Personal Details

Name:	Gustaaf Christiaan Bouquet
Date & place of birth:	April 28th 1949, 's-Gravenhage, The Netherlands
Nationality:	Dutch
E-mail:	guusbouquet@gmail.com

Education

1962 – 1967	High school, 's-Gravenhage, The Netherlands Diplomas: MULO-A & MULO-B
1967 – 1972	Hogere technische school voor bouw- en waterbouwkunde 's-Gravenhage Diploma: Bachelor of Science (BSc) – Ing.
1974 – 1981	Delft University of Technology, Department of Civil Engineering Delft, The Netherlands Diploma: Master of Science (MSc) – Ir.
1994 – 1995	Imperial College of Science, Technology & Medicine, Department of Civil Engineering, London, UK Diploma: Advanced Concrete Technology – MICT

Professional Experience

1972 – 1974	Military Service (72/5), Vaandrig pantserinfanterie, Breda, The Netherlands, Buren, Germany
1974 – 1989	Rijkswaterstaat – Directie Bruggen, Ministry of Transport and Public Works, Voorburg, The Netherlands Project leader of Concrete design group
1989 – 2007	Association of The Netherlands Cement Industry (VNC), 's-Hertogenbosch, The Netherlands – Consultant The Netherlands Cement Industry (ENCI), Ijmuiden, The Netherlands – Head of Concrete Laboratory
2007 – 2011	Delft University of Technology, Department of Civil Engineering PhD student (0,2 FTE funded by ENCI – studiefonds)

Appendix 4-1

Creep deformation – activation energy method

Under the influence of a uniaxial stress on a solid the creep strain rate can be written with the constitutive law [Krausz, A.S.; Eyring, H. (1975)][Krausz, A.S.; Krausz, K. (1996)]:

$$\frac{d\varepsilon_{cr}}{dt} = A_f \exp\left(-\frac{\left(U_f - \sigma\Delta V_f\right)}{RT}\right) - A_r \exp\left(-\frac{\left(U_r + \sigma\Delta V_r\right)}{RT}\right) \qquad \text{(A4-1.1)}$$

where:

$d\varepsilon_{cr}/dt$ = creep strain rate [m/m.h]
A_f = rate constant in forward activation [m/m.h]
A_r = rate constant in reverse activation [m/m.h]
U_f = activation energy in forward activation [J/mol], $U_f = N_A\Delta G_f$
U_r = activation energy in reverse activation [J/mol], $U_r = N_A\Delta G_r$
N_A = Avogadro constant [1/mol], $N_A = 6.0221\cdot10^{23}$ 1/mol
ΔV_f = activation volume in forward activation [m^3/mol], $\Delta V_f = N_A v_f$
ΔV_r = activation volume in reverse activation [m^3/mol], $\Delta V_r = N_A v_r$
R = universal gas constant [J/mol.K], $R = N_A k_B = 8.3145$ J/mol.K
σ = uniaxial stress [N/m^2]

The change in the height of the energy barrier, due to the mechanical energy ($\sigma\Delta v$), is shown in figure A4-1.1.

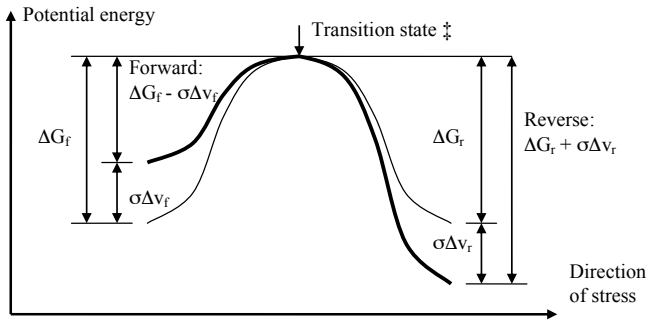

Figure A4-1.1 The energy reaction path when the mechanical energy $\sigma\Delta v$ is acting. The forward and reverse activation energies are indicated.

Under a low or moderate load compared to the material strength, and moderate temperature, it is usually assumed that the material characteristics associated with the forward and reverse activation have more or less the same magnitude, thus: $A_f \approx A_r$, $U_f \approx U_r$ and $\Delta V_f \approx \Delta V_r$. Under these boundary conditions the creep velocity can be written as:

$$\frac{d\varepsilon_{cr}}{dt} = 2A\exp\left(-\frac{U}{RT}\right)\sinh\left(\frac{\sigma\Delta V}{RT}\right) \qquad \text{(A4-1.2)}$$

Stress relaxation with the AE-method

In a moderate stress region, let say by stress/strength ratio's $\sigma/f < 0.5$, the energy barrier is symmetric, thus: $A_f \approx A_r$.

With eq.3.3 in section 3.2.2, the total strain rate can be written as:

$$\frac{d\varepsilon_{total}}{dt} = \frac{d\varepsilon_{el}}{dt} + \frac{d\varepsilon_{cr}}{dt} = \frac{1}{E}\frac{d\sigma}{dt} + 2A\exp\left(-\frac{U}{RT}\right)\sinh\left(\frac{\sigma\Delta V}{RT}\right) = 0 \qquad \text{(A4-1.3)}$$

$$\frac{d\sigma}{dt} = -2EA\exp\left(-\frac{U}{RT}\right)\sinh\left(\frac{\sigma\Delta V}{RT}\right) \qquad \text{(A4-1.4)}$$

with: $A = \frac{d\varepsilon}{dt}$

$$\int_{\sigma_0}^{\sigma}\frac{d\sigma}{\sinh\left(\frac{\sigma\Delta V}{RT}\right)} = -2EA\exp\left(-\frac{U}{RT}\right)\int_{t_0}^{t}dt \qquad \text{(A4-1.5)}$$

$$\int_{\sigma_0}^{\sigma}\frac{d\sigma}{\sinh\left(\frac{\sigma\Delta V}{RT}\right)} = \frac{\ln\left(\sinh\left(\frac{\sigma\Delta V}{2RT}\right)\right) - \ln\left(\cosh\left(\frac{\sigma\Delta V}{2RT}\right)\right)}{\frac{\Delta V}{RT}} = \frac{RT}{\Delta V}\ln\left(\tanh\left(\frac{\sigma\Delta V}{2RT}\right)\right)_{\sigma_0}^{\sigma} \qquad \text{(A4-1.6)}$$

$$\left(\frac{RT}{\Delta V}\right)\ln\left(\tanh\left(\frac{\sigma\Delta V}{2RT}\right)\right)_{\sigma_0}^{\sigma} = \left(\frac{RT}{\Delta V}\right)\ln\left(\tanh\left(\frac{\sigma\Delta V}{2RT}\right)\right) - \left(\frac{RT}{\Delta V}\right)\ln\left(\tanh\left(\frac{\sigma_0\Delta V}{2RT}\right)\right) \qquad \text{(A4-1.7)}$$

Substitution of eq. A4-1.7 in eq. A4-1.5 and $E(t_0) = E_0$ gives:

$$\left(\frac{RT}{\Delta V}\right)\ln\left(\tanh\left(\frac{\sigma\Delta V}{2RT}\right)\right) = \left(\frac{RT}{\Delta V}\right)\ln\left(\tanh\left(\frac{\sigma_0\Delta V}{2RT}\right)\right) - 2E_0A\left(t - t_0\right)\exp\left(-\frac{U}{RT}\right) \qquad \text{(A4-1.8)}$$

$$\ln\left(\tanh\left(\frac{\sigma\Delta V}{2RT}\right)\right) = \ln\left(\tanh\left(\frac{\sigma_0\Delta V}{2RT}\right)\right) - 2\left(\frac{\Delta V}{RT}\right)E_0A\left(t - t_0\right)\exp\left(-\frac{U}{RT}\right) \qquad \text{(A4-1.9)}$$

$$\ln\left(\frac{\tanh\left(\frac{\sigma\Delta V}{2RT}\right)}{\tanh\left(\frac{\sigma_0\Delta V}{2RT}\right)}\right) = -2\left(\frac{\Delta V}{RT}\right)E_0 A\left(t-t_0\right)\exp\left(-\frac{U}{RT}\right) \qquad \text{(A4-1.10)}$$

$$\tanh\left(\frac{\sigma\Delta V}{2RT}\right) = \tanh\left(\frac{\sigma_0\Delta V}{2RT}\right)\exp\left[-2\left(\frac{\Delta V}{RT}\right)E_0 A\left(t-t_0\right)\exp\left(-\frac{U}{RT}\right)\right] \qquad \text{(A4-1.11)}$$

$$\frac{\sigma\Delta V}{2RT} = \arctan h\left\{\tanh\left(\frac{\sigma_0\Delta V}{2RT}\right)\exp\left[-2\left(\frac{\Delta V}{RT}\right)E_0 A\left(t-t_0\right)\exp\left(-\frac{U}{RT}\right)\right]\right\} \qquad \text{(A4-1.12)}$$

$$\sigma(t,t_0) = \left(\frac{2RT}{\Delta V}\right)\arctan h\left\{\tanh\left(\frac{\sigma_0\Delta V}{2RT}\right)\exp\left[-2\left(\frac{\Delta V}{RT}\right)E_0 A\left(t-t_0\right)\exp\left(-\frac{U}{RT}\right)\right]\right\} \qquad \text{(A4-1.13)}$$

With the strain rate: $A = \frac{d\varepsilon_0}{dt}$ (A4-1.14)

The relaxation coefficient is defined as:

$$\psi(t,t_0) = \frac{\sigma(t,t_0)}{\sigma_0} \qquad \text{(A4-1.15)}$$

With the substitution of equation A4-1.13 and A4-1.14 in equation A4-1.15 the relaxation coefficient can be written as:

$$\psi(t,t_0) = \left(\frac{2RT}{\sigma_0\Delta V}\right)\arctan h\left\{\tanh\left(\frac{\sigma_0\Delta V}{2RT}\right)\exp\left[-2\left(\frac{\Delta V}{RT}\right)E_0\left(\frac{d\varepsilon_0}{dt}\right)\left(t-t_0\right)\exp\left(-\frac{U(t)}{RT}\right)\right]\right\} \qquad \text{(A4-1.16)}$$

where:
$\psi(t,t_0)$ = stress relaxation coefficient of cement paste [-]; $\psi(t,t_0) \leq 1.0$
σ_0 = stress at the time of loading t_0 [N/m^2]
$d\varepsilon_0/dt$ = imposed stress-dependent strain rate at the time of loading t_0 [m/mh]
E_0 = the modulus of elasticity of cement paste at the time of loading t_0 [N/m^2]
t = the actual age [h]
t_0 = the age at loading [h]
R = universal gas constant [J/molK], R = 8,3145 J/molK
T = absolute temperature [K]
ΔV = apparent activation volume of cement paste [m^3/mol]

The apparent activation energy of cement paste at time t (U = U(t)) is written as:

$$U(t) = U_0 + \Delta U_0 \ln\left(1 + \frac{(t - t_0)}{t_1}\right) \qquad \text{(A4-1.17)}$$

where:
$U(t)$ = apparent activation energy of cement paste at time t [J/mol]
U_0 = apparent activation energy of cement paste at the age of loading [J/mol]
ΔU_0 = potential increase of activation energy during the creep process [J/mol]
t_1 = 1 hour

Simplified expression of the relaxation coefficient equation A4-1.16

The tanh-function can be written with the approximation:

$$\tanh\left(\frac{\sigma\Delta V}{2RT}\right) \approx \frac{\sigma\Delta V}{2RT} \qquad \text{when } \sigma\Delta V < RT \qquad \text{(A4-1.18)}$$

With this assumption equation A4-1.11 can be written as:

$$\sigma = \sigma_0 \exp\left[-2\left(\frac{\Delta V}{RT}\right) E_0 A (t - t_0) \exp\left(-\frac{U}{RT}\right)\right] \qquad \text{(A4-1.19)}$$

For small stresses ($\sigma\Delta V < RT$) the energy function in equation A4-1.18 can be written with the approximation:

$$\exp\left(-\frac{U}{RT}\right) \approx \exp\left(\frac{\sigma_0\Delta V - U}{RT}\right) \qquad \text{(A4-1.20)}$$

By substitution of equation A4-1.19 in equation A4-1.18 the relaxation coefficient can be written as:

$$\psi(t, t_0) = \exp\left(-2\left(\frac{\Delta V}{RT}\right) E_0 \left(\frac{d\varepsilon_0}{dt}\right)(t - t_0) \exp\left(\frac{\sigma_0\Delta V - U(t)}{RT}\right)\right) \qquad \text{(A4-1.21)}$$

Numerical analysis of the relaxation coefficient equations
The evolution of the relaxation coefficient are calculated with the 'basic equation' A4-1.16 and the 'simplified equation' A4-1.21 with the parameters:

σ_0 = 0.1 MPa ($0.1 \cdot 10^6$ N/m^2)
ΔV = $7.0 \cdot 10^{-3}$ m^3/mol
U_0 = 12000 J/mol
$U_{cr,0}$ = 300 J/mol
E_0 = 7.8 GPa ($7.8 \cdot 10^9$ N/m^2)

RT = 2437.4 J/mol

Free cement paste shrinkage strain rate ($d\varepsilon/dt$) after 28 days is in the order of $8.0 \cdot 10^{-7}$ m/mh and after 91 days in the order of $8.0 \cdot 10^{-8}$ m/mh

In figure A4-1.2 the evolution of the 'original' equation A4-1.16 and the simplified presentation with equation A4-1.21 are plotted.

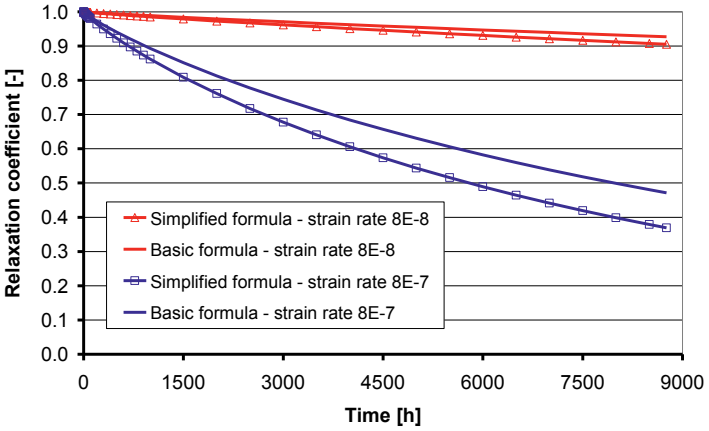

Figure A4-1.2 Evolution of the relaxation coefficient with stiffness $E_0 = 7.8 \cdot 10^9$ N/m^2; $\sigma_0 = 0.1 \cdot 10^6$ N/m^2; $\Delta V = 7.0 \cdot 10^{-3}$ m^3/mol. Strain rates: $8.0 \cdot 10^{-8}$ m/mh and $8.0 \cdot 10^{-7}$ m/mh. Stress relaxation with $U_0 = 12$ kJ/mol and $U_{cr,0} = 300$ J/mol.

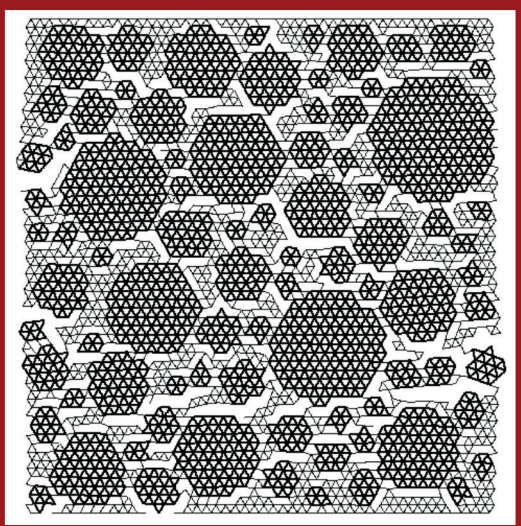

ISBN 978-94-6384-022-4